CHALMERS UNIVERSITY OF TECHNOLOGY
Gothenburg, Sweden
www.chamers.se

PHD THESIS

Newton's third law of motion states 'Every action has an equal and opposite reaction'. But does this law hold true for an interaction between a photon and a macroscopic object? Why does the tail of a comet always point away from the sun? How does a solar sail propel itself? The answers to these questions can be found in the field of optomechanics.

The field of optomechanics studies the mutual interaction between light and mechanical motion. The interaction between light and mechanics is enhanced placing the mechanical element inside an optical cavity. Cavity optomechanical devices can measure small displacements and forces with high sensitivity. They are used to measure gravitational waves in LIGO, to cool mechanical systems to their ground state using light and to create hybrid quantum systems that are useful for quantum technology.

This thesis covers experiments showcasing free-space monolithic integrated cavity optomechanical devices in III-V heterostructures. A key advantages of III-V heterostructures is the ability to grow tensile strained layers with precise thickness in a bottom-up grow and conducive for top-down fabrication. This enables the realization of sub-micrometer spaced mechanical resonators and an array of mechanical resonators of high mechanical quality in AlGaAs and InGaP heterostructures. The mechanical resonators can be patterned with a photonic crystal to increase their out-of-plane reflectance. We demonstrate modifications to the canonical optical spring effect due to the presence of the frequency-dependent photonic crystal.

The enhancement of the interaction strength between the light field and mechanical resonator remains a major challenge in optomechanics. In a system with the optomechanical coupling on the level of a single quanta larger than its losses, the interaction between light and mechanics becomes nonlinear. The nonlinear regime is key to explore novel quantum phenomena. The free-space multi-element optomechanical systems developed in this thesis are a promising approach towards the nonlinear regime.

SUSHANTH KINI MANJESHWAR • Free-space cavity optomechanical systems on a chip with III-V heterostructures • 2023

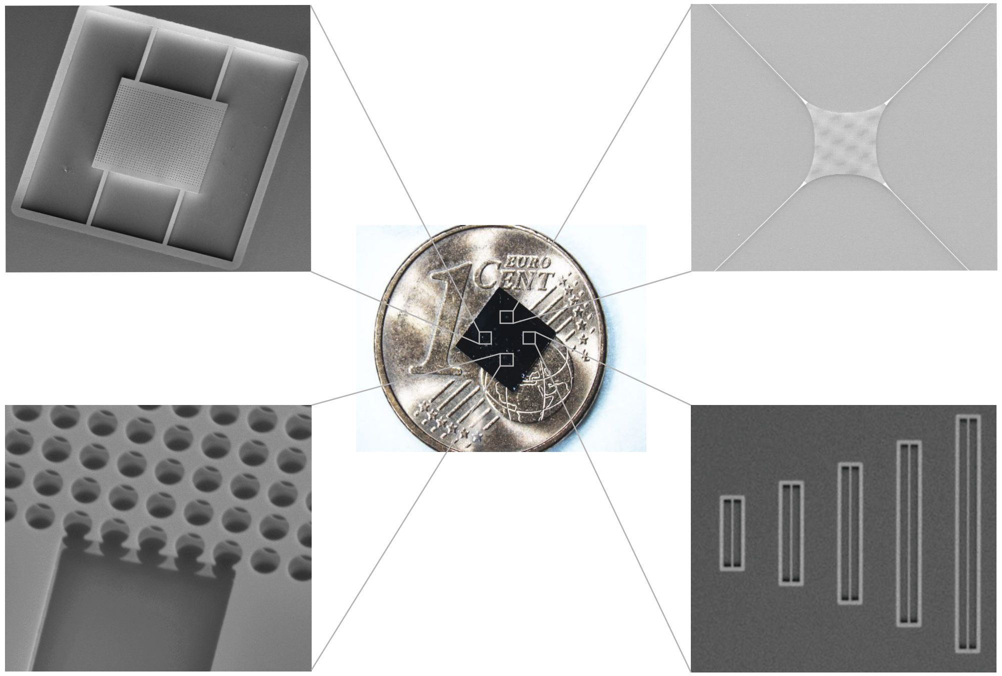

Free-space cavity optomechanical systems on a chip with III-V heterostructures

SUSHANTH KINI MANJESHWAR

DEPARTMENT OF MICROTECHNOLOGY AND NANOSCIENCE
CHALMERS UNIVERSITY OF TECHNOLOGY
Gothenburg, Sweden 2023
www.chalmers.se

THESIS FOR THE DEGREE OF DOCTOR OF PHILOSOPHY

Free-space cavity optomechanical systems on a chip with III-V heterostructures

Sushanth Kini Manjeshwar

CHALMERS
UNIVERSITY OF TECHNOLOGY

Department of Microtechnology and Nanoscience
Chalmers University of Technology
Gothenburg, Sweden, 2023

Free-space cavity optomechanical systems on a chip with III-V heterostructures

Sushanth Kini Manjeshwar
ISBN 978-91-7905-792-3

Technical Report No. 5258
ISSN 0346-718X
Department of Microtechnology and Nanoscience

Under the supervision of:
Witlef Wieczorek, Docent (1)
Åsa Haglund, Professor (2)

Examined by:
Per Delsing, Professor (1)

(1) Quantum Technology laboratory, Department of Microtechnology and Nanoscience
(2) Photonics laboratory, Department of Microtechnology and Nanoscience

Chalmers University of Technology
SE-412 96 Gothenburg, Sweden
Phone: +46 (0)31 772 1000
`www.chalmers.se`

Printed by Chalmers Reproservice
Gothenburg, Sweden, February 2023

Abstract

Cavity optomechanics examines the mutual interaction between light and mechanical motion for controlling mechanical resonators down to the quantum regime. A major challenge in the field of cavity optomechanics remains to access a strong interaction between the light field and mechanics on the level of single quanta. Optomechanical systems with small mode volumes show considerable enhancement in the interaction strength. However, in a majority of these systems, the increase in the interaction strength comes at the cost of additional optical losses. Therefore, one cannot exploit the novel capabilities of such systems often.

This thesis is about the development of a monolithic cavity optomechanical platform using III-V materials which demonstrates a pathway to combine a free-space optical cavity with an integrated mechanical system. To this end, we showcase the design, fabrication and characterization of optomechanical microresonators in AlGaAs/InGaP heterostructures. We demonstrate the enhancement of the out-of-plane reflectivity by reflectance engineering using photonic crystals. We utilize the features of III-V heterostructures by realizing monolithic fully-suspended micromechanical resonator arrays with sub-µm gaps in GaAs. This would make it possible to enhance the optomechanical interaction using the concept of multi-element optomechanics. We explore integrated cavity optomechanical systems formed by two photonic crystals reflectors and by a photonic crystal reflector with an integrated distributed Bragg mirror. Furthermore, we propose the use of highly-frequency dependent photonic crystal reflectors in the optomechanical system for realizing photonic bound states in a continuum, which decouple the otherwise coupled cavity loss rates and coupling strength.

The quality factor of the mechanical resonator can be increased by using tensile-strained InGaP, which is compatible with AlGaAs heterostructures growth. We determine the material properties of InGaP relevant to mechanical resonators. We demonstrate quality factors of 10^7 in trampoline resonators in InGaP at room temperature. The quality factor is pressure limited and can be enhanced using strain engineering. Free-space integrated multi-element cavity optomechanical systems in III-V heterostructures have the potential to enter the quantum optomechanical regime at room temperature.

Keywords: Optomechanics, III-V materials, Cavity Optomechanics, Photonic crystals, Micromechanical resonators.

List of Publications

This thesis is based on the following publications:

[A] **Sushanth Kini Manjeshwar**, Karim Elkhouly, Jamie M. Fitzgerald, Martin Ekman, Yanchao Zhang, Fan Zhang, Shu Min Wang, Philippe Tassin, and Witlef Wieczorek, "Suspended photonic crystal membranes in AlGaAs heterostructures for integrated multi-element optomechanics". Appl. Phys. Lett **116**, 264001 (2020).

[B] Jamie M. Fitzgerald, **Sushanth Kini Manjeshwar**, Witlef Wieczorek, Philippe Tassin, "Cavity Optomechanics with Photonic Bound States in the Continuum". Phys. Rev. Research **3**, 013131 (2021).

[C] **Sushanth Kini Manjeshwar**, Anastasiia Ciers, Fia Hellman, Jürgen Bläsing, André Strittmater, Witlef Wieczorek, "Micromechanical high-Q trampoline resonators from strained crystalline InGaP for integrated free-space optomechanics". arXiv:2211.12469 (2022).

[D] **Sushanth Kini Manjeshwar†**, Anastasiia Ciers†, Juliette Monsel†, Cindy Peralle, Shu Min Wang, Philippe Tassin, Witlef Wieczorek, "Cavity optomechanics with a chip-based microcavity using a suspended frequency-dependent photonic crystal mirror". Manuscript in preparation (2023).

[E] **Sushanth Kini Manjeshwar**, Anastasiia Glushkova, Jamie M. Fitzgerald, Shu Min Wang, Philippe Tassin, Witlef Wieczorek, "Double layer photonic crystal membranes in AlGaAs heterostructures for integrated cavity optomechanics". CLEO (2021).

[F] Anastasiia Glushkova, **Sushanth Kini Manjeshwar**, Jamie M. Fitzgerald, Shu Min Wang, Philippe Tassin, Witlef Wieczorek, "Integrated free-space optomechanics with AlGaAs heterostructures". CLEO Europe (2021).

[G] Jamie M. Fitzgerald, **Sushanth Kini Manjeshwar**, Witlef Wieczorek, Philippe Tassin, “Nanophotonic Structures for Cavity Optomechanics”. Proceedings of CLEO Europe (2021).

Other publications by the author, not included in this thesis, are:

[H] Juliette Monsel, Nastaran Dashti, **Sushanth Kini Manjeshwar**, Jakob Eriksson, Henric Ernbrink, Ebba Olsson, Emelie Torneus, Witlef Wieczorek, and Janine Splettstoesser, “Optomechanical cooling with coherent and squeezed light: the thermodynamic cost of opening the heat valve”. Phys. Rev. A. **103**, 063519 (2021).

Acknowledgments

The journey of the past five years is something I will always cherish. I would like to take this opportunity to thank everyone who has helped and supported me.

First and foremost, I am extremely grateful to my supervisor, Witlef Wieczorek for giving me this opportunity to join his group and pursue research under his guidance. Witlef, your optimism and enthusiasm has always been a source of inspiration. You have been a wonderful mentor to me in these past five years. You have always answered any questions I had with a smile. Thank you! Let's take a rain-check on that cleanroom visit!

I would like to thank my co-supervisor Åsa Haglund, and my examiner, Per Delsing for providing me with support and guidance through this journey despite your busy schedules. I would like to thank this opportunity to thank Ingo Breunig from my alma mater, University of Freiburg for showing me that research is fun and enjoyable and inspired me to take this big step towards a PhD.

I would like to thank Martí for helping me settle in Sweden and always taking time to solve my problems even when he had things to do. I will always be grateful to you. I would like to thank Matthias Rudolph for always being around for work and fun! We will see more of each other soon! I would also like to thanks Anastasiia for the patience and help in the past few years we have worked together on the optomechanics project. The optomechanics project is better for it! I would like to thank Karim, Johan and Fia for being great colleagues during your thesis! I want to express my gratitude to my group members Hanlin, Gerard, Achintya, Fabian and Hannes. I want to thank Juliette from AQP for helping in the theoretical work of the microcavity project. To all the colleagues - past and present - from QTL, thank you for making our group a wonderful and fun place to work.

I am grateful to Marcus Rommel, Niclas Lindvall, Mats Hagberg, Johan Andersson, Mahdad Sadeghi. Mattias Fredrikson and everyone else at NFL for training me on the tools, always being there to trouble shoot and solve issues. Being in the cleanroom is always fun because you make it seamless.

Most importantly, I would like to thank my parents and my wife Raksha for your unrelenting love and support. I would like to especially thank Raksha for her understanding in the last few months of my PhD. Finally, I would like thank my family and friends for their love and support.

Acronyms

MEMS:	Micro-electro-mechanical systems
PhC:	Photonic crystal
DBR:	Distributed Bragg reflector
BIC:	Bound state in the continuum
FEM:	Finite element method
TED:	Thermo-elastic damping
PML:	Perfectly matched layer
RCWA:	Rigorous Coupled-Wave Analysis
EBL:	Electron beam lithography
SEM:	Scanning electron microscope
TEM:	Transmission electron microscope
AFM:	Atomic force microscopy
EDX:	Energy-dispersive X-ray
XRD:	X-ray diffraction
NPS:	Noise power spectrum

Contents

CHAPTER 1

Introduction

Resonance is a fundamental property of matter. In nature, we find resonances in systems ranging from astronomical entities like pulsars all the way down to sub-atomic particles. The measurement and study of these resonances, which can be described as ‘sensing’, provides vital information about the system. Likewise, one can design and build a system to have the required behavior, which can be called ‘actuation’. This is how bridges, skyscrapers, loudspeakers, etc., are designed and constructed. The technology of sensing and actuation using resonators is not only found in large systems but also is ingrained in every aspect of modern technology. Decades of advancement in microfabrication methods have led to realization of highly efficient micro-electro-mechanical systems (MEMS) [1]. MEMS can be used to measure vibrations, displacement, pressure and forces. MEMS microresonators found, for instance, in satellites, phones, laptops, smart watches, cars. In research, these resonators are seen as a popular hardware platform for quantum experiments in the current era of the ‘second quantum revolution’.

In recent years, quantum control of mechanical resonators has seen tremendous progress [2], [3]. One such example is the cooling of micromechanical resonators to their quantum ground state of motion [2], [4], [5]. When sensing and actuation of the mechanical resonator is achieved using an optical cavity light field, we enter the realm of cavity optomechanics [3]. The field of cavity optomechanics encompasses systems with an extensive range of masses and frequencies. These include kilogram-scale mirrors with frequencies in Hz used in gravitational wave detection at LIGO [6] to attogram-scale nanobeams with frequencies in the GHz regime [4].

Historically, the mechanical quality factor of a resonator would reduce due to miniaturization [7]. However, recent advances in the fabrication of mechanical resonators in tensile-strained materials have led to the realization of high-quality micro- and nano-mechanical resonators. Such resonators are excellent platforms for quantum mechanical experiments as they have very low mass and high force sensitivity. The dissipation in micromechanical resonators is extremely low, therefore one can realize resonators with high mechanical Q-factors. Tensile strain enables implementation of methods such as strain engineering [8]–[15] and soft-clamping [9], [15]–[17] resulting in ‘dissipation dilution’. Amorphous SiN is the most widely used material in realizing tensile-strained mechanical resonators [8]–[10], [12], [13], [15], [16] showing mechanical Q-factors up to 10^9. Recent works have also shown mechanical resonators fabricated in crystalline materials such as GaAs [18]–[29], InGaP [30]–[33], SiC [11] and s-Si [14]. Amorphous materials have larger defect densities compared to crystalline materials [34]. Hence, we can assume that tensile-strained crystalline materials with strain engineering techniques would lead to higher mechanical Q-factors. The current record for mechanical quality factor in a micromechanical resonator, 10^{10}, was measured in crystalline silicon [14].

Mechanical resonators, when placed inside an optical cavity, interacts with the light field. This interaction mechanism is based on the principle of radiation pressure forces. Photons entering into the cavity impinge off the mechanical resonator and exert a force on it. This force results in a displacement of the resonator which leads to a change in the cavity length. The consequence of the cavity length change is the modification of the cavity field and its influence on the mechanical resonator [3]. The interaction strength is usually placed in comparison with the loss rates in the system, the optical and mechanical losses. The loss rate is usually dominated by the optical loss as the mechanical loss is several orders of magnitude lower in micromechanical systems [3].

The optomechanical system is said to be in the strong-coupling regime if the interaction strength is greater than the optical loss rate. In this regime, we observe hybridization between the optical and mechanical modes [3], [35]. If the interaction strength of a single photon in the cavity is greater than the optical loss rate, the system is classified to be in the single-photon strong coupling regime [36]. In the single-photon strong coupling regime non-linear quantum effects such as photon blockade [37] and direct generation of non-classical states [38] can be observed [3]. Single-photon strong coupling has so far been achieved only in systems with atomic gas [39] and Bose-Einstein condensates [40]. However, in microresonators the highest coupling achieved was two orders of magnitude short of being in the single-photon strong coupling regime [4], [5].

Another interesting regime is the ultra-strong coupling regime where the interaction strength is comparable to the frequency of the mechanical resonator [41], [42]. In this regime, effects such as mechanical mode splitting [43] and mechanical squeezing [44] can be observed.

The interaction strength is drastically enhanced in optomechanical systems with a small mode volume and large optical and mechanical mode overlap. These systems are usually described as integrated or on-chip cavity optomechanical systems. Optomechanical crystals seen in [45], [49], see Fig. 1.1(a) and whispering gallery mode resonators [46], [50], [51], Fig. 1.1(b) are examples of integrated optomechanical devices where the cavity mode is mainly confined within the material that, at the same time serves as the mechanical resonator leading to an increased interaction. The interaction between the light field and mechanics is on the order of the wavelength of the light. These systems can be realized on a chip by microfabrication and benefit from the resulting mechanical stability. However, since the light is predominantly in the material, optical losses in the form of absorption and scattering are present. As a result, the ratio of interaction strength and losses has not been improved so far. Optical microcavities in free-space can be realized by using highly

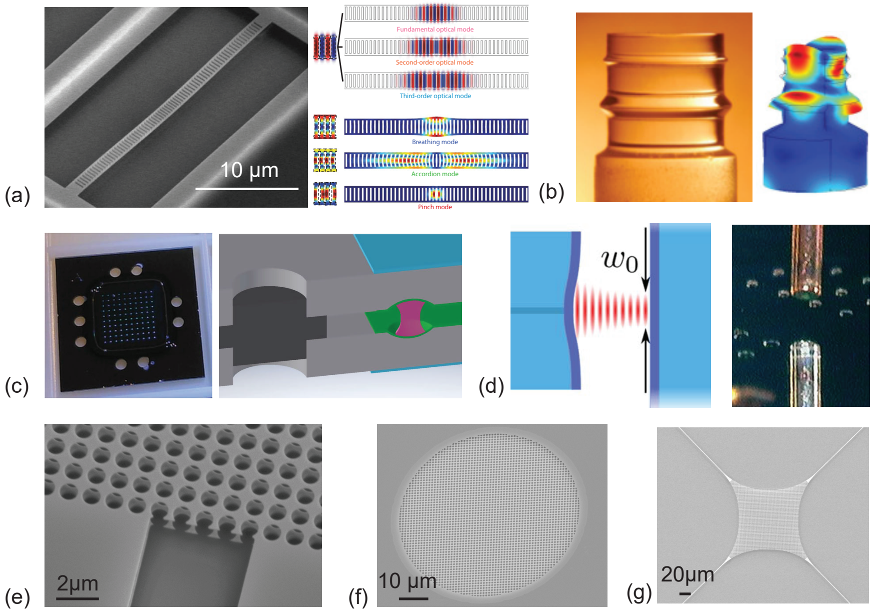

Figure 1.1: (a) Scanning electron microscope image of an optomechanical crystals along with the confined optical and mechanical modes. Image taken from Ref. [45] (b) A whispering gallery mode resonator shown alongside one of its mechanical mode. Image taken from Ref. [46]. (c) A chip with an array of micromirrors along with the schematic of a Fabry-Pérot microcavity formed with them. Image taken from Ref. [47]. (d) A fiber-based Fabry-Pérot microcavity. Image taken from Ref. [48]. Scanning electron microscope images of (e) a monolithic freely-suspended micromechanical resonators in GaAs patterned with photonic crystals (Sec. 4.1.1). (f) a suspended micromechanical resonator in GaAs with photonic crystal above a distributed Bragg reflector mirror (Sec. 4.1.3). (g) a trampoline shaped micromechanical resonator in InGaP (Sec. 4.2.2).

reflective mirrors [47], as seen in Fig. 1.1(c) or fiber-based Fabry-Pérot microcavities [48], [52], like in Fig. 1.1(d). A mechanical resonator, for example, a nanorod, can be introduced into this system to form a cavity optomechanical system [53]. However, such Fabry-Pérot type microcavities are realized by combining two or independent devices and may suffer from mechanical instability and optical losses during alignment.

An alternative method to increase the optomechanical coupling strength was proposed by Xuereb et al [54]. The optomechanical system consists of an array of identical, uncoupled mechanical resonators placed in an optical cavity, as seen in Fig. 1.2(a). Hence, the system is also referred to as multi-element cavity optomechanical system. The distance between each resonator, d, is selected such that the resonator array is transmissive. This is needed to assure the light field can interact with all the mechanical resonators in the array. The cavity field couples to the collective modes of the resonator array. Examples of such collective modes are seen in Fig. 1.2(b). Since the light is mainly concentrated between the mechanical resonators, the interaction between the collective mode and the optical field is large. The optical losses are given by the external cavity and remain the same while the interaction strength is enhanced. The multi-element approach is gaining attention in the field of cavity optomechanics as a promising avenue to attain single-photon strong coupling with several works adopting the approach [55]–[58].

In this thesis, we describe the work done over five years developing a monolithic free-space integrated cavity optomechanical system in III-V heterostructures. The goal was to combine the advantages of monolithic fabrication and stability found in integrated optomechanical systems [45], [46], [49]–[51] with reduced optical losses in free-space Fabry-Pérot microcavities. This is achieved by the bottom-up growth and top-down fabrication ability of III-V materials. This allows monolithic realization of multiple mechanical resonators and mirrors in the form of a distributed Bragg reflector (DBR) in the heterostructure. In this approach, the optical microcavity is predominantly formed in free-space, hence circumventing the disadvantage of the optical mode being confined within the material as in optomechanical crystals or whispering gallery mode resonators.

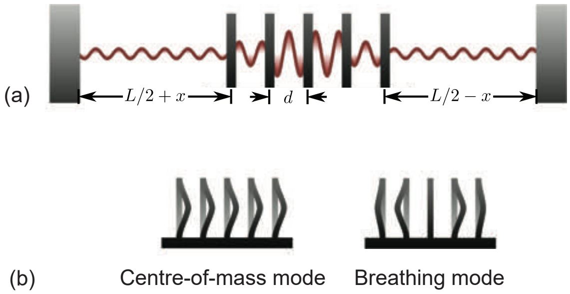

Figure 1.2: (a) Schematic of a multi-element optomechanical system. The system contains an array of uncoupled, identical mechanical resonators separated by a length d placed in an optical cavity of length L. (b) The collective modes of the mechanical resonators - The centre-of-mass and the breathing mode. Images taken from Ref. [54]

1.1 Contribution to the field

In this thesis, we show the viability of the approach to realize integrated free-space cavity optomechanical systems in AlGaAs heterostructures with high-reflectance, high-quality single-layer GaAs-based mechanical resonators. We design and fabricate the resonators and characterize their optical and mechanical properties. The out-of-plane high reflectance of the mechanical resonators can be achieved by reflectance engineering using photonic crystals [59]–[64]. The mechanical quality factor of 10^5 at room temperature is on-par with previously realized micromechanical resonators in GaAs [18]–[20], [22]–[29]. We demonstrate the validity of the method to use III-V heterostructures as the building block of an integrated free-space cavity optomechanical system. These results have been published in Paper A [21].

To showcase the advantage of III-V materials over other materials used in the field, we realize a monolithic micromechanical resonator array in AlGaAs-heterostructures seen in Fig. 1.1(e). We demonstrate the fabrication of two freely-suspended GaAs-based mechanical resonators patterned with photonic crystals. The mechanical resonators have a vacuum gap of $\approx 750\,\mathrm{nm}$ between them. We characterize the free-space microcavity formed between the two PhC patterned resonators. The mechanical characterization of the two mechanical resonators is performed. The mechanical frequency of the resonator exhibit modifications when the wavelength of the incident light is detuned around the microcavity resonance. We compare our system to other implementations of multi-element optomechanical system [55]–[58]. In Gärtner et al (Ref. [57]), the system is monolithic, however the two mechanical resonators are separated by the thickness of the substrate which is 200 µm. Additionally, the two resonators were fabricated in individual fabrication process. This implementation would result in uncontrollable gap between the resonators while also limiting the number of mechanical elements in the system to two resonators. In Nair et al (Ref. [55]), the monolithic system is realized by combining two SiN membranes with a spacer. The gap between the membranes varies from 8.5 µm to 200 µm. The manual combination of the SiN membranes can lead to additional optical losses due to relative tilt between the membranes while the gap between the membranes is limited by assembly and handling of the spacer. In Piergentili et al (Ref. [56]) and Wei et al (Ref. [58]), the SiN membranes are glued to piezos to provide control of the position of individual membranes. The relative tilt between the membranes and stability of the system are issues which affect these systems. The implementation discussed in this thesis circumvents the disadvantages of the above systems. Firstly, multiple mechanical resonators can be fabricated in the same fabrication process. Secondly, the gap between resonators can be controlled in the heterostructure growth. Finally, the issue of relative tilt between resonators is eliminated. To the best of my knowledge, there are no other works with monolithic resonator array with sub-µm gaps. These results were published in Paper E [65]and Paper F [66].

Photonic crystals (PhC) are highly frequency dependent reflectors. These PhC reflectors have internal guided resonances that couple to external radiations leading to a Fano lineshape [59], [60], [63], [64], [67]–[70]. In a double-layer system, the presence of two PhC guided resonances along with a microcavity mode leads to interference between these three, resulting in interesting optical behaviors. We can obtain an optical linewidth narrowing which decouples optical losses from the optomechanical coupling strength. The possibility of realizing an optical bound state in a continuum in a double-layer system is then discussed. We argue that the simple system of only two patterned freely suspended photonic crystal reflectors can potentially be used for quantum optomechanical experiments. These results are published in Paper B [71] and

Paper G [72].

Furthermore, we investigate the optomechanical effects in a system with one frequency-dependent reflector. To this end, we fabricate a PhC patterned mechanical resonator freely suspended over a distributed Bragg reflector mirror to form an integrated free-space optomechanical microcavity ,see Fig. 1.1(f). We show that the mechanical frequency shift due to the optical spring effect is drastically different compared to the canonical system where the mirrors are frequency-independent. We model the optomechanical system with Langevin equations including a frequency dependent reflector and attempt to understand the measured behavior. Although we cannot fully capture the measured shift, we show that we are able to capture the trend of the frequency shift. The optomechanical microcavity exhibits an optomechanical coupling strength comparable to the mechanical frequency ($g_0/\omega_m \approx 0.3$) which places the system in the ultra-strong coupling regime. The manuscript of this work is in preparation. A manuscript draft is appended as Paper D.

The GaAs-based devices cannot be used to realize mechanical resonators with $Q > 10^5$ as they are grown with minimal tensile stress. We change to another material system that can be grown on AlGaAs heterostructure with high tensile stress - InGaP [30]. We begin by experimentally determining the material properties relevant to mechanical resonators using one-dimensional string resonators [31], [32]. We observe a time dependent Q degradation in InGaP due to a currently undetermined reason. We fabricate trampoline-shaped micromechanical resonators, see Fig. 1.1(g) which show a $Q > 10^7$, the highest reported to date in an InGaP-based micromechanical resonator. We propose that, if the time-dependent Q degradation issue is solved, InGaP-based mechanical resonators can be used to realize integrated free-space multi-element optomechanical systems. Such a system has the potential to achieve the elusive single-photon strong coupling regime in optomechanics. The results of this work are published in Paper C [33].

1.2 Thesis structure

In Chapter 2, we introduce the key theoretical concepts that are relevant to the experiments performed in this thesis. We discuss mechanical resonators and their dissipation mechanisms, tensile-strained resonators, optical resonators and optomechanical effects in frequency-independent and -dependent optomechanical systems.

In Chapter 3, we discuss the methods used in designing, fabricating and measuring the optomechanical devices. We look at the simulation methods used to design/determine the optical and mechanical properties of the devices. The microfabrication process used in realizing the optomechanical devices is discussed extensively. The optical measurement setups used to characterize the optical, mechanical and optomechanical properties of the devices are presented.

In Chapter 4, we provide an overview of the results in GaAs- and InGaP-based optomechanical resonators. We sequentially discuss the results of optical, mechanical and optomechanical measurements undertaken on single layer PhC, PhC-PhC and PhC-DBR GaAs-based systems. Following which, the material properties of InGaP relevant to mechanical resonators are presented. Finally, the results of trampoline-shaped micromechanical resonator and their dissipation limits are discussed.

In Chapter 5, the summary of the results presented in the thesis is given and we give an outlook for the future of the project.

Chapter 6 contains an appendix with a description of the parameter estimation method used in the PhC-DBR system. Additionally, the frequency pull factor and single-photon optomechanical coupling rates of optomechanical microcavities in literature are shown for comparison to the system discussed in this thesis. Finally, the measured and simulated mechanical frequencies of InGaP trampoline resonators for different orientation is shown.

Finally, Chapter 7 consists of a brief summary of Papers A to G. The full papers are appended after the summary.

CHAPTER 2

Theory

This chapter introduces the theoretical concepts required to understand the experimental results presented in this thesis. An optomechanical system is presented in Fig. 2.1. It consists of a Fabry-Pérot cavity (optical resonator) interacting with an oscillating mirror (mechanical resonator). The radiation pressure of the intracavity light field displaces the mirror which changes the cavity length and the resonance frequency of the cavity and, thus the intensity of the optical cavity field.

We begin by describing the fundamental properties of micro- and nanomechanical resonators such as mechanical eigenmodes, effect of stress and strain on the resonator's eigenfrequencies and dissipation. We introduce the concept of dissipation dilution that is used to enhance the mechanical quality factor in tensile stressed materials. Next, an optical resonator and its fundamental properties - optical losses, finesse, etc., are discussed. We then

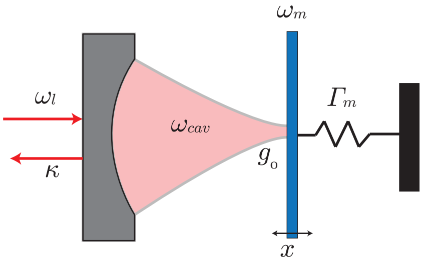

Figure 2.1: Schematic of an optomechanical cavity where the oscillating mirror modulates the cavity length. The standard form of an optical cavity formed with a fixed and a moveable mirror. The input laser frequency ω_l, the cavity frequency ω_{cav}, the mechanical frequency ω_m, the mechanical dissipation Γ_m, the optical loss κ, the optomechanical coupling g_0 and the displacement of the mechanical resonator x.

describe the optomechanical Hamiltonian, and the Langevin equations used to describe the optomechanical dynamics which lead to the optical spring effect, optomechanical damping, etc. The theory of Fano resonances and bound state in a continuum that occur in photonic crystal reflectors is described. Furthermore, the modification to the Langevin equations due to the presence of a frequency-dependent PhC reflector is introduced. The description of the theory is kept short and the reader is recommended for an in-depth discussion to review the cited references.

2.1 Mechanical resonators

Mechanical resonators contain oscillating vibrational modes. The spatial displacement of the geometry during the vibrations is given by the displacement field $\vec{u}(\vec{r})$. The amplitude of the oscillation $x(t)$ can be found by writing the displacement field as $\vec{u}(\vec{r}, t)$ where $\vec{u}(\vec{r}, t) = \vec{u}(\vec{r}) \cdot x(t)$. The mechanical resonator can have several modes each with its unique displacement field $\vec{u}_n(\vec{r}, t)$ where n is the mode number. The dynamics of these modes for sufficiently small amplitudes can be approximated by the equation of motion of a harmonic oscillator [3]:

$$\ddot{x}_n(t) + \Gamma_n \dot{x}_n(t) + \omega_n^2 x_n(t) = \frac{F_{\mathrm{ex}}(t)}{m_{n,\mathrm{eff}}}, \tag{2.1}$$

where ω_n and Γ_n are the angular frequency and damping associated with the n-th mechanical mode, $m_{n,\mathrm{eff}}$ is the effective mass of the mechanical mode and $F_{\mathrm{ex}}(t)$ is the sum of all the external forces acting on the mechanical resonator.

One of the mechanical resonators used in this thesis are string resonators. The mechanical response of string resonators can be fully described analytically by its material properties [73]. The eigenfrequency of highly tensile stressed string resonators used in this thesis (Sec. 4.2.1) is given by [31], [33], [73]

$$\omega_n = 2\pi \frac{n}{2L}\sqrt{\frac{\sigma}{\rho}}, \tag{2.2}$$

where n is the mode number, σ is the tensile stress in resonator, L is the length of the string resonator and ρ is the density of the material. In Fig. 2.2, we look at the finite element simulation (described in Sec. 3.1.1) of the fundamental mechanical modes in the different geometries used in this thesis. The mechanical quality factor of a single mechanical mode of the resonator Q which is parameter to judge the coherence time of a mechanical mode is given by $Q = \omega_m/\Gamma_m$. It is evident that high-Q mechanical resonators are achieved by increasing the mechanical frequency ω or reducing the dissipation in the system Γ. High-Q mechanical resonators are desirable as they have high coherence time and a lower thermal force noise, $S_{\mathrm{FF}} = 4k_{\mathrm{B}}Tm_{n,\mathrm{eff}}\Gamma_m$. The dissipation mechanisms in mechanical resonators and methods to mitigate them are discussed in Sec. 2.1.1.

Consider a single mechanical mode, Eq. 2.1 can be written in Fourier space using the Fourier transform, i.e., $x(\omega) = \int_{-\infty}^{\infty} x(t)e^{i\omega t}dt$, as $x(\omega) = \chi_m(\omega)F(\omega)$ where χ_m is the mechanical susceptibility. The susceptibility describes the response of the resonator to applied forces and is given by [3]

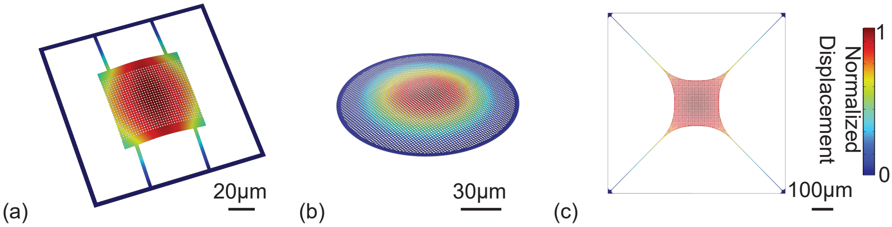

Figure 2.2: Finite element simulation showing the fundamental mode of the resonator geometries used in this thesis. (a) Free-free geometry patterned with PhC (b) Fully clamped membrane resonators patterned with PhC (c) Trampoline resonators patterned with PhC.

$$\chi_m(\omega) = \frac{1}{m}\left(\frac{1}{\omega_m^2 - \omega^2 - i\Gamma_m\omega}\right). \tag{2.3}$$

The mean square value of $x(t)$, i.e., $\langle x^2(t)\rangle$ is obtained by integrating over the noise power spectral density $S_{xx}(\omega)$ to obtain $\langle x^2(\omega)\rangle = \int_{-\infty}^{\infty} S_{xx}(\omega)d\omega$ where $S_{xx}(\omega)$ is given by [74]

$$S_{xx}(\omega) = \frac{F_{th}(\omega)}{m}\frac{1}{(\omega_m^2 - \omega^2)^2 + \Gamma_m^2\omega^2}. \tag{2.4}$$

For a high-Q mechanical system, in the frequencies where $\omega \approx \omega_m$, Eq. 2.4 can be approximated to a Lorentzian response given by [3], [74]:

$$S_{xx}(\omega) = \frac{\Gamma_m k_\mathrm{B} T_m}{2\pi m_\mathrm{eff}}\frac{1}{(\omega_m - \omega)^2 + (\Gamma_m/2)^2}. \tag{2.5}$$

The Lorentzian response of a thermally driven mechanical resonator is used to experimentally extract ω_m and Γ_m. The mechanical quality factor Q is calculated by performing a ringdown measurement [75].

2.1.1 Mechanical dissipation

Mechanical resonators lose mechanical energy through several dissipation mechanisms. The mechanical quality factor Q is defined as the ratio of the energy stored, W and the energy lost in the resonator, ΔW during one oscillation [73]:

$$Q = 2\pi \frac{W}{\Delta W}. \tag{2.6}$$

The dissipation mechanisms in the resonator can be divided into intrinsic and extrinsic dissipation. The total dissipation of a resonator is the sum of all the different dissipation mechanisms and Q is limited by the largest source of dissipation and is given by [76]

$$Q^{-1} = Q^{-1}_{\text{intrinsic}} + Q^{-1}_{\text{extrinsic}}. \tag{2.7}$$

Intrinsic dissipation originates from the oscillation of the mechanical resonator. The oscillation leads to a dynamic strain which couples to the internal degrees of freedom of the material. Due to the aforementioned coupling, the strain and the resulting stress will acquire an out-of-phase component. The delay is the relaxation time of the internal degrees of freedom to the new equilibrium [76], [77]. Intrinsic losses can occur due to material surface defects, volume defects, thermal expansion of the material leading to thermoelastic damping (TED) among others[76], [78]. The extrinsic dissipation originates from the interaction of the resonator with its environment. It includes damping due to gas molecules around the resonator and the energy loss into the support of the resonator via acoustic phonons. The total quality factor then can be written as

$$Q^{-1} = Q^{-1}_{\text{Surface}} + Q^{-1}_{\text{Volume}} + Q^{-1}_{\text{TED}} + Q^{-1}_{\text{Gas}} + Q^{-1}_{\text{Clamping}} + Q^{-1}_{\text{Misc}}, \tag{2.8}$$

where Q^{-1}_{Misc} constitutes the remaining damping mechanisms. In the following, we will describe dissipation mechanisms relevant in micro- and nanomechanical resonators that we employ in this thesis.

Thermoelastic damping

During the oscillation of a mechanical resonator, the bending creates a temperature gradient which depends on the thermal expansion coefficient, α within the material. The region that is compressed and expanded experiences a temperature increase (decrease) and decrease (increase) respectively for a positive (negative) value of α. This temperature gradient leads to an irreversible flow of phonons from the hot to the cold region of the material. This flow of phonons leads to energy being lost, which is referred to as thermoelastic damping. The quality factor limited by TED, Q_{TED}^{-1} is given by [76]

$$Q_{\mathrm{TED}}^{-1} = \frac{\alpha^2 T E}{\rho C_{\mathrm{p}}} \frac{\omega_m \tau_{\mathrm{TED}}}{1 + (\omega_m \tau_{\mathrm{TED}})^2}, \tag{2.9}$$

where T is the temperature, E is the Young's modulus, ρ is the density, C_{p} is the specific heat at constant pressure, ω_m is the mechanical frequency and τ_{TED} is the thermal relaxation time. τ_{TED} is given by

$$\tau_{\mathrm{TED}} = \frac{h^2 \rho C_{\mathrm{p}}}{\pi^2 \kappa}, \tag{2.10}$$

where h is the thickness of the resonator and κ is the thermal conductivity. The dissipation via TED can be minimized by operating at a temperature where $\alpha \to 0$.

Gas Damping

Gas damping is the most prominent loss in micromechanical resonators operated in ambient conditions. The gas molecules in the environment that collide with the resonator acquire momentum that leads to mechanical energy being lost. Gas damping can be differentiated into two regimes, fluidic and ballistic. In the fluidic regime which is present at high pressures, the gas is modeled as a viscous medium. In this case, the dimensions of the resonator are larger than the mean free path of the gas molecules. At high pressures, gas damping is the limiting dissipation mechanism. At lower pressures, the gas damping transitions into the ballistic regime. As the pressure decreases, the number of gas molecules in the environment reduces. Then, the mean free path of the gas molecules will become larger than the dimensions of the resonator. The gas damping limited quality factor in the ballistic regime Q_{Gas}^{-1} is given by [76]

$$Q_{\mathrm{Gas}}^{-1} = \frac{4}{\rho h \omega_m}\sqrt{\frac{2M_{\mathrm{m}}}{\pi RT}}P, \tag{2.11}$$

where M_{m} is the molar mass of the gas, R is the universal molar gas constant and P is the pressure. The gas damping can be mitigated by operating in low pressures, typically smaller than 10^{-8} mbar.

Clamping loss

The oscillations of the resonator result in elongation and bending of the mechanical resonator geometry. These deformations result in shear forces at the clamping points leading to elastic strain and stress. This elastic energy consequently produces acoustic waves that propagate to the substrate through the clamping point. This acoustic wave propagation leads to energy dissipation from the mechanical resonator to its support, hence it is also called radiation loss. The efficiency of the wave propagation depends on the acoustic impedance matching between the resonator and the support [73]. Hence, clamping loss is highly dependent on the geometry of the resonator. A two-dimensional square membrane is the limiting case for the geometry-dependent clamping loss as the resonator is connected to the support at its perimeter. For a square membrane, connected to a semi-infinite substrate, the clamping loss limited quality factor, Q_{Clamp} is given by [73]

$$Q_{\mathrm{Clamp}} = 1.5\left(\frac{E_s}{\sigma}\right)^{\frac{3}{2}}\sqrt{\frac{\rho_s}{\rho_r}}\frac{n^2m^2}{(n^2+m^2)^{\frac{3}{2}}},\frac{L}{h}, \tag{2.12}$$

where E_s is the Young's modulus of the substrate, σ is the stress in the resonator, ρ_s (ρ_r) is the density of the substrate (resonator), n and m are the mode number, L and h is the length and thickness of the resonator. Clamping losses can be reduced by careful engineering of the clamping points. Clamping losses are estimated in this thesis numerically using a perfectly matched layer in finite element simulations, see Sec. 3.1.1 [11], [79].

Intrinsic quality factor

The extrinsic damping can be reduced by operating at ultrahigh vacuum and modifying the clamping points. In the case where the extrinsic damping mechanisms are not the limiting damping mechanisms, then the mechanical factor Q is purely dependent on intrinsic dissipation, and is given by Q_{int}, [73]

$$Q_{\mathrm{int}} = 2\pi \frac{W_{\mathrm{elongation}} + W_{\mathrm{bending}}}{\Delta W_{\mathrm{elongation}} + \Delta W_{\mathrm{bending}}}, \tag{2.13}$$

where $W_{\mathrm{elongation}}$ (W_{bending}) and $\Delta W_{\mathrm{elongation}}$ ($\Delta W_{\mathrm{bending}}$) are the potential energy stored and lost in the elongation (bending) of the resonator during one oscillation.

2.1.2 Tensile stress in mechanical resonators

The intrinsic quality factor of micromechanical resonators is typically below 10^4 [10], [11], [14], [15], [78], [80]. Recent advancements in fabricating tensile-strained micromechanical resonators have shown mechanical quality factors of $Q \approx 10^{10}$[14]. This is possible due to the presence of tensile stress in the material. Tensile stress enhances the mechanical quality factor due to additional tensile potential energy which increases the total energy of the system (Eq. 2.13) whilst the energy lost remains the same. The tensile-stress enhanced Q can be expressed as [73] :

$$Q = 2\pi \frac{W_{\mathrm{tensile}} + W_{\mathrm{elongation}} + W_{\mathrm{bending}}}{\Delta W_{\mathrm{elongation}} + \Delta W_{\mathrm{bending}}}, \tag{2.14}$$

where W_{tensile} is the stored elastic energy due to the tensile stress.

The growth of heterostructures in crystalline materials can result in tensile stress within the material [31], [33], [81]. Crystalline materials can be grown with high-quality, low-defect thin films using epitaxial growth techniques such

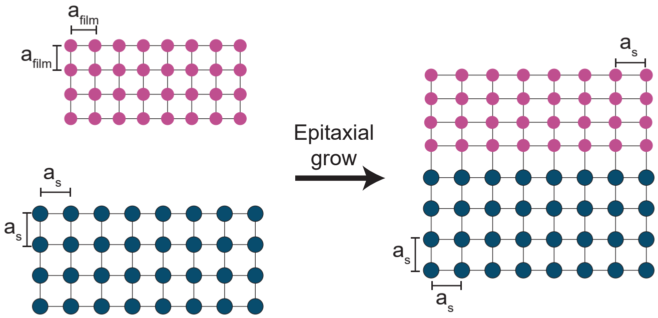

Figure 2.3: Tensile stress in epitaxially grown thin films. The substrate (blue) and thin film (purple) have different native lattice constants denoted by a_s and a_film, respectively. The film grown on top of the substrate adapts its lattice constant to that of the substrate leading to strain in the thin film.

as molecular beam epitaxy and metalorganic chemical vapour deposition. The epitaxial growth techniques allow a precise control over film thickness and enable growth of heterostructures [81]. A thin film of a crystalline material when grown epitaxially on a substrate, follows the crystal orientation and lattice constant of the substrate, as seen in Fig. 2.3 [31], [81]. If the native lattice constant of the material is different to the substrate it leads to an in-plane strain in the thin film, ϵ given by [31]

$$\epsilon = \frac{a_\mathrm{s} - a_\mathrm{film}}{a_\mathrm{film}}, \tag{2.15}$$

where a_s and a_film are the lattice constants of the substrate and film respectively. The grown film remains crystalline after growth only if the two lattice constants are close, else the film will have severe defects. A certain thickness of the film, referred to as the critical thickness, grows without defects following the crystal structure of the substrate [21], [31]. After the critical thickness, the thin film starts to relax towards its native lattice constant. The relaxation also leads to crystallographic defects [21], [31].

The tensile stress, σ that originates as a result of the strain is given by $\sigma = E\epsilon$, where E is Young's modulus of the thin film material. For an isotropic material, Young's modulus and the stress are isotropic. However for an anistropic material like III-V materials, Young's modulus ans stress also depends on the crystal direction. The elasticity in a material can be defined by the stress tensor σ_{ij} and strain tensor ϵ_{kl}. They are related to each other by a fourth order stiffness tensor C_{ijkl} as [82] :

$$\sigma_{ij} = C_{ijkl}\epsilon_{kl}. \tag{2.16}$$

For materials like GaAs and InGaP which have a zinc-blende crystal structure with a cubic symmetry, the stiffness matrix can be reduced and Eq. 2.16 can be written as [82] :

$$\begin{pmatrix} \sigma_{xx} \\ \sigma_{yy} \\ \sigma_{zz} \\ \sigma_{yz} \\ \sigma_{xz} \\ \sigma_{xy} \end{pmatrix} = \begin{pmatrix} c_{11} & c_{12} & c_{12} & 0 & 0 & 0 \\ c_{12} & c_{11} & c_{12} & 0 & 0 & 0 \\ c_{12} & c_{12} & c_{11} & 0 & 0 & 0 \\ 0 & 0 & 0 & c_{44} & 0 & 0 \\ 0 & 0 & 0 & 0 & c_{44} & 0 \\ 0 & 0 & 0 & 0 & 0 & c_{44} \end{pmatrix} \begin{pmatrix} \epsilon_{xx} \\ \epsilon_{yy} \\ \epsilon_{zz} \\ \epsilon_{yz} \\ \epsilon_{xz} \\ \epsilon_{xy} \end{pmatrix}, \tag{2.17}$$

where x, y, z denote the crystal directions and c_{11}, c_{12} and c_{44} are elastic constants of the material.

The reduced stiffness matrix in Eq. 2.17 can be expressed using the material constants namely Poisson's ratio $\nu_{ij} = -\epsilon_{jj}/\epsilon_{ii}$, Young's modulus $E_i = \sigma_{ii}/\epsilon_{ii}$ and shear modulus $G_{ij} = \sigma_{ij}/\epsilon_{ij}$ as [83]:

$$C = \begin{pmatrix} \frac{1-\nu_{yz}\nu_{zy}}{E_y E_z \Delta} & \frac{\nu_{yx}+\nu_{yz}\nu_{zy}}{E_y E_z \Delta} & \frac{\nu_{zx}+\nu_{yz}\nu_{zy}}{E_y E_z \Delta} & 0 & 0 & 0 \\ \frac{\nu_{xy}+\nu_{xz}\nu_{zy}}{E_y E_x \Delta} & \frac{1-\nu_{yx}\nu_{xz}}{E_y E_x \Delta} & \frac{\nu_{zy}+\nu_{yx}\nu_{xy}}{E_x E_z \Delta} & 0 & 0 & 0 \\ \frac{\nu_{xz}+\nu_{xy}\nu_{yz}}{E_x E_y \Delta} & \frac{\nu_{yz}+\nu_{xz}\nu_{yx}}{E_x E_y \Delta} & \frac{1-\nu_{xy}\nu_{yx}}{E_x E_y \Delta} & 0 & 0 & 0 \\ 0 & 0 & 0 & G_{yz} & 0 & 0 \\ 0 & 0 & 0 & 0 & G_{zx} & 0 \\ 0 & 0 & 0 & 0 & 0 & G_{xy} \end{pmatrix}, \tag{2.18}$$

where $\Delta = \frac{1-\nu_{xy}\nu_{yx}-\nu_{yz}\nu_{zy}-\nu_{zx}\nu_{zx}-2\nu_{xy}\nu_{yz}\nu_{xz}}{E_x E_y E_z}$.

The inverse of the stiffness matrix gives the compliance matrix S and relates

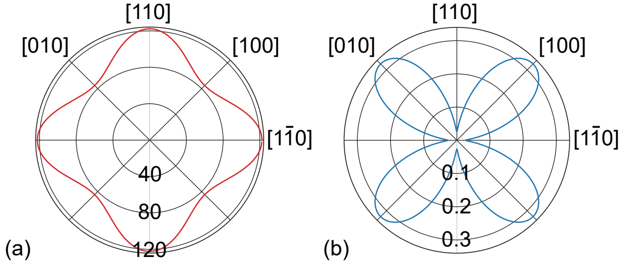

Figure 2.4: Anisotropic Young's modulus and Poisson ration. Estimated values for (a) Young's modulus $E(\theta)$ (in GPa) and (b) Poisson's ratio $\nu(\theta)$ for $\mathrm{In}_{1-x}\mathrm{Ga}_x\mathrm{P}$ for $x = 0.5685$. Image taken from [33].

the strain and stress via the relation $\epsilon_{ij} = S_{ijkl}\sigma_{kl}$, where

$$S = \begin{pmatrix} \frac{1}{E_x} & -\frac{\nu_{yx}}{E_y} & -\frac{\nu_{zx}}{E_z} & 0 & 0 & 0 \\ -\frac{\nu_{xy}}{E_x} & \frac{1}{E_y} & -\frac{\nu_{zy}}{E_z} & 0 & 0 & 0 \\ -\frac{\nu_{xz}}{E_x} & -\frac{\nu_{yz}}{E_y} & \frac{1}{E_z} & 0 & 0 & 0 \\ 0 & 0 & 0 & \frac{1}{G_{yz}} & 0 & 0 \\ 0 & 0 & 0 & 0 & \frac{1}{G_{zx}} & 0 \\ 0 & 0 & 0 & 0 & 0 & \frac{1}{G_{xy}} \end{pmatrix}. \tag{2.19}$$

Young's modulus of the material along the x crystal direction is given by $E_x = 1/s_{11}$. The Young's modulus along different crystal directions can be obtained by rotating the matrix in the crystal plane [31], [33], [84]. Similarly, one also obtains the crystal direction dependent Poisson's ratio. In Fig. 2.4 , we see the crystal direction dependent Young's modulus $E(\theta)$ and Poisson's ratio $\nu(\theta)$ for InGaP in the (0 0 1) plane [31], [33].

Similar to the material properties, i.e., Young's modulus and Poisson's ratio, the stress in the material is also crystal direction dependent. For materials where the concentration between elements can be varied, for e.g., $\mathrm{In}_{1-x}\mathrm{Ga}_x\mathrm{P}$ and $\mathrm{Al}_{1-x}\mathrm{Ga}_x\mathrm{As}$, the stress is also dependent on the Ga content x. Therefore the anisotropic stress in the device layer is given by [31], [33]:

$$\sigma(\theta, x) = E(\theta, x)\,\epsilon(x). \tag{2.20}$$

2.1.3 Dissipation dilution

In materials with tensile stress, the intrinsic dissipation can be diluted by the process called 'dissipation dilution'. The addition of tensile stress to the resonator increases the energy stored in the mechanical resonator as seen in Eq. 2.14. The effect can be seen as an enhancement of Q_{int} by a factor called 'dilution factor', D. The enhanced quality factor, Q_D is given by [10], [73], [78]:

$$Q_{\mathrm{D}} = D \cdot Q_{\mathrm{int}}, \tag{2.21}$$

and D is given by [73]

$$D = 1 + \frac{W_{\mathrm{tensile}}}{W_{\mathrm{elongation}} + W_{\mathrm{bending}}}. \tag{2.22}$$

For micromechanical resonators where $h \ll L$ where h and L are the thickness and length of the resonator respectively, the $W_{\mathrm{elongation}} \ll W_{\mathrm{bending}}$. Therefore, we can approximate the dilution factor to a purely geometric term. For a uniform string resonator, D is given by [10], [73], [85]

$$D_n = \frac{1}{2\lambda + (\pi n)^2 \lambda^2}, \tag{2.23}$$

where n is the mode number and λ is a stress parameter:

$$\lambda = \frac{h}{L}\sqrt{\frac{E}{12\,\sigma}}. \tag{2.24}$$

Using Eq. 2.23, one can calculate the intrinsic quality factor of the material which we will use in Sec. 4.2.1.

2.2 Optical Resonators

Optical resonators are cavities formed by two or more mirrors. When light enters the cavity, it resonates between the mirrors via reflection and forms a standing wave inside the cavity as seen in Fig. 2.5. These standing waves

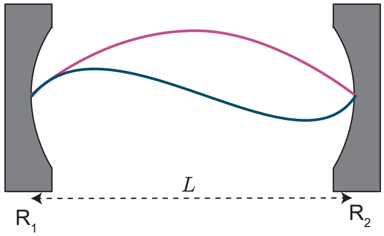

Figure 2.5: Schematic of showing an optical cavity formed between two mirrors with reflectance R_1 and R_2. The cavity length is L. The first two modes, n = 1 (purple) and n = 2 (blue), are shown.

are the optical cavity modes. A Fabry-Pérot (FP) cavity consisting of two weakly transmissive mirrors is the most commonly known optical cavity. The resonances of a FP cavity are given by [86], [87]:

$$\omega_{\text{cav}} = n\frac{\pi c}{L}, \tag{2.25}$$

where n is the integer mode number of cavity resonance, c is the speed of light and L is the length of the cavity. As evident from Eq. 2.25, the resonance of the FP cavity are equally spaced in frequency. The difference between two resonances is the free spectral range of the cavity [86], [87]:

$$\omega_{\text{FSR}} = \frac{\pi c}{L}. \tag{2.26}$$

The transmission profile of an optical cavity is Lorentzian as seen in Fig. 2.6 [87]. The linewidth of the Lorentzian, κ is determined by the sum of all the optical losses in the cavity. Another important quantity that is used to characterize an optical cavity is its finesse $\mathscr{F}$. The finesse can be described as the number of round trips that a photon takes in the cavity before exiting it. The finesse can be calculated by [86], [87]:

$$\mathscr{F} = \frac{\omega_{\text{FSR}}}{\kappa} = \frac{\pi c}{\kappa L} = \frac{\pi\sqrt{\mid r_1 r_2 \mid}}{1- \mid r_1 r_2 \mid}, \tag{2.27}$$

where r_1 and r_2 are the reflection coefficients of the two mirrors.

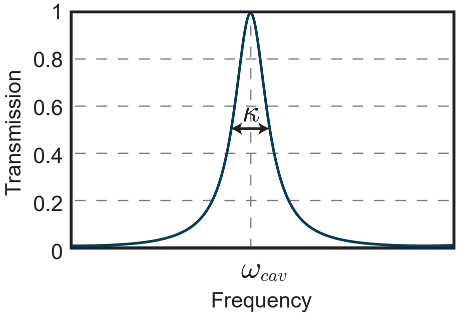

Figure 2.6: The Lorentzian shape of the transmission of the optical cavity formed by two mirrors. The optical losses are denoted by the linewidth of the Lorentzian calculated at full-width half maximum, κ.

Assuming an input light field incident on one of the mirrors, the transmission of the cavity can be calculated as the ratio of the output and input intensities. The final expression following the derivation from Refs. [86], [87] is given as

$$T = \frac{I_{\text{out}}}{I_{\text{in}}} = \frac{(1-R_1)(1-R_2)}{(1-\sqrt{R_1R_2})^2 + 4\sqrt{R_1R_2}\sin^2(\phi)}, \tag{2.28}$$

where $R_1 =\mid r_1 \mid^2$ and $R_2 =\mid r_2 \mid^2$ are the reflectance of the two individual mirrors and ϕ is the phase that the light field acquires while traveling in the cavity and is given by

$$\phi = kL = \frac{2\pi L}{\lambda}. \tag{2.29}$$

As seen in Fig. 2.7 (a), the transmission of the cavity reaches unity at resonance if the two mirrors have the same reflectance. Also, the linewidth of the cavity becomes narrower as the reflectance increases. In other words, a high finesse cavity can be formed with high reflectance mirrors. In Fig. 2.7 (b), we can observe that the transmission reduces as the reflectance mismatch between the two mirrors increases.

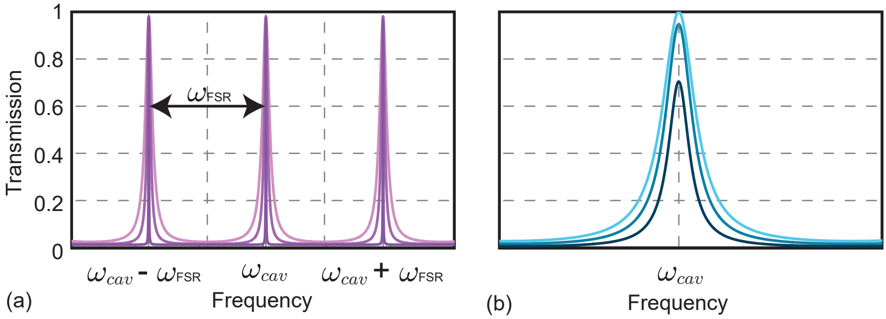

Figure 2.7: (a) Transmission for an optical cavity where the reflectance of the mirrors varies from $R_1 = R_2 = 0.8, 0.9, 0.99$ (lighter to darker). (b) Transmission for an optical cavity where the reflectance of one of the mirrors is kept constant, $R_1 = 0.7$ and the reflectance R_2 varies $R_2 = 0.7, 0.8, 0.9$ (lighter to darker).

2.3 Cavity Optomechanics

In the previous sections we have described mechanical and optical resonators as independent entities. In the following section, we discuss a cavity optomechanical system where an optical resonator (Sec. 2.2) is coupled to a mechanical resonator (Sec. 2.1).

2.3.1 Optomechanical Hamiltonian

We begin with the discussion on cavity optomechanics by describing the optomechanical Hamiltonian, following the review on cavity optomechanics by Aspelmeyer et al., Ref. [3]. For uncoupled mechanical and optical harmonic oscillators, the Hamiltonian is:

$$\hat{H}_0 = \hbar\omega_{\text{cav}}\hat{a}^\dagger\hat{a} + \hbar\omega_m\hat{b}^\dagger\hat{b}, \tag{2.30}$$

where $\hat{a}^\dagger$ ($\hat{b}^\dagger$) and $\hat{a}$ ($\hat{b}$) are the photon (phonon) creation and annihiliation operators respectively, ω_{cav} and ω_m are the optical and mechanical angular frequencies, respectively.

When one of the mirrors oscillates, the mechanical and optical modes couple since ω_{cav} depends on the mirror position x seen in Fig. 2.1. Assuming small displacements around the equilibrium position of the mirror at a cavity length L, we can perform a Taylor expansion on ω_{cav} to obtain :

$$\omega_{\text{cav}}(x) \approx \omega_{\text{cav}} + x\frac{\partial \omega_{\text{cav}}}{\partial x} + \mathcal{O}(x)^2 + ... \tag{2.31}$$

Neglecting the higher order terms, we consider the linear term as the frequency shift per displacement $G = -\partial\omega_{\text{cav}}/\partial x$. Inserting Eq. 2.31 into Eq. 2.30, we get the optomechanical Hamiltonian as

$$\begin{aligned} \hat{H} &= \hbar(\omega_{\text{cav}} - G\hat{x})\hat{a}^\dagger\hat{a} + \hbar\omega_{\text{m}}\hat{b}^\dagger\hat{b} && (2.32\text{a}) \\ &= \hbar\omega_{\text{cav}}\hat{a}^\dagger\hat{a} + \hbar\omega_{\text{m}}\hat{b}^\dagger\hat{b} - \hbar G\hat{x}\hat{a}^\dagger\hat{a} && (2.32\text{b}) \\ &= \hat{H}_0 - \hbar G\hat{x}\hat{a}^\dagger\hat{a}. && (2.32\text{c}) \end{aligned}$$

The first two terms in Eq. 2.32a(b) are recognized to part of the bare Hamiltonian. The last term is the interaction Hamiltionian

$$\begin{aligned} \hat{H}_{\text{int}} &= -\hbar G\hat{x}\hat{a}^\dagger\hat{a}, && (2.33\text{a}) \\ &= -\hbar g_0\hat{a}^\dagger\hat{a}(\hat{b} + \hat{b}^\dagger), && (2.33\text{b}) \end{aligned}$$

where we introduce the mechanical displacement operator $\hat{x} = x_{\text{zpf}}(\hat{b} + \hat{b}^\dagger)$ and the single-photon optomechanical coupling strength $g_0 = Gx_{\text{zpf}}$ [3]. x_{zpf} denotes the zero-point-fluctuation of the mechanical resonator i.e., the oscillations of the mirror in its ground state. It is given by:

$$x_{\text{zpf}} = \sqrt{\frac{\hbar}{2m_{\text{eff}}\omega_m}}, \tag{2.34}$$

where m_{eff} is the effective mass of the mechanical resonator, g_0 is the measure of the interaction between a single photon and a single phonon. In other words, g_0 is the cavity frequency shift that occurs due to one photon interacting with the moving mirror. The radiation pressure force that the mirror experiences due to the interaction with the photons in the cavity is

$$\hat{F}_{\mathrm{rad}} = -\frac{d\hat{H}_{\mathrm{int}}}{d\hat{x}} = \hbar G \hat{a}^{\dagger}\hat{a}. \tag{2.35}$$

The single-photon optomechanical interaction strength can be enhanced by having a large number of photons in the cavity. This can be achieved by high finesse optical cavities. In the situation described above, we have a strong intra-cavity field which can be described as a $\hat{a} = \alpha + \delta\hat{a}$. α is the mean field and $\delta\hat{a}$ are the fluctuations around this mean value. Then, the interaction Hamiltonian can be linearized [3] and one obtains,

$$\hat{H}_{\mathrm{int}}^{\mathrm{lin}} = -\hbar g(\delta\hat{a} + \delta\hat{a}^{\dagger})(\hat{b} + \hat{b}^{\dagger}), \tag{2.36}$$

where $g = g_0\alpha = g_0\sqrt{n_{\mathrm{cav}}}$, and n_{cav} is the number of photons circulating in the optical cavity.

The optomechanical theory discussed thus far is also referred to as dispersive optomechanics wherein the optical cavity frequency $\omega_{\mathrm{cav}}(x)$ changes with the position x of the movable mirror. There exists also dissipative optomechanics where the optical cavity loss rate $\kappa(x)$ changes with the position of the mirror x, which is discussed in Refs. [67], [88], [89].

2.3.2 Quantum Langevin equations

The oscillation of the mechanical resonator modulates the cavity frequency and the corresponding optical field. Consequently, the radiation pressure force acting on the mechanical resonator changes, which modifies the resonator position. This cycle continues as long as the optical cavity is populated with photons. The finite cavity decay rate introduces a delay between mechanical motion and the radiation pressure force. This feedback loop is called the 'dynamical optomechanical backaction'. To model the dynamics of the optomechanical system and the corresponding effects, we use the Langevin equations of the system. Langevin equations are useful to determine the evolution of quantum operators under the influence of stochastic forces. The equations of motion for the cavity field amplitude $\hat{a}$ and the mechanical amplitude $\hat{b}$ seen

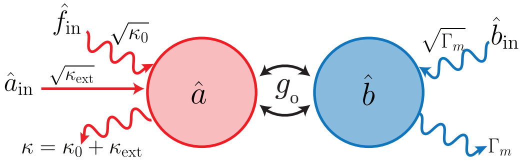

Figure 2.8: Schematic of a canonical optomechanical system. The optical mode $\hat{a}$ and the mechanical mode $\hat{b}$ are coupled by the single-photon optomechanical coupling strength g_0. The optical and mechanical modes are coupled to the noise operators $\hat{f}_{\mathrm{in}}$ and $\hat{b}_{\mathrm{in}}$ with the rates κ_0 and Γ_m, respectively. The cavity is driven with the field $\hat{a}_{\mathrm{in}}$ coupling to the cavity with the rate κ_{ext}. The optical and mechanical modes dissipate to the environment with a rate of $\kappa = \kappa_0 + \kappa_{\mathrm{ext}}$ and Γ_m, respectively.

in Fig. 2.8 are given by [3], [74], [90]:

$$\dot{\hat{a}} = -(\kappa - i\Delta_a^0)\hat{a} + ig_0\hat{a}\hat{x} + \sqrt{2\kappa_{\mathrm{ex}}}\hat{a}_{\mathrm{in}} + \sqrt{2\kappa_0}\hat{f}_{\mathrm{in}}, \tag{2.37a}$$

$$\dot{\hat{b}} = -(\frac{\Gamma_m}{2} + i\omega_{\mathrm{m}})\hat{b} + ig_0\hat{a}^\dagger\hat{a} + \sqrt{\Gamma_m}\hat{b}_{\mathrm{in}}, \tag{2.37b}$$

where $\Delta_a^0 = \omega_l - \omega_{\mathrm{cav}}$, the optical and mechanical modes are coupled to the noise operators $\hat{f}_{\mathrm{in}}$ and $\hat{b}_{\mathrm{in}}$ with the rates κ_0 and Γ_m, respectively. The cavity is driven with the field $\hat{a}_{\mathrm{in}}$ coupling to the cavity with the rate κ_{ext}. Eq. 2.37 are nonlinear and can be linearized similar to Eq. 2.36 resulting in the set of linearized equations of motion [3]:

$$\delta\dot{\hat{a}} = (i\Delta_a - \kappa)\delta\hat{a} + ig(\hat{b} + \hat{b}^\dagger) + \sqrt{2\kappa_{\mathrm{ex}}}\delta a_{\mathrm{in}} + \sqrt{2\kappa_0}\hat{f}_{\mathrm{in}}, \tag{2.38a}$$

$$\dot{\hat{b}} = -(\frac{\Gamma_m}{2} + i\omega_{\mathrm{m}})\hat{b} + ig(\delta\hat{a} + \delta\hat{a}^\dagger) + \sqrt{\Gamma_m}\hat{b}_{\mathrm{in}}, \tag{2.38b}$$

$\Delta_a = \Delta_a^0 - \frac{g_0^2|\alpha|^2}{\omega_m}$ which is the detuning taking the radiation pressure effects into account.

Optical spring effect and optomechanical damping

The effect of the optomechanical coupling on the mechanical resonator can be calculated by solving the linearized equations of motions in Eq. 2.38. Firstly, we consider the classical averaged form of Eq. 2.37 given by [3]:

$$\dot{\alpha} = (i\Delta_a - \frac{\kappa}{2})\alpha + iGx + \sqrt{\kappa_{\mathrm{ex}}}\alpha, \tag{2.39a}$$

$$m_{\mathrm{eff}}\ddot{x} = -m\Gamma_m\dot{x} - m\omega_{\mathrm{m}}x + G\hbar \mid \alpha \mid^2, \tag{2.39b}$$

where $\alpha(t) = \langle\hat{a}(t)\rangle$, $x(t) = \langle\hat{x}(t)\rangle$, $x = 2x_{\mathrm{zpf}}\Re\,[\langle\hat{b}\rangle]$ with the assumption that $\Gamma_m \ll \omega_{\mathrm{m}}$ which is true in almost all mechanical systems.

Solving Eq. 2.39 for the effective mechanical susceptibility $\chi_{\mathrm{m,eff}}(\omega)$ in frequency space (similar to Eq. 2.3):

$$\chi_{\mathrm{m,eff}}(\omega) = \frac{1}{m_{\mathrm{eff}}[\omega_{\mathrm{m}}^2 + 2\omega\delta\omega_{\mathrm{m}}(\omega) - \omega^2 - i\omega(\Gamma_m + \Gamma_{\mathrm{opt}}(\omega))]}. \tag{2.40}$$

We see that the effective mechanical susceptibility (Eq. 2.40) is similar to the unperturbed mechanical susceptibility (Eq. 2.3) except for two terms, i.e., $\delta\omega_{\mathrm{m}}(\omega)$ and $\Gamma_{\mathrm{opt}}(\omega)$. $\delta\omega_{\mathrm{m}}(\omega)$ is the mechanical frequency modification of the resonator by the optical spring effect and $\Gamma_{\mathrm{opt}}(\omega)$ is the optomechanically induced damping. These modifications to the mechanical frequency and damping are given by [3]:

$$\delta\omega_{\mathrm{m}}(\omega) = g^2\frac{\omega_{\mathrm{m}}}{\omega}\left(\frac{\Delta_a + \omega}{(\Delta_a + \omega)^2 + (\frac{\kappa}{2})^2} + \frac{\Delta_a - \omega}{(\Delta_a - \omega)^2 + (\frac{\kappa}{2})^2}\right), \tag{2.41a}$$

$$\Gamma_{\mathrm{opt}}(\omega) = g^2\frac{\omega_{\mathrm{m}}}{\omega}\left(\frac{\kappa}{(\Delta_a + \omega)^2 + (\frac{\kappa}{2})^2} - \frac{\kappa}{(\Delta_a - \omega)^2 + (\frac{\kappa}{2})^2}\right). \tag{2.41b}$$

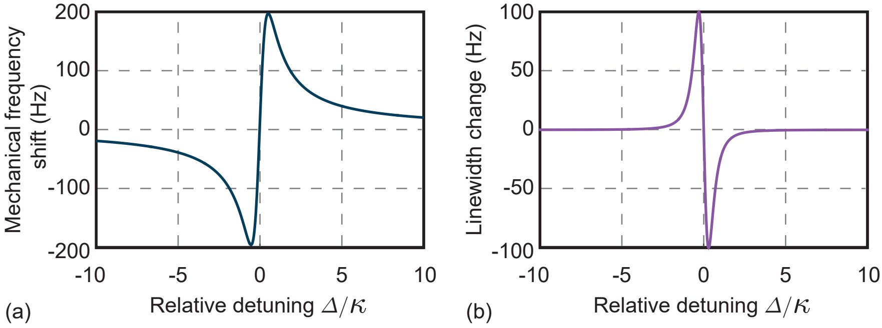

Figure 2.9: Optical spring effect and optomechanical damping. (a) The mechanical frequency shift due to the optical spring effect, The frequency reduces (increases) for red-detuning (blue-detuning). (b) The change in the damping rate of the mechanical resonator due to detuning leading to optomechanical damping. The parameters used in the calculations were: $\omega_\mathrm{m} = 2\pi \cdot 100\,\mathrm{kHz}$, $\mathrm{g} = 2\pi \cdot 10\,\mathrm{kHz}$ and $\kappa = 10\omega_\mathrm{m}$.

Optical spring effect At $\omega = \omega_\mathrm{m}$, we find the light field induced mechanical frequency shift $\delta\omega_\mathrm{m}(\omega_m)$:

$$\delta\omega_\mathrm{m} = g^2 \left(\frac{\Delta_a + \omega_\mathrm{m}}{(\Delta_a + \omega_\mathrm{m})^2 + (\frac{\kappa}{2})^2} + \frac{\Delta_a - \omega_\mathrm{m}}{(\Delta_a - \omega_\mathrm{m})^2 + (\frac{\kappa}{2})^2} \right). \tag{2.42}$$

In Eq. 2.42 and shown in Fig. 2.9(a), we observe that for a red-detuning ($\Delta < 0$), the frequency reduces corresponding to a spring softening, and for a blue-detuning ($\Delta > 0$) the frequency increases corresponding to the spring hardening.

Optomechanical damping In the same approximation as above, i.e., $\omega = \omega_\mathrm{m}$, the optomechanical damping is given by:

$$\Gamma_\mathrm{opt} = g^2 \left(\frac{\kappa}{(\Delta_a + \omega_\mathrm{m})^2 (\frac{\kappa}{2})^2} - \frac{\kappa}{(\Delta_a - \omega_\mathrm{m})^2 + (\frac{\kappa}{2})^2} \right). \tag{2.43}$$

The overall mechanical damping of the system is given by $\Gamma = \Gamma_m + \Gamma_\mathrm{opt}$. Since Γ_opt can be either positive or negative based on the detuning of the laser frequency with respect to the cavity resonance, we can either increase or decrease the overall damping seen in Fig. 2.9(b). This means, on one hand, when $\Gamma_{\text{opt}} > 0$, the system can be cooled. On the other hand, if $\Gamma_{\text{opt}} < 0$ and $\Gamma > 0$, the system can be heated. It has to be noted that if $\Gamma < 0$, the system becomes unstable. Optomechanical cooling is discussed in detail in Ref. [3].

2.3.3 Photothermal optomechanics

We see in Sec. 4.1.3, that the conventional dispersive optomechanical theory discussed above does not explain the mechanical frequency shift observed. Therefore we explore optomechanics that occur due to the absorption of the photon called photothermal optomechanics. However, the mechanical resonators are realized in semiconductor materials in this thesis. The incident light is in the bandgap of the material. Therefore, the photon should not get absorbed. Nonetheless, we discuss the frequency shift expected due to photothermal optomechanics.

In photothermal optomechanics, photons that are absorbed by the mechanical resonator lead to thermo-elastic effects which displace the resonator [91], [92]. The absorbed power by the mechanical resonator is given by (described in detail in Ref. [91]):

$$P_{\text{abs}}(x) = \left(1 + 4x\frac{\Delta_0\omega_l}{L(\kappa^2+\Delta_a^2)}\right)\frac{TA/\tau_0^2}{\kappa^2+\Delta_a^2}P_{\text{inc}}, \tag{2.44}$$

where A is the absorption coefficient, T is the transmittance, $\tau_0 = \frac{2L}{c}$ and P_{inc} is the incident power. The effective mechanical frequency of the mechancical resonator under photothermal effects is given by [91]

$$\omega_{\text{eff}} = \omega_m^2\left(1 - \beta\frac{1}{1+\omega_m^2\tau_{\text{th}}^2}\frac{2R}{c}\frac{dP_{\text{abs}}(x)}{dx}\frac{1}{K}\right), \tag{2.45}$$

where τ_{th} is the thermal relaxation time, R is the reflectance, and K is the spring constant of the reflector.

2.4 Optical cavities with frequency-dependent reflectors

2.4.1 Photonic Crystals

The mechanical resonators used in this thesis are realized from thin-film dielectrics. These thin-films usually do not possess high reflectivity above 99% which is required to form an efficient optomechanical system. Additionally, it aids for an efficient transduction of the mechanics to the optical light field. A 100 nm-thick layer of GaAs has a reflectance of $\approx 70\%$. To enhance the reflectance we utilize photonic crystals (PhC). PhCs are periodic structures that lead to a refractive index contrast. The periodic changes in the refractive index form a photonic bandgap in the material akin to the energy bandgap formed in semiconductors due to the lattice structure of the material [59], [63], [93].

Guided modes and guided resonances exist in a PhC structure [59]. The guided modes lie below the light line and are similar to dark modes. These guided modes do not couple to external radiation. The guided resonances are above the light line and are leaky. Therefore, the guided resonances can couple to external radiation. Light incident on the PhC can interact with the PhC in two ways shown in Fig. 2.10. First (i), there can be a direct transmission through the PhC slab. Second (ii), the incident light can couple into the guided resonance. A destructive interference can occur between these two light paths leading to all the incident light being reflected back. This response can be modeled as a Fano resonance leading to an asymmetric lineshape for the resonance [59], [60].

Considering a single guided resonance in a PhC slab, the transmission and reflection amplitude of the PhC can be expressed as [59]:

$$t_F(\omega) = t_d(\omega) + f\frac{\gamma}{-i(\omega-\omega_F)+\gamma_d}, \tag{2.46a}$$

$$r_F(\omega) = r_d(\omega) + s\cdot f\frac{\gamma}{-i(\omega-\omega_F)+\gamma_d}, \tag{2.46b}$$

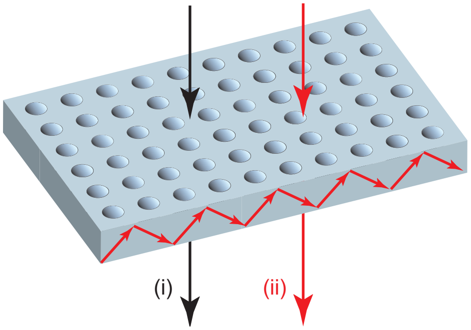

Figure 2.10: Schematic showing the two optical paths the light incident on the PhC can take. Direct transmission through the PhC and coupling into the guided resonance.

where t_d and r_d are the direct transmission and reflection coefficients respectively, ω_d is the angular frequency of the guided resonance and γ its linewidth, f is the complex amplitude of the guided resonance where $f = -(t_d + s\ r_d)$ and s indicates the even $(s = 1)$ or odd $(s = -1)$ symmetry of the guided resonance with respect to the mirror plane in the center of the PhC parallel to the face. The reflection and transmission coefficients in Eq. 2.46 can be rewritten as

$$t_F(\omega) = \frac{-2s\gamma_d r_d(\omega) - i\Delta_F t_d(\omega)}{-i\Delta_F + 2\gamma_d}, \tag{2.47a}$$

$$r_F(\omega) = \frac{-2s\gamma_d t_d(\omega) - i\Delta_F r_d(\omega)}{-i\Delta_F + 2\gamma_d}. \tag{2.47b}$$

where $\Delta_F = \omega - \omega_d$. The reflectance of a PhC exhibiting an asymmetric profile is shown in Fig. 2.11. We see that the reflectance of the PhC can be engineered to give high reflectance at certain wavelengths.

2.4.2 Transfer matrix modeling

The optical properties of the cavity can be modeled using analytical methods. The models help us to characterize the optical properties of the system and

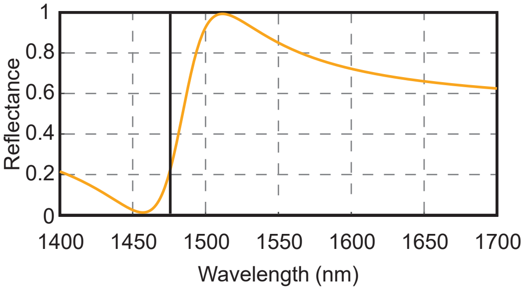

Figure 2.11: The reflectance of a PhC with $r = 418\,\text{nm}$, $a = 1081\,\text{nm}$ and $d = 75\,\text{nm}$ in vacuum showing the Fano lineshape. The vertical line shows the resonance wavlength of the guided resonance $\lambda_0 = 2\pi c/\omega_d$.

also individual elements. It also allows us to simulate the expected optical behavior of an optical system. Here, we discuss transfer matrix modeling.

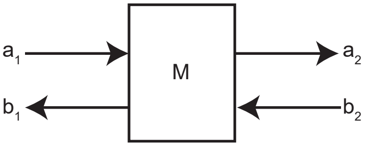

Figure 2.12: Schematic of an optical system with the transfer matrix M that describes its optical properties.

The transfer matrix method is a commonly used to analyze the propagation, transmission and reflection of the electromagnetic field in a material stack [86], [87]. As seen in Fig. 2.12, considering an optical system where electromagnetic field on one side is related to the other side with a characteristic transfer matrix M given by [86], [87]

$$\begin{pmatrix} a_2 \\ b_2 \end{pmatrix} = M \begin{pmatrix} a_1 \\ b_1 \end{pmatrix}. \tag{2.48}$$

The reflection coefficient of the system is given by $r = \frac{M_{2,1}}{M_{1,1}}$ and transmission coefficient is given by $t = \frac{1}{M_{1,1}}$. For a combination of multiple optical elements, the total transfer matrix of the system M_{tot} is given by $M_{\text{tot}} = M_1 M_2 M_3 ... M_N$. The transfer matrix of each element is given by M_N

where $n = 1, 2, 3.., N$.

The mirrors in the system can be modeled as thin one-dimensional scatterers. For a thin-scatterer, the transfer matrix is given by [93]

$$M = \frac{1}{t}\begin{bmatrix} 1 & -r \\ r & t^2 - r^2 \end{bmatrix}. \tag{2.49}$$

Alternatively, the transmission and reflection coefficient of a one-dimensional scatterer can also be described by its polarizability ζ given by [93]

$$\zeta = \frac{r}{it}, \tag{2.50}$$

where both r and t are complex numbers. We also express r and t in terms of ζ as follows:

$$r = \frac{i\zeta}{1 - i\zeta}, \tag{2.51}$$

$$t = \frac{1}{1 - i\zeta}. \tag{2.52}$$

By using Eq. 2.51 and Eq. 2.52, we obtain the relation

$$t = 1 + r. \tag{2.53}$$

The following conditions must also be satisfied such that r and t fulfill energy conservation [93]

$$\begin{aligned} |r|^2 + |t|^2 &= 1, \\ rt^* + r^*t &= 0. \end{aligned} \tag{2.54}$$

Hence, one can rewrite r, t and ζ as

$$r = i \sin\phi e^{i\phi}, \tag{2.55}$$

$$t = \cos\phi e^{i\phi}, \tag{2.56}$$

$$\zeta = \tan\phi. \tag{2.57}$$

The PhCs fabricated in this work have dimensions less than 100 nm. Since the incident wavelength is larger than the thickness of the PhC, the one-dimensional scatterer modeling is also valid for the case of a PhC [60], [68], [69]. The polarizability of the frequency dependent reflector is given by

$$\zeta_F(\omega) = \frac{1}{-i} \frac{-2s\gamma_d t_d - i\Delta_F r_d}{-2s\gamma_d r_d - i\Delta_F t_d}. \tag{2.58}$$

Revisiting Eq. 2.49, the transfer matrix of a scatterer in terms of its polarizability is given by [93]

$$M_\zeta = \begin{bmatrix} 1 - i\zeta & -i\zeta \\ i\zeta & 1 + i\zeta \end{bmatrix}. \tag{2.59}$$

Similarly, the transfer matrix describing propagation in a material with thickness d and refractive index n is given by [69], [86], [87]:

$$M_{\text{prop}} = \begin{bmatrix} e^{iknd} & 0 \\ 0 & e^{-iknd} \end{bmatrix}, \tag{2.60}$$

where $k = 2\pi/\lambda$ is the wavevector.

The transfer matrix of a PhC-DBR system is then obtained as $M_{\text{PhC-DBR}} = M_{\text{PhC}} \cdot M_{\text{prop}} \cdot M_{\text{DBR}}$. The transmission coefficient of the PhC-DBR system is given by

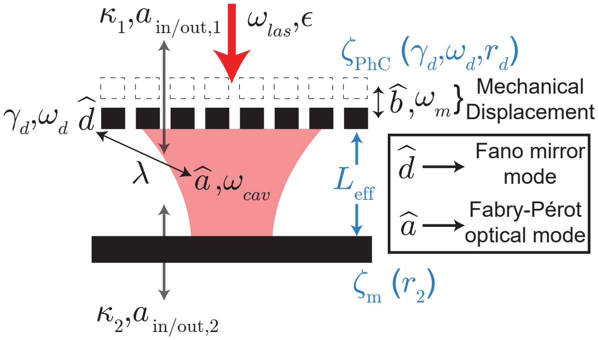

Figure 2.13: Schematic of the optomechanical system with a frequency-dependent reflector.

$$t_{PhC-DBR}(\omega) = \frac{1}{M(1,1)} = \frac{1}{(1 - i\zeta_F(\omega))(1 - i\zeta_m)e^{i\Phi} + \zeta_m \zeta_F(\omega) e^{-i\Phi}}, \tag{2.61}$$

where ζ_F (ζ_m) is the polarizability of the frequency-dependent (-independent) reflector and Φ is the phase acquired by the light field during propagation in the microcavity.

The measured reflectance of the microcavity can be fit to Eq. 2.61 with ϕ and Φ as the free-parameters for the properties of the mirror and propagation respectively.

2.5 Optomechanics in frequency-dependent reflectors

2.5.1 Quantum Langevin equations

The optomechanical Hamiltonian discussed in Sec. 2.3.1 was described by assuming the reflectance of the mirrors was frequency-independent. However, since the reflectance of a PhC is highly frequency dependent, as seen in Fig. 2.11, one must revisit the cavity optomechanical theory to account for the presence of an frequency-dependent reflector. For this discussion, we consider a system which consists of a microcavity formed by a frequency-dependent PhC reflector (Fano mirror) and a mirror with constant reflectance in the frequency range of interest. The following Hamiltonian description follows the work of Ĉernotík et al (Refs. [69]) which was adapted to our system in colloboration with Juliette Monsel and is part of Paper D.

The total Hamiltonian $\hat{H}$ of the system seen in Fig. 2.13 is given by the sum of the standard optomechanical Hamiltonian (Eq. 2.32a), $\hat{H}_{\mathrm{OM}}$, and an additional term $\hat{H}_{\mathrm{F}}$ which is the internal mode of the Fano mirror (considered to be even) and its coupling to the cavity mode [69]:

$$\hat{H} = \hat{H}_{\mathrm{OM}} + \hat{H}_{\mathrm{F}}, \tag{2.62a}$$

$$\hat{H}_{\mathrm{OM}} = \hbar\omega_{\mathrm{m}}\hat{b}^\dagger\hat{b} + \hbar\Delta_a^0\hat{a}^\dagger\hat{a} - \hbar g_0\hat{a}^\dagger\hat{a}(\hat{b} + \hat{b}^\dagger), \tag{2.62b}$$

$$\hat{H}_{\mathrm{F}} = \hbar\Delta_d\hat{d}^\dagger\hat{d} + \hbar(\lambda^*\hat{a}^\dagger\hat{d} + \lambda\hat{a}\hat{d}^\dagger), \tag{2.62c}$$

where $\hat{d}^\dagger$ ($\hat{d}$) is the photon creation (annihilation) operator of the Fano mirror. We denote $\Delta_a^0 = \omega_{\mathrm{cav}} - \omega_l$ as the bare detuning between the cavity and the laser and $\Delta_d = \omega_d - \omega_l$ as the detuning between the Fano-mirror mode of frequency ω_d and the laser. The coupling strength between the Fano-mirror and cavity modes is denoted λ. Note that $*$ denotes the complex conjugate.

The mechanical resonator is coupled to a phonon bath with damping rate Γ_m. The cavity is coupled to two photon baths through the top (PhC) and bottom mirrors with optical loss rates κ_1 and κ_2, respectively. The Fano-mirror mode is coupled to the top bath only, with loss rate γ_d. The evolution of this system can be described with a set of Langevin equations [69], [90]:

$$\dot{\hat{q}} = \omega_{\mathrm{m}}\hat{p}, \tag{2.63a}$$

$$\dot{\hat{p}} = -\omega_{\mathrm{m}}\hat{q} - \Gamma_m\hat{p} + g_0\sqrt{2}\hat{a}^\dagger\hat{a} + \sqrt{\Gamma_m}\hat{\xi}, \tag{2.63b}$$

$$\dot{\hat{a}} = -(\kappa + i\Delta_a^0)\hat{a} + ig_0\sqrt{2}\hat{a}\hat{q} - \mathcal{G}_a\hat{d} + \sqrt{2\kappa_2}\hat{a}_{\mathrm{in},2} + \sqrt{2\kappa_1}(\alpha_{\mathrm{las}} + \hat{a}_{\mathrm{in},1}), \tag{2.63c}$$

$$\dot{\hat{d}} = -(\gamma_d + i\Delta_d)\hat{d} - \mathcal{G}_d\hat{a} + \sqrt{2\gamma_d}(\alpha_{\mathrm{las}} + \hat{a}_{\mathrm{in},1}), \tag{2.63d}$$

where we have defined the mechanical quadratures $\hat{q} = \left(\hat{b} + \hat{b}^\dagger\right)/\sqrt{2}$ and $\hat{p} = \left(\hat{b} - \hat{b}^\dagger\right)/i\sqrt{2}$ and denoted $\kappa = \kappa_1 + \kappa_2$ the total loss rate of the cavity. The laser driving the cavity is modeled as a classical drive of complex amplitude α_{las} and treated as part of the upper input field [94]. The input laser power P_{las} is given by $P_{\mathrm{las}} = \hbar\omega_l \mid \alpha_{\mathrm{las}} \mid^2 = \hbar\omega_l \frac{|\epsilon|^2}{2\kappa_1}$. The thermal noise of the mechanics is given by the operator $\hat{\xi}$, while the vacuum noise of the light field coming in from the top/bottom optical bath is associated with the operator $\hat{a}_{\mathrm{in},1/2}$. We have also defined $\mathcal{G}_a = i\lambda^* + \sqrt{\kappa_1\gamma_d}$ and $\mathcal{G}_d = i\lambda + \sqrt{\kappa_1\gamma_d}$, the detailed derivation can be found in Ref. [69].

The Langevin equations in Eq. 2.63 can be linearized similarly to Eq. 2.36. Here we consider the mean and some fluctuations around the mean for all operators, i.e, $\hat{a} = \alpha + \delta\hat{a}$, $\hat{q} = \bar{q} + \delta\hat{q}$, $\hat{p} = \bar{p} + \delta\hat{p}$ and $\hat{d} = \delta + \delta\hat{d}$, with $\bar{p} = 0$. The semiclassical steady state is then, given by

$$\alpha = \frac{\sqrt{2\kappa_1} - \mathcal{G}_a\sqrt{2\gamma_d}/(\gamma_d + i\Delta_d)}{\kappa + i\Delta_a - \mathcal{G}_a\mathcal{G}_d/(\gamma_d + i\Delta_d)}\alpha_{\mathrm{las}}, \tag{2.64a}$$

$$\bar{q} = \sqrt{2}\frac{g_0}{\omega_{\mathrm{m}}}|\alpha|^2, \tag{2.64b}$$

$$\delta = \frac{-\mathcal{G}_d\alpha + \sqrt{2\gamma_d}\alpha_{\mathrm{las}}}{\gamma_d + i\Delta_d}, \tag{2.64c}$$

where we have defined the effective detuning $\Delta_a = \Delta_a^0 - g_0\sqrt{2}\bar{q}$ and chosen the phase of α_{las} so that $\alpha = |\alpha|$ is real and positive. The linearized Langevin equations (first order in the fluctuations) are as follows,

$$\delta\dot{\hat{q}} = \omega_{\mathrm{m}}\delta\hat{p}, \tag{2.65a}$$

$$\delta\dot{\hat{p}} = -\omega_{\mathrm{m}}\delta\hat{q} - \Gamma_n\delta\hat{p} + g\sqrt{2}(\delta\hat{a}^\dagger + \delta\hat{a}) + \sqrt{\Gamma_m}\hat{\xi}, \tag{2.65b}$$

$$\delta\dot{\hat{a}} = -(\kappa + i\Delta_a)\delta\hat{a} + ig\sqrt{2}\delta\hat{q} - \mathcal{G}_a\delta\hat{d} + \sqrt{2\kappa_1}\hat{a}_{\mathrm{in},1} + \sqrt{2\kappa_2}\hat{a}_{\mathrm{in},2}, \tag{2.65c}$$

$$\delta\dot{\hat{d}} = -(\gamma_d + i\Delta_d)\delta\hat{d} - \mathcal{G}_d\delta\hat{a} + \sqrt{2\gamma_d}\hat{a}_{\mathrm{in},1}. \tag{2.65d}$$

The Langevin equations Eq. 2.65 can be rewritten in the frequency domain using Fourier transforms and be solved to obtain the mechanical susceptibility $\chi_{\mathrm{opt}}^{\mathrm{eff}}$ (similar to Eq. 2.3). We then obtain the expression for the mechanical frequency shift due to the optical spring effect as

$$\delta\omega_{\mathrm{m}}[\omega] = \frac{1}{2}\Re[\chi_{\mathrm{opt}}^{\mathrm{eff}}[\omega]^{-1}], \tag{2.66}$$

$$= -g^2\left(\frac{a_0(\gamma_d^2 + a_d^2) - \gamma_d a_\lambda\sqrt{\kappa_1\gamma_d} + a_d\kappa_1\gamma_d - |\lambda|^2 a_d}{[\kappa_2\gamma_d + |\lambda|^2 - a_d a_0]^2 + \left[a_d\kappa + a_0\gamma_d - a_\lambda\sqrt{\kappa_1\gamma_d}\right]^2} + (\omega \leftrightarrow -\omega)\right), \tag{2.67}$$

where $a_0 = \Delta_a - \omega$, $a_d = \Delta_d - \omega$ and $a_\lambda = \lambda + \lambda^*$.

2.5.2 Transmission using coupled-mode theory

The optomechanical modeling of the optical system described in Sec. 2.5.1 does not use polarizabilities. Hence, we need to describe the optical system using quantum optics parameters. We cannot directly experimentally access parameters such as the loss rates, the cavity frequency, the Fano resonance etc.. Therefore, we use coupled-mode theory to model the transmission and relate it to the transmission obtained by the transfer matrix method in Eq. 2.61.

The optical response of the frequency dependent optomechanical system is modeled by assuming a weak coupling regime, i.e., $g_0 \ll \kappa$ where the optomechanical coupling rate g_0 can be considered as a pertubation. In other words, the optomechanical effect has no discernible effect on the optical properties of the system. Hence, the terms with optomechanical coupling g_0 in Eq. 2.65(c) and (d) can be set to zero. The output fields are given by $\hat{a}_{\mathrm{out},1}[\omega] = \hat{a}_{\mathrm{in},1}[\omega] - \sqrt{2\gamma_d}\delta\hat{d}[\omega] - \sqrt{2\kappa_1}\delta\hat{a}[\omega]$ and $\hat{a}_{\mathrm{out},2}[\omega] = \hat{a}_{\mathrm{in},2}[\omega] - \sqrt{2\kappa_2}\delta\hat{a}[\omega]$. We can obtain the transmission coefficient of the system for the input field $\hat{a}_{\mathrm{in},1}[\omega]$ to the output field $\hat{a}_{\mathrm{out},2}[\omega]$ (when assuming $\hat{a}_{\mathrm{in},2}[\omega] = 0$) as [69]:

$$t(\omega) = \left\langle \frac{\hat{a}_{\mathrm{out},2}[\omega]}{\hat{a}_{\mathrm{in},1}[\omega]} \right\rangle\Bigg|_{\hat{a}_{\mathrm{in},2}[\omega]=0} = \frac{\sqrt{2\kappa_2}\left(\mathcal{G}_d\sqrt{2\gamma_d} - \sqrt{2\kappa_1}\chi_d[\omega]^{-1}\right)}{\chi_a[\omega]^{-1}\chi_d[\omega]^{-1} - \mathcal{G}_a\mathcal{G}_d}. \tag{2.68}$$

Using Eq. 2.68 and Eq. 2.61, we can extract the parameters of the optical system requried to model its optomechanial properties.

2.6 Bound states in a continuum

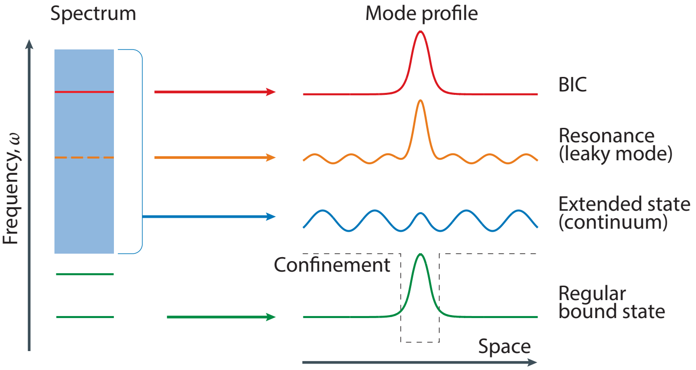

Figure 2.14: Illustration of a BIC. In an open system, the frequency spectrum consists of a continuum (blue) and discrete levels of bound states (green). The spatial confinement due to structure or potential is shown as the black dashed line. States inside the continuous spectrum either do not couple to the system (blue) or couple to the system becoming leaky resonances (orange). Bound states in the continuum (red) are special states that lie inside the continuum but remain localized with no radiation. Image taken from [95].

An electromagnetic wave can be confined within a system fully or partially. If the frequency of the wave is outside the continuum, then the mode is completely confined as it does not have a channel for the wave to radiate and is called a 'bound state'. Alternatively, if the wave is within the continuum, it is partially confined and is called a 'resonance' and can radiate away. A 'bound state in a continuum' (BIC) as the name states is a complete confinement of the mode without any losses within the continuum as seen in Fig. 2.14 [95].

In this thesis, we discuss an optical BIC which occurs due to destructive interference of different waves or modes in a system. The symmetry of the system plays a crucial role in determining the existence of a BIC [71]. Since the optical BIC has no loss channels, from the discussion on optical cavities in Sec. 2.2, it can be seen as an optical mode with $\kappa = 0$ and $Q = \infty$. In the context of cavity optomechanics, the introduction of a mechanical element inside an optical BIC would immediately place it in the single-photon strong coupling regime as $g_0 > \kappa$. The advantage of a BIC, i.e., it has no loss channels, is also a disadvantage as there is no possibility to access this mode. Therefore, the concept of ‘quasi-BIC’ is introduced [96], [97]. A quasi-BIC is a high-Q optical mode with loss channels that allow light to be coupled into the optical cavity.

CHAPTER 3

Methods

In this chapter, we describe the methods involved in designing, fabricating and measuring the devices used in this thesis. The optomechanical resonators should be designed to exhibit the desired mechanical and optical properties. We use different simulation methods to design the geometry, whereby finite element method simulations are primarily used to design the mechanical properties and rigourous coupled-wave analysis is used to design the optical properties. The fabrication of the micromechanical devices are performed in a cleanroom environment in several process steps. We discuss the fabrication process steps that are used to fabricate GaAs- and InGaP-based devices. We discuss the various techniques used to analyze the device quality during the course of fabrication. The fabricated devices are then characterized to determine the mechanical, optical and optomechanical properties of the devices. We discuss the different optical setups that are used to perform these measurements.

3.1 Simulation

3.1.1 Simulation of mechanical properties

The mechanical properties of a system that describe, for example how the material deforms and oscillates, are space- and time-dependent. These properties can be described by partial differential equations (PDEs). For simple geometries such as strings and membranes, these PDEs can be reduced to analytical models that faithfully capture the mechanical properties of the system [73]. But these analytical models are not available for more complex geometries like trampolines and membranes with photonic crystals that are used in this thesis. Hence, we utilize finite element method (FEM) as an alternative. An FEM simulation approximates the PDEs to numerical equations that can be solved numerically. FEM operates by dividing the geometry into smaller elements and solving the numerical equations for this element while also taking into account the solutions of its neighboring elements and in this manner the total solution for the system is calculated. The criteria for the subdivision of the geometry is determined by the density of meshing - the smaller the mesh, the more accurate the solution but the larger is the computational cost. In this thesis, we use COMSOL as the software platform to perform FEM simulations [98]. COMSOL is an appealing FEM software as it has the ability to combine multiple physical processes in the same simulation. Using COMSOL, we can estimate the static deformation [99], the stress-strain redistribution [8], [12], the mechanical eigenfrequencies of a released mechanical resonator [21]. We also use COMSOL to estimate the dilution factor [13]–[15], the clamping loss limited-quality factor Q_{clamp} of a resonator using perfectly matched layers [11], [78] and the thermo-elastic damping (TED) in the system to estimate Q_{TED}.

The simulations are constructed by building the geometry of the mechanical resonator in COMSOL and defining its material properties such as the elasticity matrix, Young's modulus, etc. The COMSOL simulation to compute the mechanical properties is performed in the 'Solid Mechanics' physics module. The structural properties of the resonator such as the initial material tensile stress and the faces of the mechanical resonator that are fixed are well-defined. The appropriate mesh size is selected based on the smallest size

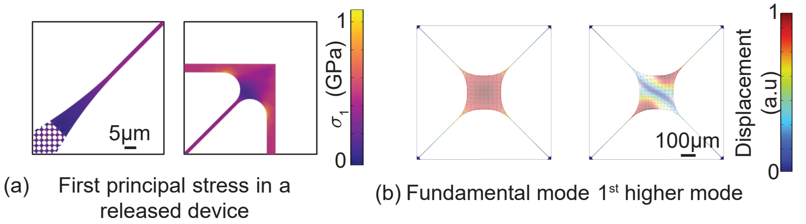

(a) First principal stress in a released device

(b) Fundamental mode 1st higher mode

Figure 3.1: FEM simulations of mechanical properties of mechanical resonator. (a) The stress distribution shown as the first principal stress of a released device showing stress concentration in the tether region. (b) The first two mechanical modes of a trampoline resonator with photonic crystal reflector. Images taken from [33]

in the geometry and the computational resource available. The study steps that compute the solution are done in two steps. In the first step, COMSOL calculates the static solution which encompasses the strain-stress distribution in the geometry after the release of the device as seen in Fig. 3.1(a). The stress redistribution results in a static deformation of the device. In the second step, the deformed geometry of the first step is used as the input to calculate the eigenfreqencies and the corresponding mode-shapes of the deformed geometry seen in Fig. 3.1(b) .

FEM simulations can also be used to calculate the dilution factor which quantifies the amount by which the mechanical dissipation is diluted. The dilution factor, D is dependent on the bending, elongation and tensile stress energies associated with the mode shape of the resonator [10], [73], [100]. The intrinsic quality factor of a resonator, Q_{int} that is experimentally measured can be enhanced by the dilution factor, leading to high-Q mechanical resonators realized in highly tensile stressed materials.

Mechanical energy from the resonator can be lost to the environment via the support. This loss, referred to as clamping loss, can be simulated in COMSOL by using a perfectly matched layer (PML). Any material that is defined as a PML in FEM allows the acoustic waves to propagate but dampens them to avoid the waves being reflected back into the system essentially mimicking the realistic situation of energy loss at the interface between the chip and the environment seen in Fig. 3.2(a). The accuracy of the estimation of clamping losses

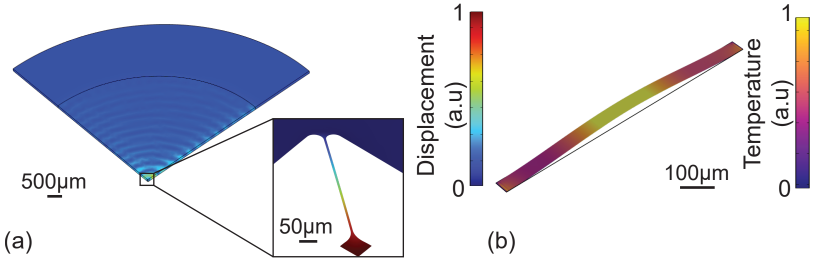

Figure 3.2: FEM simulations of mechanical properties of mechanical resonator. (a) A quarter of the geometry of a trampoline-shaped mechanical resonator patterned with PhC showing the propagation of acoustic waves of the fundamental mode of the trampoline into the PML layer (b) The heat distribution in the fundamental mode in a string resonator leading to TED.

depends on the length of the PML layer that is constructed in COMSOL. As a rule of thumb, the length of the PML defined should be able to encapsulate at least one full wavelength. As a result for kHz and MHz resonators, the PML required extents to a few mm and therefore requires considerable computing power to be simulated.

The simulations performed to estimate the TED losses required an additional physics module, i.e., 'Heat transfer in solids' and the linking of this module to the 'Solid Mechanics' module via 'Multiphysics' which takes into account thermal expansion of the material and its effect on its mechanical properties as seen in Fig. 3.2(b). The same study steps are performed as discussed above and the quality factor of the system limited by TED is obtained.

3.1.2 Simulation of optical properties

The engineering of the reflectance of the PhC was performed using a Rigorous Coupled-Wave Analysis (RCWA) based simulation software named Stanford Stratified Structure Solver (S4). RCWA is a method that is useful to model periodic structures with a refractive index contrast. The RCWA formulation begins with Maxwell's equations in the frequency domain [86]. The system under study can be inhomogeneous in the lateral directions but has to be

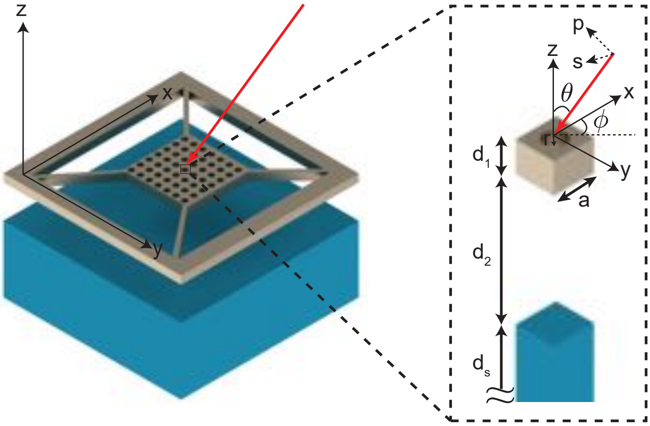

Figure 3.3: Schematic of a trampoline geometry patterned with photonic crystal. The inset shows the unit cell used for RCWA simulation. The light is incident on a material stack consisting of the device layer with photonic crystal, a vacuum gap and a substrate. A closer look at the unit cell where the photonic crystal is defined by its radius r and lattice constant a. d_1 is the thickness of the photonic crystal layer, d_2 is the thickness of the vacuum and d_s is a semi-infinite substrate. The light is incident as a plane wave with a polar angle θ and azimuthal angle ϕ.

homogeneous in the longitudinal directions. Therefore, the Maxwell's equations are transformed into Fourier space only in the lateral directions giving us a semi-analytical form of Maxwell's equations in Fourier space [101], [102]. The total system for which the reflectance has to be calculated can be subdivided into multiple layers. Each layer, as in the initial assumption - can be in-homogeneous in the lateral directions but must be homogeneous in the longitudinal direction. The modified Maxwell's equations are numerically solved to obtain the field in each layer. The propagation of the field is calculated by matching the boundary condition at each interface. In this way, the propagation of the incident light through the entire stack is calculated giving the reflectance and transmittance.

The simulation is performed on a unit cell assuming it is periodic and infinite in the lateral directions. The unit cell seen in Fig. 3.3 was constructed by providing the properties - radius, lattice constant, the material stack in the

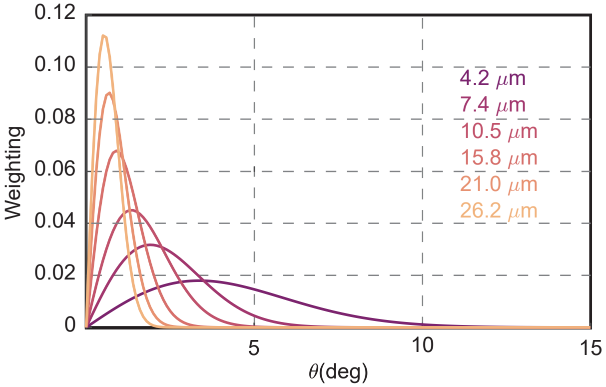

Figure 3.4: Weighting factor of a plane wave incident at polar angle θ for different waists of the Gaussian beam.

correct order and their respective refractive indices, the substrate is modeled as a semi-infinite medium. The reflectance was calculated for a plane-wave that is incident on the unit cell at the input polar (θ) and azimuthal (ϕ) angle.

The parameters of the PhC for high reflectivity are obtained by performing a simulation with varying radius and lattice constant of only the device layer. Even though the simulation is performed for a plane wave, in reality a Gaussian beam is incident on the PhC. The Gaussian beam can be decomposed into a weighted superposition of plane waves that is incident on the PhC. The weighting of plane waves is given by the denominator in Eq. 3.1. Fig. 3.4 shows the weighting of plane waves incident on the PhC at different θ for a particular waist. The optical response for plane waves incident at different incident angles θ and ϕ is calculated and weighted accordingly. The Gaussian beam response for a particular wavelength is given by Eq. 3.1 [21], [64]:

$$R(\lambda) = \frac{\int d\theta d\phi \; |\tilde{E}(\theta)|^2 \sin(\theta)\Big(\sin^2(\phi)|r_s(\lambda)|^2 + \cos^2(\phi)|r_p(\lambda)|^2\Big)}{\int d\theta d\phi \; |\tilde{E}(\theta)|^2 \sin(\theta)}, \qquad (3.1)$$

where r_s and r_p are the reflection co-efficient of the plane waves corresponding to polarization perpendicular and parallel to the plane of incidence respectively.

3.2 Fabrication

3.2.1 GaAs-based mechanical resonators

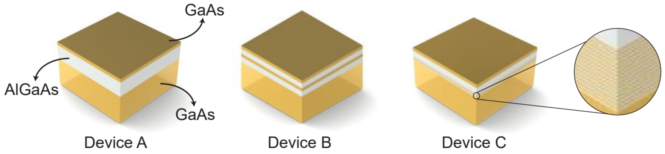

Figure 3.5: Schematic of the AlGaAs heterostructures used in fabricating the different GaAs-based mechanical resonators in this thesis.

The GaAs devices in this thesis were fabricated in AlGaAs heterostructures grown on GaAs substrates using molecular beam epitaxy. A bottom-up grow and top-down fabrication approach was adopted in fabricating the devices. The growth was done on a 2-inch wafer and subsequent fabrication was carried out on 5 mm x 5 mm or 10 mm x 10 mm chips that were diced using a diamond scriber. The first generation of our GaAs devices henceforth referred to as **'Device A'** was a single-layer device which consisted of a 4 µm thick AlGaAs sacrificial layer followed by a 100 nm-thick GaAs device layer as seen in Fig. 3.5. The second generation of the GaAs devices referred to as **'Device B'** consisted of two pairs of consecutive layers of 100 nm-thick GaAs device layers followed by a 750 nm-thick AlGaAs sacrificial layer. The third generation referred to as **'Device C'** consisted of a distributed Bragg reflector (DBR) which comprised of 30 pairs of alternating layers of 105.9 nm-thick $Al_{0.92}Ga_{0.08}As$ and 130 nm-thick GaAs grown on the wafer seen in Fig. 3.5. The DBR was followed by a set of 100 nm-thick GaAs device layer followed by a 750 nm-thick AlGaAs sacrificial layer.

The fabrication process seen in Fig. 3.6 begins with the sample preparation - cleaning the sample and resist coating followed by a lithography step. In lithography, we transfer the required pattern, i.e., mechanical resonator with photonic crystal patterning onto the resist. The lithography technique used depends upon the smallest feature size in the pattern. The available lithography techniques were contact lithography using masks, non-contact lithography using photolithography and electron beam lithography (EBL). In this work, we use photolihtography via direct laser writing and EBL for writing our patterns into the resist as these techniques are ideal for quick prototyping for devices with varying geometric parameters. For mechanical resonators with features larger than 1 µm, which were devices without any photonic crystals, the laser writer was used. For all other devices, EBL was used. The pattern is transferred on to the device layer using anisotropic etching usually done using plasma also known as 'Dry etching'. The device was released by removing the sacrificial layer which in most cases is performed by using wet chemicals in a process called 'wet etching'. An important step in our fabrication was critical point drying (CPD). The fragile nature of the mechanical devices meant that after the wet etching the devices could not be directly removed out of the liquid without them collapsing as they cannot withstand the capillary force. Hence, we use CPD as a method to dry our devices whilst preventing the collapse of the devices.

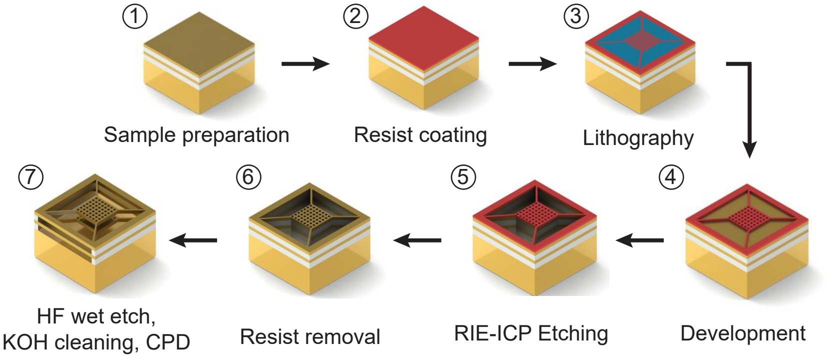

Figure 3.6: Schematics of the main process steps involved in fabrication of GaAs-based mechanical devices.

Sample preparation Cleaning of the chip after every step is of utmost importance so as to remove any residues from the previous steps that may contaminate and lead to device failure in the following steps of the fabrication process flow. Generally, sonication is used to clean the wafers but this cannot be used for brittle, crystalline materials as they are subject to getting cracked easily. Hence, the cleaning process in this thesis is always preformed by a thorough agitation of the chip in Acetone, Isopropanol and deionised water for 60 s each. In the cleaning process during sample preparation, we also use lint-free chemical wipes to remove any stubborn dust particles that are hard to remove by agitation. The sample is observed in an optical microscope after every cleaning to check for the presence of any particles on the surface.

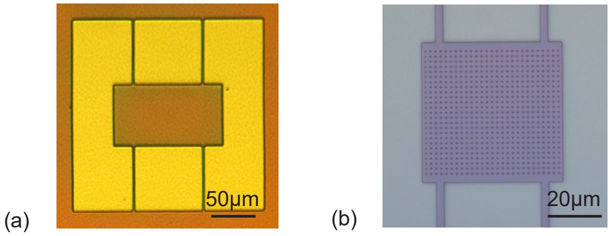

Figure 3.7: Optical microscope images of resist patterns with (a) A mechanical resonator without any PhC written using direct laser writing and (b) A mechanical resonator with PhC written using electron beam lithography

Resist coating and Lithography The sample, once cleaned, has to be coated with a resist into which the pattern is written using lithography techniques. This is done by 'spin coating' where the sample is placed in a centrifuge and the resist is poured on its surface using a pipette. For laser writing, a positive photoresist, AZ1512 was used. A 1.2 µm-thick resist layer was obtained when the photoresist is spun at 3000 RPM for 60 s following which the sample is baked on a hotplate at 100 °C for 50 s. The laser writing is performed using DWL 2000 from Heidelberg Instruments. The exposure was done using a 405 nm laser. After the lithography, the resist that was exposed is removed using a developer in a process called 'development'. The sample is agitated in the developer - MFCD-26 for 60 s followed by a dip in deionised water for 1 min. A developed device written using DWL is seen in Fig. 3.7(a).

In the devices where EBL was used seen in Fig. 3.7(b), we use chemically amplified electron beam resist, UV-60 0.75 which is also a positive resist. The resist is spun at 3000 RPM for 60 s which gives a resist layer with a thickness of 750 nm. Before exposure, the sample is pre-exposure baked on a hot-plate at 130 °C for 60 s. Since our smallest dimensions in the design - the PhC features - are in the range of a few 100 nm, EBL is performed using a Raith

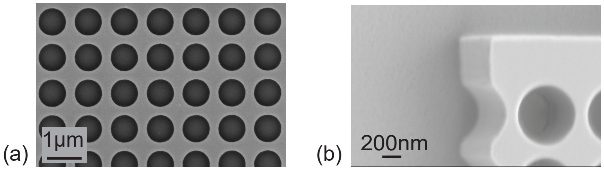

Figure 3.8: Scanning electron microscope images of devices where the pattern has been transferred to the device layer using dry etching. (a) The top view of a PhC pattern (b) An angled-view of a PhC pattern.

EBPG 5200 100 kV system. This system can write features of down to 10 nm. The chip was post-exposure baked at 130 °C for 60 s to chemically activate the polymers in the resist followed by the development using MFCD-26 for 75 s followed by a dip in deionised water for 60 s. Additionally for both the laser writing and the EBL process, a low power O2-plasma cleaning also known as ‘descum’, is performed after the development to remove any resist residues in the developed regions.

Dry etching The dry-etching is a critical part of the fabrication process flow as here we transfer the pattern from the resist onto the device layer. Since we have high-aspect ratio in the resonators, we utilize chlorine-based anisotropic reactive ion etching - inductively coupled plasma (RIE-ICP) method to etch our GaAs-based devices. The etching is carried out by mixture of $SiCl_4$ and Ar gases are introduced into the pressure-controlled chamber while the sample is placed on the bottom of the chamber on an electrode [103]. A radio frequency (RF) voltage is applied to the electrode. The RF field ionizies the gas molecules and accelerates the ions towards the bottom plate. An additional inductive coil can also be used which increases the density of the plasma. The Ar and Cl ions physically and chemically etch the material respectively while the resist acts as a mask and protects the required GaAs regions thus, transferring the pattern to the device layer as seen in Fig. 3.8.

The Cl-based chemical etching is isotropic. To make sure that the etched PhC patterns have vertical sidewalls we need to prevent lateral etching. This is achieved by the Si in $SiCl_4$ which deposits on the sidewall and prevents lateral etching [21], [103]–[107]. This becomes crucial when etching through the

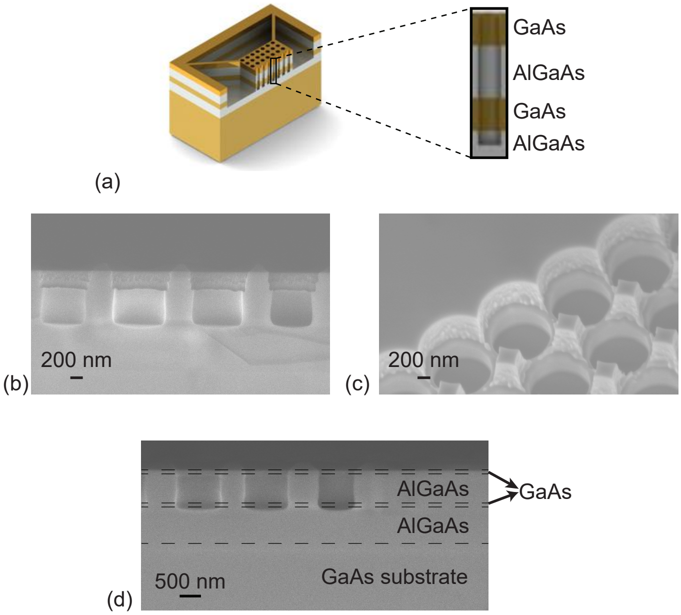

Figure 3.9: Dry etching through the layers of Device B. (a) Schematic showing the vertical sidewalls required while etching through the second GaAs layer. (b) Cross-sectional SEM image of a device showing sidewall tapering. (c) SEM image of an extreme case where the top layer of the PhC is partially etched away due to lateral etching. (d) Cross-sectional SEM image of a device with optimized etching recipe showing vertical sidewalls through the second GaAs device layer.

second layer while still maintaining the same PhC radius as seen in Fig. 3.9(a). The effect of lateral etching does not show any significant effect when etching Device A as the etch depth required for pattern transfer is only a couple of 100 nm. When the required etch depth is larger or equal to the diameter of the opening, i.e., the PhC pattern which is about 1 µm for device B we observe tapering along the sidewalls seen in Fig. 3.9(b). In extreme cases, the top layer is completely etched away as seen in Fig. 3.9(c). By optimising the etching parameters such as gas flow rates, plate and ICP power and, chamber pressure we can optimize the etch to obtain vertical sidewalls while etching through the second device layer as seen in Fig. 3.9(d).

The dry-etching exposes the underlying AlGaAs layer to the atmosphere which would lead to oxidation of AlGaAs. To prevent this, we transfer the device into deionised water immediately after the sample is removed from the etching tool. Next, we remove the resist from the chip by using a remover - REM1165 heated to 85 °C. The chip is submerged into the hot remover for 10 minutes. This is done with the chip facing downwards so as to allow any residuals from the resist to fall naturally into the beaker. We then dip the chip into isopropanol to remove any traces of the remover followed by cleaning of the device using acetone, isopropanol and deionised water. The cleaning is followed by an additional O2-plasma cleaning at 100 W for 2 min to remove any resist residues that are still on the sample surface.

Wet etching and critical point drying The devices are suspended by removing the sacrificial layer by wet etching. For the GaAs devices, 15% HF is used as the etchant which etches AlGaAs isotropically at an etch rate of $1\,\mu\mathrm{m}\,\mathrm{min}^{-1}$ [21], [108], [109] but etches GaAs at a rate of $0.1\,\mathrm{nm}\,\mathrm{min}^{-1}$ [110]. Therefore in Device A and B, the GaAs substrate acts as a natural etch-stop layer. In the DBR samples, the first layer of the DBR fulfils this role. The HF etch results in the formation of AlF_3 and $Al(OH)_3$ which are the solid etch by-products as seen in Fig. 3.10(a). Therefore, we have to perform an additional sample cleaning step to remove these etch remnants. The AlF_3 is crystalline and is soluble in deionised water whereas a dip in 4.5M KOH removes the $Al(OH)_3$ remnants [21], [109]. It was also observed that for lower HF concentrations in Device B, the HF etching would not completely remove the sacrificial layer as seen in Fig. 3.10(b). This can be a result of the small gap between the GaAs layers which hinders the etchant from efficiently etching the AlGaAs and flushing out the etch by-products. This was solved by increasing the concentration of HF and by the introduction of a stirrer during the wet etch which enabled a homogeneous flow of the etchant. The HF etch also makes the surface of the device hydrophobic as the thin oxide layer on the GaAs surface is also removed during the wet etch. Therefore after KOH cleaning, the sample is dipped in isopropanol which stays on the surface of the chip due to its higher surface tension.

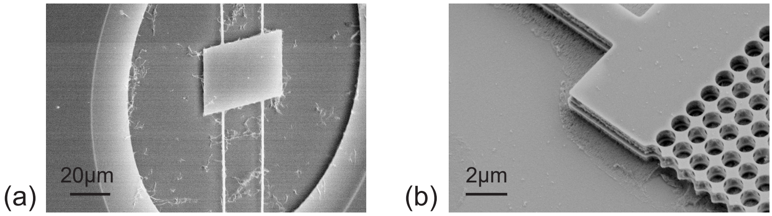

Figure 3.10: (a) SEM image of a device after HF etch without the KOH cleaning showing the $Al(OH)_3$ particles. (b) SEM image of a device showing incomplete removal of the sacrificial layer at a lower HF concentration level and absence of a stirrer during the wet etch.

Single-layer devices with sub-µm gap were also fabricated by using the Device B heterostructure. This was done by stripping the top two layers of GaAs and AlGaAs using dry and wet etching. The dry etching was performed without any resist.

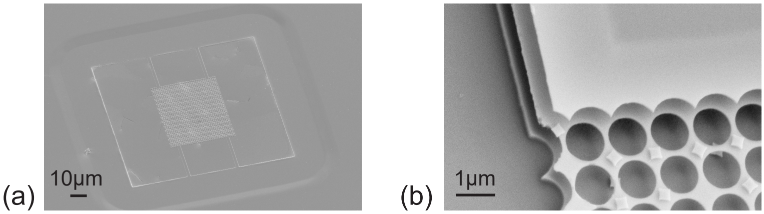

Figure 3.11: (a) SEM image of a collapsed device due to the failure of CPD. (b) SEM image of a released device where the top GaAs layer was over-etched during the dry etching step (similar to device seen in Fig. 3.9(c)) where the remnants of the top-layer are seen as diamond shaped particles.

The critical aspect to be monitored during the wet etching is that the sample is always submerged in the liquid at all times to avoid the collapse of devices due to capillary forces as seen in Fig. 3.11(a). Due to the fragile nature of the released devices, the sample can be dried only using critical point drying. In a critical point dryer, the sample is placed in the process chamber in an isopropanol bath and the alcohol is exchanged with liquid carbon dioxide (LCO_2) in a gradual manner at a high pressure. Once the chamber has only LCO_2, the chamber is heated while maintaining a high pressure to a temperature such that the LCO_2 becomes a supercritical fluid. The chamber is vented in a controlled manner to complete the fabrication process. The SEM images of fabricated devices is seen in Fig. 3.12.

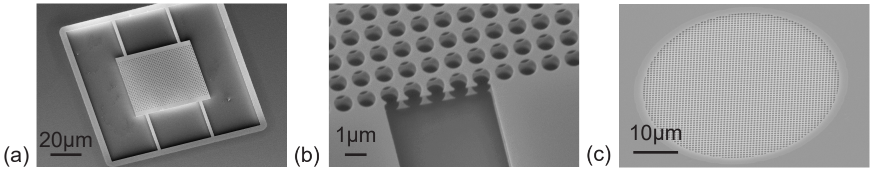

Figure 3.12: SEM images of (a) Suspended single-layer PhC - Device A (b) suspended double-layer PhC - Device B and (c) suspended PhC over a DBR - Device C.

3.2.2 InGaP-based mechanical resonators

The InGaP devices were fabricated from heterostructures grown using metal-organic chemical vapor deposition (MOCVD) on a GaAs substrate. The growth consisted of an 400 nm-thick GaAs buffer layer followed by an 75 nm-thick InGaP device layer. The fabrication process is largely similar to the GaAs-based devices with notable differences in the resist coating and wet etching step. The fabrication process shown in Fig. 3.13 begins with the sample preparation which involved cleaning and resist coating followed by a EBL which transfers the required pattern, i.e., the mechanical resonator with photonic crystals onto the resist. The pattern is transferred onto the device layer by using Cl-based dry etching. The device was released by removing the sacrificial GaAs layer with a mixture of citric acid and hydrogen peroxide followed by CPD.

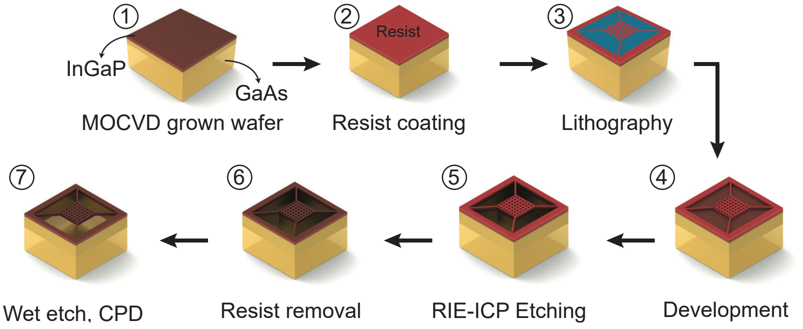

Figure 3.13: Schematics of the main process steps involved in fabrication of InGaP-based mechanical devices.

The optomechanical devices fabricated in the InGaP were long, thin string resonators and trampoline resonators, which had long, thin tethers connecting the central PhC pad to the support. These large aspect ratio features in the geometry when exposed and developed, showed a wavy behaviour as seen in Fig. 3.14(a). This behavior originates due to poor adhesion of the resist to the chip in these large aspect ratio regions. This problem is overcome with the use of the adhesion promoter TI-Prime. TI-Prime was spin-coated at 4000 RPM for 20 s and baked on a hotplate for 120 °C for 2 min. Following the adhesion promoter, the EBL resist UV-60 is spin-coated as described for GaAs-devices. The result of the pattern on a chip after development with an adhesion promoter is seen Fig. 3.14(b).

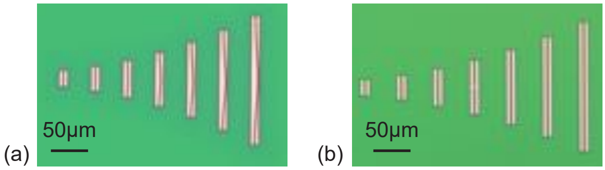

Figure 3.14: Optical microscope images of InGaP strings after exposure and development (a) without adhesion promoter and (b) with adhesion promoter TI-Prime.

The wet-etch based release of InGaP devices is different compared to the GaAs devices as the sacrificial layer is now changed to GaAs. Therefore, HF would not be a viable option to release the devices. Hence, we use a mixture of citric acid and hyrdogen peroxide in a volume ratio of 5:1 to etch the GaAs. The wet etching of GaAs using the aforementioned mixture is anisotropic with etch rates ranging from $0.2\,\mu\mathrm{m\,min}^{-1}$ to $3\,\mu\mathrm{m\,min}^{-1}$ based on the crystal direction [111]. However, before the devices are released, the adhesion promoter, TI-Prime must be removed. This is done by a dip in a 15% HF which does not etch the device layer. Following the TI-Prime removal, the sacrificial layer is removed. The sample is gently flushed with deionised water after every etching step to remove any remnants of the etchant. The process is completed with CPD to dry the sample and prevent collapse. The SEM images of fabricated devices is seen in Fig. 3.15.

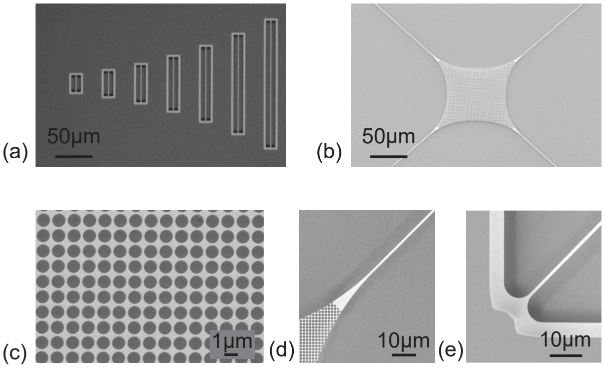

Figure 3.15: SEM images of (a) InGaP strings of varying lengths along crystal direction [1 1 0] (b) InGaP trampoline with tether width of 1 µm and tether length of 750 µm along [1 1 0], central pad area of $100 \times 100\,\mu\mathrm{m}^2$. Enlarged views of the resonator in (b) showing (c) the PhC pattern on the central area with PhC, (d) the tether connection to the central pad, and (e) the tether clamping to the substrate. Images from [33].

3.2.3 Sample analysis

The analysis of the devices before, between and after fabrication steps is crucial to verify whether the desired result has been achieved. Analysis can range from simple imaging under a optical microscope to measuring the thickness and strain in the material using X-ray diffraction. In the following section, we discuss few of the key factors that were measured/analyzed and the tools used to perform them.

Surface examination

Surface examination using optical microscopy or scanning electron microscopy (SEM) is the standard method to inspect the status of the sample after a fabrication step or the entire process. The optical microscope uses light to image the surface. The differential interference constrast (DIC) microscope, is a kind of optical microscope that allows for easy identification of surface roughness Fig. 3.16(a). SEM is a microscope that uses electrons scattered from a surface that is scanned with a focused electron beam. The sample is placed in a vacuum chamber with a translational and tilt stage that allows the imaging of several devices in different orientations. SEM images of the PhC patterns are taken to estimate the actual PhC radius r and lattice constant a to aid the estimation of the optical properties. The SEM can also be used to perform energy-dispersive X-ray (EDX) analysis where the chemical composition of the material that is being imaged can be estimated. This is a useful tool to identify the origin of any unexpected particles that appear on the sample after a process as seen in Fig. 3.16(c). When an electron from the inner shell of an atom is removed by the incoming electron energy and an electron in an outer shell takes its place, the result is the emission of a particular x-ray energy. Each element has a characteristic x-ray which is collected by the EDX detector. The energy of the detected X-rays is used to decipher the elements present in the field-of-view.

Layer thickness estimation

The thickness of the device layer plays a crucial role in device design and characterization. In this thesis, a combination of four different techniques were used in thickness estimation. SEM imaging can be used to obtain a rough estimate of the thickness. A cross-section of the wafer is cleaved and imaged as seen in Fig. 3.17(a). A more accurate measurement technique that provides

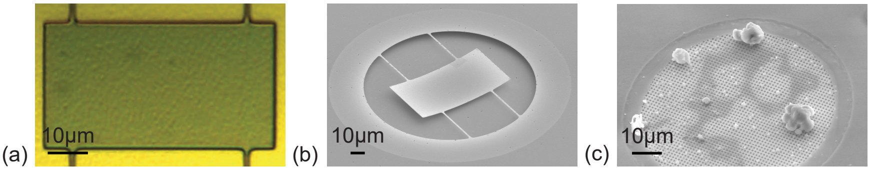

Figure 3.16: (a) A DIC microscope image of a device layer showing surface roughness. (b) The SEM image of a released device showing buckling (c) The SEM image with unexpected particles after wet-etch and CPD identified as potassium salts using EDX.

accuracy in the sub-nm range is transmission electron microscopy (TEM). TEM is a microscopy technique where electrons are transmitted through a material to form an image. The sample to be imaged is prepared in the form of a lamella - a thin slice, using focused ion beam milling. The image is formed as the electrons passing through the material interact with the electrons in the material. In this thesis, TEM imaging is performed on a cross-section of the heterostructure growth to estimate the actual thickness of the device and sacrificial layers. Additionally, the quality of growth can be estimated looking at the roughness of the grown layers. An example of a false colored TEM image is shown in Fig. 3.17(b).

Ellipsometry is a technique that is used to investigate the dielectric properties of a material. If the refractive index of the material under test is well-known, this method can also be used to estimate the thickness. X-ray diffraction (XRD) analysis is a measurement technique that is used to determine the crystallographic structure of a material. This method can also be used to measure the thickness of the material along with other properties such as material concentration, strain in the layers, etc.

Surface roughness

Surface roughness determines the quality of the mechanical resonators that we can fabricate as it contributes to surface losses. Also, the optical properties of the PhC is drastically affected by surface roughness. Hence, it is important to quantify the surface roughness of the layer. The DIC microscopy discussed

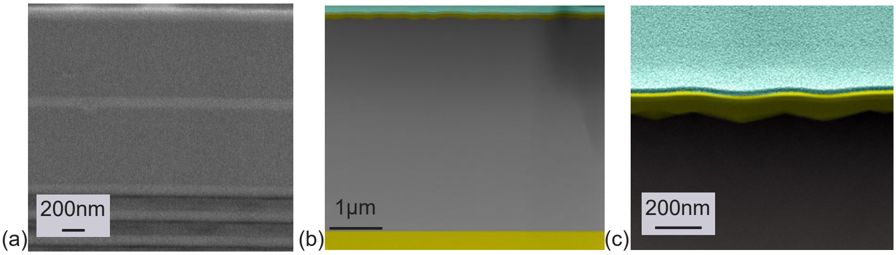

Figure 3.17: (a) A cross-sectional SEM image showing the device layers and first alternating DBR layers. (b) False-colored TEM image of Device A. The top layer (green) is palladium that is deposited during ion beam milling, followed by the GaAs layer (yellow) and the AlGaAs layer (gray) on top of the GaAs substrate (yellow) (c) A closer look at the TEM image of the device layer in (b). TEM images taken from Ref. [21].

earlier can provide a qualitative measure of the roughness. However, atomic force microscopy (AFM) must be used for quantitative measurement of surface roughness. AFM is a technique in which a cantilever with a sharp tip is scanned over the surface of a sample. The sharp tip interacts with the surface via Van der Waals forces. We use the non-contact mode where the cantilever with the sharp tip hovers a few nm above the sample surface and can be used to image the surface topology. The AFM signal yields surface properties such as roughness, waviness etc. AFM measurement can be used to measure buckling (Fig. 3.16(b)) or static deformation in released devices. Fig. 3.18(a) shows an AFM scan of a suspended PhC membrane. Fig. 3.18(b) shows the profile of the region marked with a blue line in Fig. 3.18(a) that is normalized to the unreleased region. The released region shows buckling in the range of 20 nm.

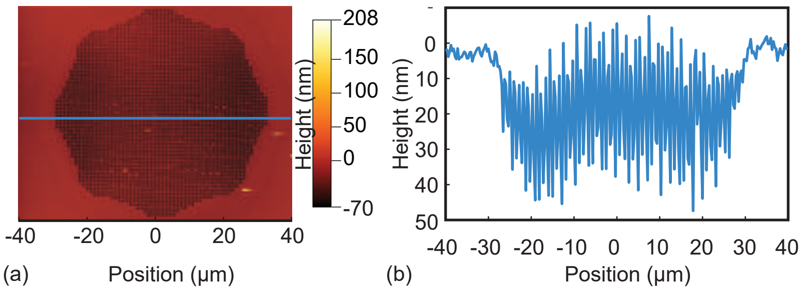

Figure 3.18: (a) AFM image showing a topographical scan of a released and suspended PhC membrane. (b) Normalized surface profile of the membrane along the direction marked blue in (a)

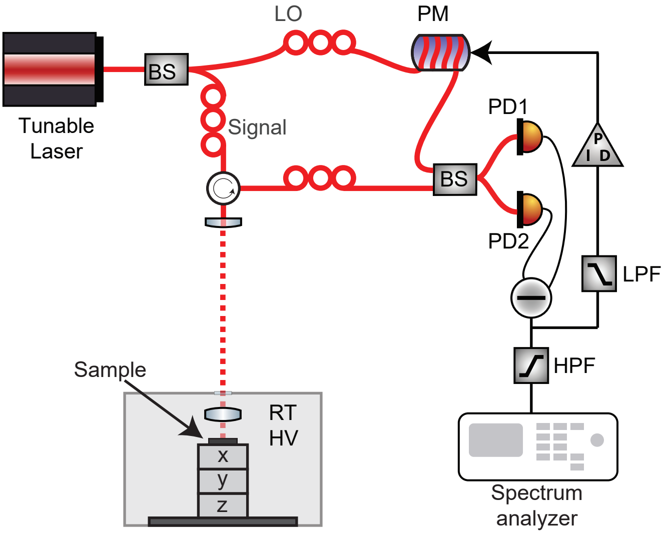

Figure 3.19: Experimental setup for characterization of mechanical properties of the mechanical resonators. The solid lines and dashed lines indicate the fiber beam path and the free-space beam path respectively. BS: fiber-based beam splitter, PM: fiber-based phase modulator, PD: photodetector, RT: Room temperature, HV: High Vacuum, PID: Proportional-Integral-Derivative controller, LPF: Low-pass filter, HPF: High-pass filter.

3.3 Setup and Measurement

3.3.1 Characterization of mechanical properties

The characterization of the mechanical properties of the fabricated devices is performed using an optical homodyne detection setup using a tunable telecom-wavelength laser seen in Fig. 3.19. The mechanical modes of suspended devices relate to a time-dependent displacement Δx. When a signal beam with a steady state amplitude $\alpha_s(t)$ interacts with the resonator its mechanical displacement modulates the phase quadrature of the signal. The modulations can be written as amplitude $\delta X_s(t)$ and phase $\delta Y_s(t)$ fluctuations around the steady state. This information is encoded into the phase of its reflected field $\phi = k\Delta x$, where k is the wave vector of the incident light. The phase of the light reflected off the mechanical resonator is measured using an interferometer where a reference beam referred to as the local oscillator (LO) is generated from the same laser source, hence the name 'homodyne detection'. The reflected signal can be written as [74], [112]:

$$\alpha_s(t) = \alpha_s + \delta X_s(t) + i\delta Y_s(t) \tag{3.2}$$

where $\alpha_s, \delta X_s(t), \delta Y_s(t) \in \mathbb{R}$. This signal is mixed with a strong LO on a 50/50 beam splitter and detected by two photodetectors. The LO signal can be written as

$$\alpha_{LO}(t) = [\alpha_{LO} + \delta X_{LO}(t) + i\delta Y_{LO}(t)]e^{i\varphi} \tag{3.3}$$

The field on the two photodetectors PD1 and PD2 can be written as:

$$\alpha_{PD1} = \sqrt{\frac{1}{2}}\alpha_{LO}(t) + \sqrt{\frac{1}{2}}\alpha_s(t), \tag{3.4}$$

$$\alpha_{PD2} = \sqrt{\frac{1}{2}}\alpha_{LO}(t) - \sqrt{\frac{1}{2}}\alpha_s(t) \tag{3.5}$$

Assuming that the intensity in the LO is much larger than the signal and following the derivation available in Ref. [112], we obtain the difference in photo-current between the two photodiodes as:

$$i(t) = i_{D1} - i_{D2} = 2\alpha_{LO}\alpha_s(\cos\varphi) + 2\alpha_{LO}[\delta X_s(t)(\cos\varphi) + \delta Y_s(t)(\sin\varphi)] \quad (3.6)$$

The homodyne signal has a DC term that is proportional to the steady-state amplitudes and AC terms that depend on the relative phase between signal and LO. This means by changing φ, we can either measure only the amplitude or phase quadrature or a combination of both. Since we are interested in the phase quadrature to measure the mechanical modes, we use a PID controller to generate an error signal using the low frequency component of the signal to lock the signal on the maximum slope, i.e., $\varphi = \pi/2$. In this way, we use a homodyne detection scheme to measure the mechanical properties such as eigenfrequencies and quality factor.

3.3.2 Characterization of optical properties

The setup for measuring the optical reflectance of the PhC slabs is shown in Fig. 3.20. A laser beam passes through a polarizer defining the polarization of the incident light. A half-wave plate is used to adjust the ratio of the light reflected and transmitted at a polarizing beam splitter (PBS). The reflected light is sent to a photodetector and called the reference arm. A quarter-wave plate rotates the light transmitted from the PBS to circular polarization. We use a lens to focus the light onto the PhC slab. The light reflected off the sample collects a π-phase shift upon reflection and, after passing through the quarter-wave plate, is vertically polarized and, thus, reflected by the PBS into the detection arm. The InGaAs charge-coupled device camera is used to image the transverse optical modes of the reflected beam. This type of reflectance measurement scheme assumes that the reflectance of the sample is the same for s- and p-polarized light. As the PhC pattern on the mechanical resonators used in this work have C_4 symmetry, the above condition is valid.

The reflectance of the PhC slab, R_{PhC}, is then given by:

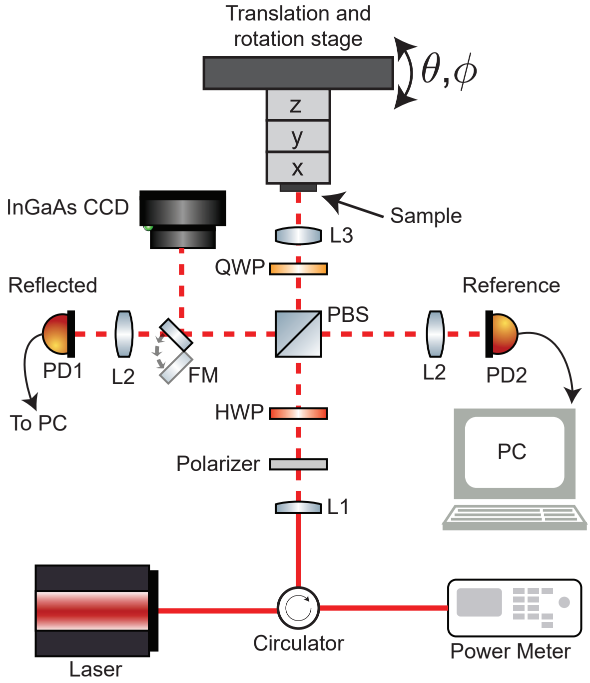

Figure 3.20: Experimental setup for the characterization of the optical reflectance of devices. The solid lines and dashed lines indicate the fiber beam path and the free-space beam path respectively. HWP: half-wave plate, QWP: quarter-wave plate, PBS: polarizing beam splitter, FM: flip mirror, PD: photodetector. L1: triplet collimator , L2 and L3: focusing lens.

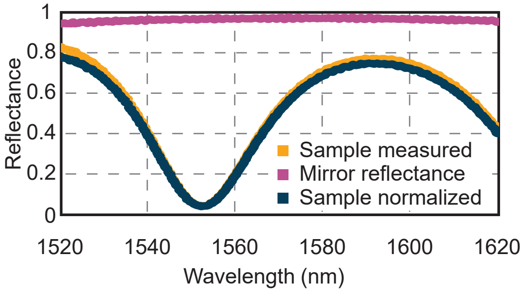

Figure 3.21: Reflectance spectra of a mirror of known reflectance and a PhC fabricated in an 75 nm-thick InGaP suspended above a GaAs substrate with a 14.8 µm gap.

$$R_{\mathrm{PhC}} = \left(\frac{I_{\mathrm{PD1}}^{\mathrm{Sample}}}{I_{\mathrm{PD2}}^{\mathrm{Sample}}}\right) \cdot \left[\left(\frac{I_{\mathrm{PD1}}^{\mathrm{Mirror}}}{I_{\mathrm{PD2}}^{\mathrm{Mirror}}}\right)^{-1} \cdot R_{\mathrm{mirror}}\right] \tag{3.7}$$

where $I_{\mathrm{PD1}}^{\mathrm{Sample}}$ $(I_{\mathrm{PD1}}^{\mathrm{mirror}})$ is the reflected signal intensity of the device under test (a mirror of known reflectivity) measured by photodetector 1 (PD1) and $I_{\mathrm{PD2}}^{\mathrm{Sample}}$ $(I_{\mathrm{PD2}}^{\mathrm{Mirror}})$ is the reference signal intensity measured simultaneously by photodetector 2 (PD2). This means that we normalize the signal in PD1 by the one in PD2 to account for laser intensity fluctuations. In order to account for any undesired wavelength dependence of the utilized optical components, we independently measure the reflectivity of a mirror of known reflectance, R_{mirror}, in our setup, i.e., $I_{\mathrm{PD1}}^{\mathrm{Mirror}}/I_{\mathrm{PD2}}^{\mathrm{Mirror}}$ and normalize by this measurement, as seen in Fig. 3.21.

3.3.3 Characterization of optomechanical properties

The optomechanical properties are characterized by combining the measurement setups used to characterize the mechanical and optical properties. The $\lambda/2$, PBS, $\lambda/4$ and photodectectors are introduced in the free-space path after the collimator in the mechanical setup marked with a dashed box in Fig. 3.22. An important requirement when measuring optomechanical effects is to have

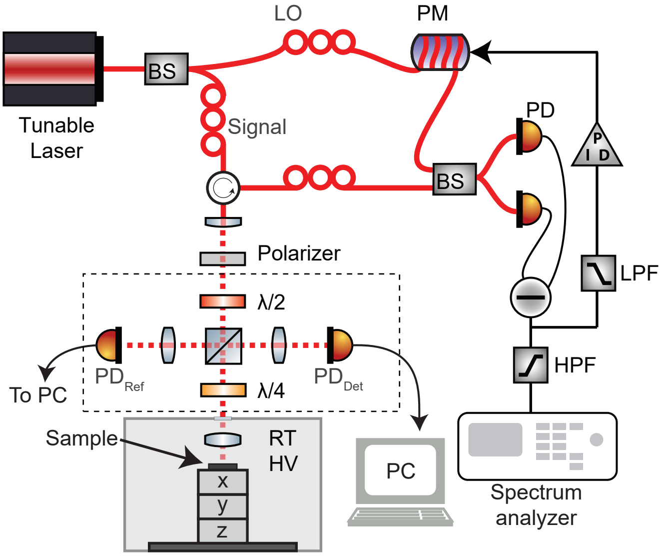

Figure 3.22: Experimental setup used for characterizing the optomechanical properties of the devices. Solid lines represent the fiber beam path and dashed lines the free-space beam path, BS: beam splitter, PM: fiber-based phase modulator, $\mathrm{PD}_{\mathrm{Ref(Det)}}$: photo diode in the reference (detection) arm, RT: room temperature, HV: high vacuum, PID : Proportional-Integral-Derivative controller, LPF : Low-pass filter, HPF : High-pass filter

the same power incident on the sample when tuning the wavelength. The photosensitivity of the photodiode (Hamamatsu InGaAs PIN photodiode - G12180-005A) is almost constant in the wavelength regime of interest. In the optomechanical setup, the reference photo diode $\mathrm{PD}_{\mathrm{Ref}}$ whose voltage readout is used to maintain a constant power reaching the sample when tuning the laser wavelength.

CHAPTER 4

Results

In the following chapter, we present and discuss the optomechanical properties of highly-reflective optomechanical resonators in III-V heterostructures. We begin by demonstrating the feasibility of the III-V material system for realizing integrated free-space cavity optomechanics. To this end, we show a proof-of-concept by fabricating single-layer GaAs PhC resonators and examining their optical and mechanical properties. To show the capabilities of AlGaAs-based heterostructures, we then explore two device architectures interesting in the context of cavity optomechanics - two suspended GaAs-based PhC mirrors and a suspended PhC mirror on a distributed Bragg reflector (DBR). Both systems have the two mirrors separated by a sub-µm gap between them, thus forming an optical microcavity. We investigate the optical properties of the systems. The frequency-dependent reflectance of the PhC opens the possibility to engineer interesting optical cavity properties such as 'bound state in a continuum' (BIC). We discuss the optomechanical effects such as optomechanically induced frequency shift observed due to the microcavity interacting with the suspended PhC mirror. The absence of significant tensile stress in GaAs, however, limits the GaAs-based mechanical quality factor of the mechanical resonators to be maximally around 10^5. Hence, we consider InGaP - a III-V material which can be grown with stress up to 1 GPa while being compatible with AlGaAs-based heterostructures. We extract the material properties of InGaP using one-dimensional string resonators. Following this, we fabricate trampoline resonators including a PhC. The trampolines exhibit mechanical quality factors $\geq 10^7$, the highest reported to date in an InGaP-based micromechanical resonator.

4.1 GaAs-based optomechanical systems

Multi-element optomechanics has been theoretically shown to be able to increase the optomechanical coupling [54], [113]. This increase in optomechanical coupling would allow to access new and interesting non-linear regimes in optomechanics. The uniformity of the mechanical resonators and the gap between them, along with their individual reflectivity, plays a crucial role in determining the coupling enhancement. III-V materials with the advantage of bottom-up heterostructure growth and top-down fabrication are the ideal candidate for realizing such a multi-element system. III-V materials also offer the possibility of integrating one of the cavity ‘mirrors’ in the form of a DBR.

4.1.1 Single-layer GaAs system

The objective of the single-layer GaAs devices - Device A is to establish a proof-of-concept that III-V materials specifically GaAs can be used to fabricate high-quality, high-reflectance mechanical resonators. The mechanical resonators realized in GaAs have shown mechanical quality factors of up to 10^5 at room temperature [18]–[20], [22]–[29]. These resonators can be used as building blocks to realize a mechanical resonator array in a multi-element optomechanical device. Device A consisted of a 100 nm-thick GaAs device suspended above the substrate. The sacrificial layer was a 4 µm-thick $Al_{0.65}Ga_{0.35}As$. In

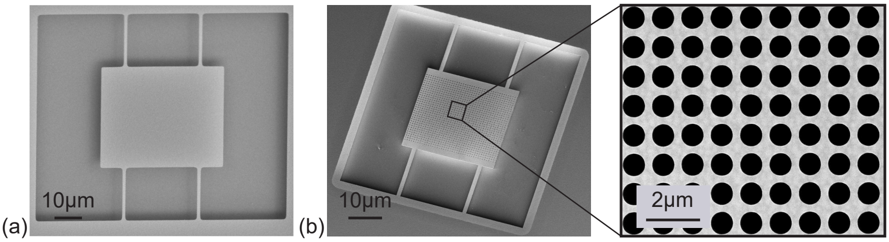

Figure 4.1: (a) SEM image of a single-layer GaAs device without PhC after fabrication (b) SEM image of a single-layer GaAs device with PhC after fabrication along with a closer look at the PhC on the device layer.

Device A, we utilize the 'free-free'-type geometry where a rectangular slab is connected to the support with four tethers [24], [25]. The advantage of the free-free geometry is evident when the tethers are connected at the flexural node of the 'free-free' mode. In this case, the mechanical mode is well-isolated from the surroundings and the energy loss via phonons is drastically minimized [24], [25]. The rectangular slab is patterned with a PhC to increase the out-of-plane reflectivity [63]. This is important as the intrinsic reflectance of a 100 nm-thick GaAs layer is only 67%. We fabricated Device A without - Fig. 4.1(a) and with PhC Fig. 4.1(b) using the process discussed in Sec. 3.2.1. The mechanical and optical response of the single-layer GaAs PhC resonators is presented below.

Reflectance engineering

The first step in engineering the optical properties of the system is to design an appropriate PhC pattern by determining the parameters of the PhC [8], [59], [63], [114], [115]. We choose a C_4 symmetry for the PhC to make its out-of-plane reflectance polarization insensitive. The PhC parameters, i.e., radius r, and lattice constant a, are chosen by simulating a reflectance map for a particular wavelength using S4 [116]. We consider a 100 nm-thick GaAs slab for an incident wavelength of $\lambda = 1550\,\text{nm}$ with a plane wave incident at polar angle $\phi = 0$ and azimuthal angle $\theta = 0$, as seen in Fig. 4.2(a). The reflectance map of the unit cell for varying r and a is shown in Fig. 4.2(b). In the EBL exposure step, the placement of the holes at the required position

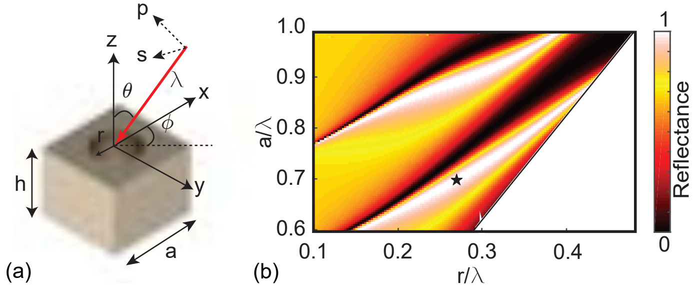

Figure 4.2: (a) Schematic of a unit cell of a PhC with thickness h, radius r and lattice constant a. A plane wave with wavelength λ is incident at a polar angle θ and azimuthal angle ϕ. (b) Reflectance map for an incident wavelength $\lambda = 1550\,\mathrm{nm}$ plane wave at normal incidence on a $h = 100\,\mathrm{nm}$ GaAs PhC slab for varying r and a. The star indicates the parameters for $R > 99.99\%$, i.e., $r = 418\,\mathrm{nm}$ and $a = 1081\,\mathrm{nm}$.

on the PhC slab, i.e., the lattice constant, is more precise than the radius of an individual hole. We want to choose a PhC pattern whose reflectance has a high tolerance to fabrication related imperfections. Therefore, we look for a region of the reflectance map which has a high constant reflectivity when slightly varying r but for a fixed a. The parameters chosen, i.e., $r = 418\,\mathrm{nm}$ and $a = 1081\,\mathrm{nm}$, are marked by a star in Fig. 4.2.

The reflectance of the fabricated PhC slabs in Device A are measured using the setup described in Sec. 3.3.2 and their reflectance is plotted in Fig. 4.3(a). We observe the maximum of the reflectance around 1510 nm instead of the expected 1550 nm based on the PhC design. The TEM cross-sectional imaging seen in Fig. 4.3(b) shows that the GaAs device layer has large surface height variation due to the sample being grown without growth interruption [21], [117]. This is undesirable as the height variation also results in surface roughness resulting in optical losses. The average thickness was calculated to be 87.5 nm. By taking into account this average thickness, we can reproduce the high reflectivity of the PhC at 1510 nm. The samples grown for future devices discussed in this thesis were grown with growth interruption, which reduced the height variation and surface roughness considerably.

The feature that stands out in the reflectance measurement is the dip at

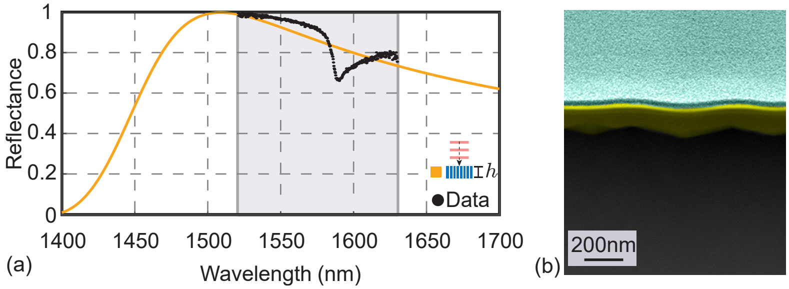

Figure 4.3: (a) Reflectance spectrum of a suspended GaAs PhC membrane of thickness $h = 87.5\,\text{nm}$ and air-gap $l = 4.3\,\mu\text{m}$. The simulated spectrum (orange) for a plane wave incident on the PhC slab. (b) False-colored TEM image of the heterostructure used to fabricate Device A. The top layer (green) is palladium deposited during sample preparation, followed by the GaAs (yellow) and the AlGaAs (gray) layers.

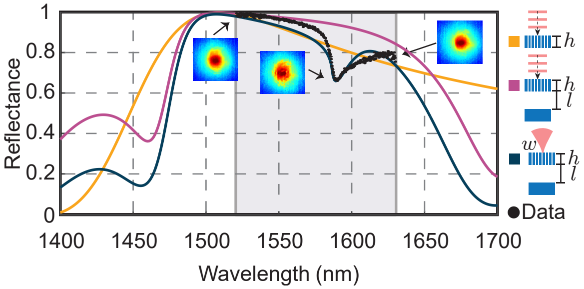

Figure 4.4: Reflectance spectra of a suspended GaAs PhC membrane of thickness $h = 87.5\,\text{nm}$ and air-gap $l = 4.3\,\mu\text{m}$. The data (black) is compared to simulated spectra for a plane wave incident on the PhC slab (orange) or on the slab on top of a GaAs substrate (purple) and a Gaussian beam pf of waist $4.2\,\mu\text{m}$ incident of the PhC (blue) . The gray region marks the measurement range. The insets show transverse mode patterns measured in reflection. Image taken from [21].

1581 nm. To understand the origin of this dip, we first simulate the reflectance of the stack containing the PhC, the GaAs substrate and the vacuum gap between the two. In Fig. 4.4, we plot the reflectance of this stack, in purple, for a plane wave incidence. We see that the dip is not captured by this simulation. Next, we also take into account that the light beam incident on the stack is not a plane wave but a Gaussian beam. The construction of the optical response of the stack to a Gaussian beam is performed by a weighted sum of plane waves as discussed in Sec. 3.1.2. We see that when considering the Gaussian beam, in blue, we get a good agreement with the measured reflectance.

As discussed in Sec. 2.4.1, the light beam incident on the PhC slab can couple to the guided resonance of the PhC. This will modify the reflectance of the PhC [59]. In addition to the guided resonance that helps in reflectance engineering, there exists 'parasitic guided resonances' in a PhC. These guided resonances couple to light incident at oblique angles and modify the reflectance further. In Fig. 4.5(a), we look at the reflectance map of the wave vector β and frequency ω where $\beta = \frac{2\pi}{\lambda}\sin(\theta)$. We observe that the dispersion relation of the parasitic guided resonance at 1581 nm at $\beta = 0$ decreases with increasing β. This means that the guided resonance appears at larger wavelength for plane waves incident on the PhC for increasing polar angles. Hence, the plane waves incident at oblique angles couple into this parasitic guided resonance and reduces the overall reflectance of the system.

In Fig. 4.5(b), we examine the effect of varying the waist of the incident Gaussian beam on the reflectance. We see that the dip becomes narrower for larger waists. This is because for larger waists the weighting of plane waves at oblique angles reduces as seen in Fig. 3.4. Therefore, less of the external beam couples into the parasitic guided resonance [21]. This is seen as a narrowing of the parasitic guided resonance in the reflectance spectra. Note also that the overall reflectance of the device reduces for increasing waist. This is due to clipping losses that arise from the finite size of the PhC slab.

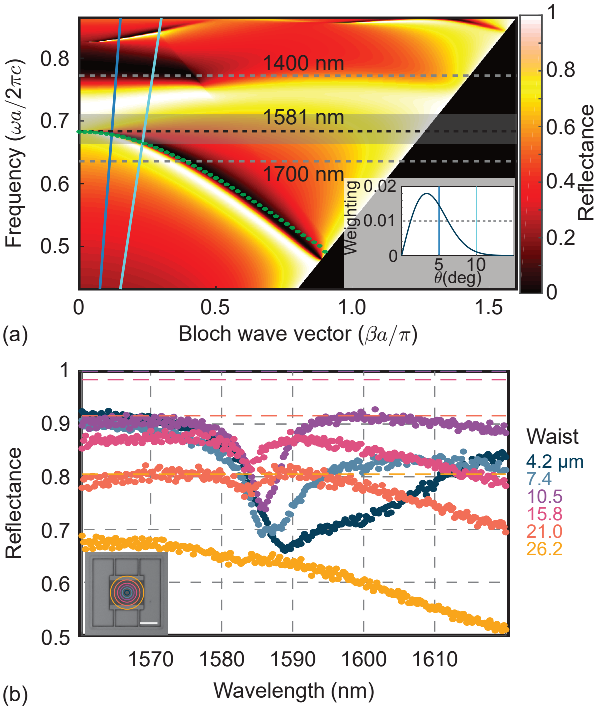

Figure 4.5: (a) Reflectance map of a PhC membrane for an incident plane wave of wave vector $\beta = \frac{2\pi}{\lambda}\sin(\theta)$ and frequency ω. The green dots show the dispersion of the guided resonance for an s-polarized wave. The inset shows the weighting factor for plane waves corresponding to a Gaussian beam of waist 4.2 µm. The blue lines mark the same angles of incidence in the inset and main panel. (b) The measured reflectance of Device A around the dip with varying waist size of the incident beam. The corresponding dashed horizontal lines indicate the expected clipping loss due to the finite size of the PhC. Image taken from Ref. [21].

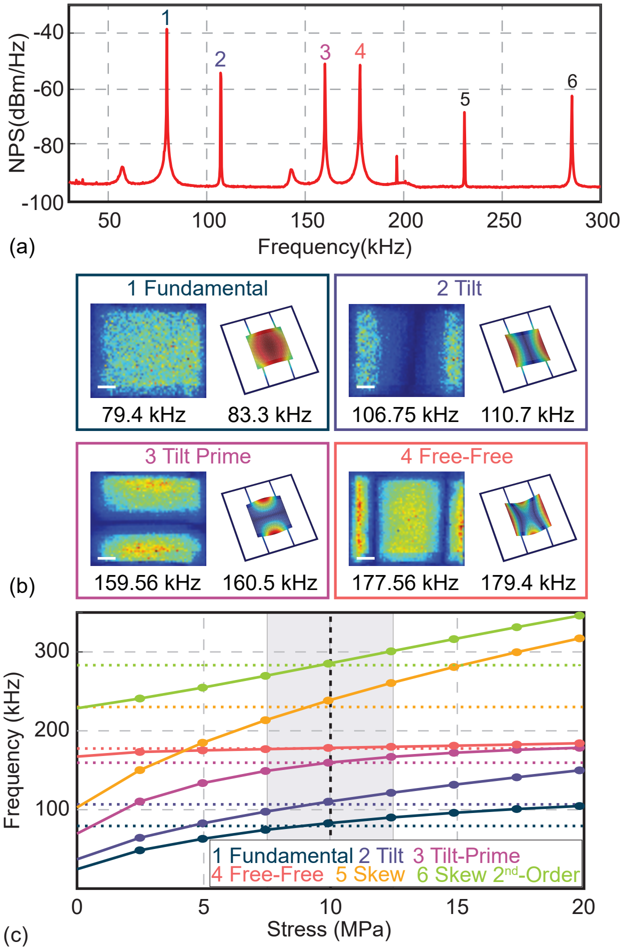

Figure 4.6: (a) Noise power spectrum (NPS) of a 50 µm × 50 µm PhC slab of free-free geometry with its mechanical modes labeled 1–6. (b) Mechanical-mode tomography of the same device along with FEM-simulated mode shapes and their frequencies. Scale bar: 10 µm (c) FEM simulation results for the device in (a) for varying tensile stress (lines are guides to the eye). The dotted horizontal lines show the measured frequencies from (a). Image taken from [21].

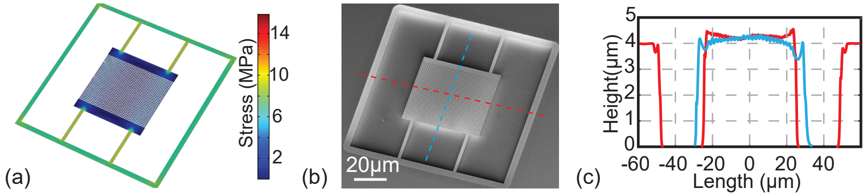

Figure 4.7: (a) FEM simulation of Von Mises stress of a released device. (b) An SEM image of a released device with PhC. (c) Measured height profile of the device in (b) along the line marked. Image taken from [21].

High-quality mechanical resonators

The mechanical properties of the devices were measured using the setup discussed in Sec. 3.3.1. The noise power spectrum (NPS) of a suspended 50 μm × 50 μm PhC slab is seen in Fig. 4.6(a). Mode tomography is performed on each mode to obtain the experimental mode-shape. We can see that the measured mode-shape and eigenfrequencies are in good agreement with the FEM simulations provided that we consider a tensile stress of 10 MPa in the device layer. We attribute the tensile stress to the lattice mismatch between the AlGaAs sacrificial- and GaAs device-layer. The tensile stress that is expected in the GaAs device layer due to a relaxed $Al_{0.65}Ga_{0.35}As$ layer is 77.5 MPa. As discussed in Paper A, the 4 μm AlGaAs layer can be in a state between being fully relaxed and fully strained depending on the model used to calculate the critical thickness [21]. Therefore, we expect a tensile stress between 0 and 77.5 MPa in the GaAs device layer. The FEM simulations of the eigenfrequencies of the free-free geometry for varying initial tensile stress is seen in Fig. 4.6(c). We observe that the simulated and measured eigenfrequencies are in very good agreement at a tensile stress of 10 MPa.

The stress in the device is redistributed in the released device. This stress redistribution can be calculated with FEM simulations as seen in Fig. 4.7. We see that after release the stress concentrates in the tethers while the device layer will relax. This relaxation leads to buckling seen in Fig. 4.7(c). The buckling of the device is undesired as it leads to additional mechanical energy dissipation and therefore reduces the mechanical quality factor of the resonator [100] and also leads to optical losses due to scattering.

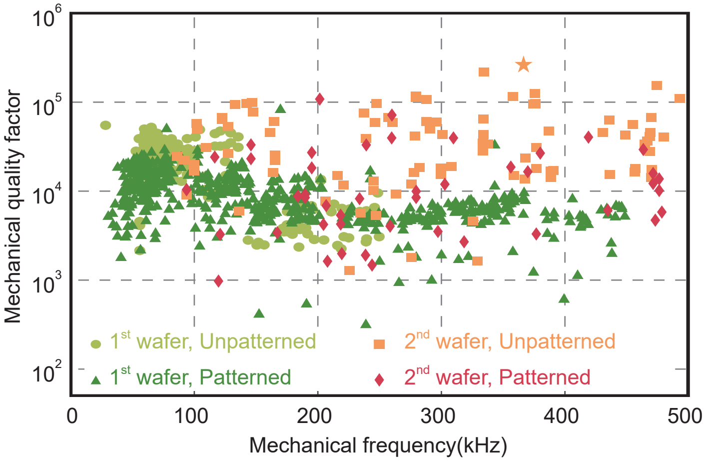

Figure 4.8: Mechanical quality factors of different modes for unpatterned and patterned GaAs devices measured at room temperature in high vacuum. 1^{st} (2^{nd}) wafer refers to the heterostructure grown without (with) growth interruption. The highest $Q \cdot f$ product is $9.8 \cdot 10^{10}$ Hz (star). Image taken from [21]

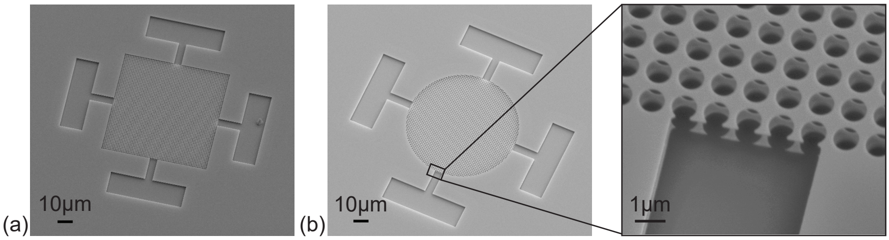

Figure 4.9: SEM images of double-layer devices fabricated from the heterostructure of Device B.

In Fig. 4.8, we present the measured mechanical quality factor for different samples of Device A. We obtain a maximum quality factor of $3 \cdot 10^5$. This is a reasonable value of mechanical quality factor due to the low tensile stress in our devices and comparable to other works in GaAs [18]–[20], [22]–[29]. We see that PhC patterning on the mechanical resonator does not affect the quality factor. The mechanical quality can be limited by surface losses due to the surface roughness, mechanical dissipation due to buckling in the PhC slab. In Fig. 4.8, we also see that the mechanical devices fabricated in the wafer grown with growth interruption (2^{nd} wafer) showed better Q-factors compared to wafer without growth interruption (1^{st} wafer). Thus we can observe the increase in Q-factor due to a reduction in surface roughness. In Fig. 4.8, we measure the Q-factor of different mechanical modes and we see that the Q-factor does not show any considerable variation. Hence, we can conclude that the free-free mode does not offer any observable advantage in improving the mechanical quality factor.

In Device A we see that we can realize out-of-plane reflectance $> 99\% \pm 2\%$ in GaAs-based mechanical resonators using PhCs. The parasitic guided resonance that reduces the reflectance can be avoided by using larger waists or different PhC pattern parameters. The size of the PhC must be large enough to not be limited by clipping losses. The mechanical quality factor of the single layer devices is $\simeq 10^5$.

4.1.2 Double-layer GaAs system

In the previous section we showed that III-V materials can be utilized to realize single-layer devices as part of an optomechanical system. Now, we look to demonstrate the other advantage of III-V materials - the ability to fabricate a monolithic resonator array. The resonator array was fabricated in an AlGaAs heterostructure with two pairs of 103 nm-thick GaAs device layer and a 730 nm-thick $Al_{0.62}Ga_{0.38}As$ sacrificial layer grown on a GaAs substrate. As discussed in Sec. 4.1.1, the free-free device does not offer an advantage in increasing the mechanical quality factor but rather causes buckling. So, we use a fully clamped membrane as the preferred geometry for samples in Device B. We fabricate both square and circular shaped membranes with PhC as seen in Fig. 4.9. Openings were made in the support of the membrane to efficiently flush the etch by-products during the wet-etch fabrication process.

PhC-PhC Microcavity

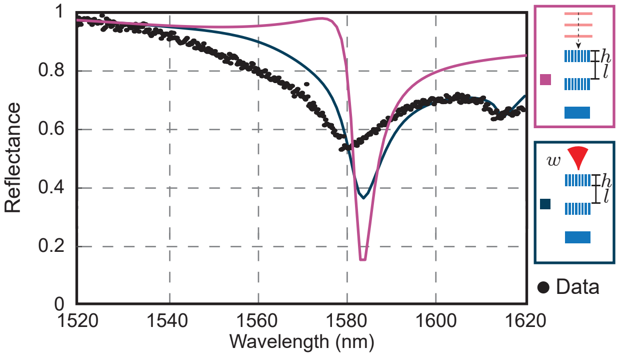

Figure 4.10: (a) Reflectance spectrum of a double-layer device with $r = 435\,\text{nm}$ and $a = 1081\,\text{nm}$ for a GaAs device layer thickness of $h = 103\,\text{nm}$ and gap between devices $l = 730\,\text{nm}$. The data (black) is compared to the simulated spectra for a plane wave (purple) and a Gaussian beam of waist 4.2 µm (blue) incident on the double-layer stack [65], [66].

The measured and simulated reflectance spectra of Device B is shown in Fig. 4.10. The measured reflectance spectrum exhibits two clear reflectance dips at 1580 nm and another at 1618 nm. We can observe that the dip at 1580 nm is present in the simulation for a plane wave incident on the device. This would point to the dip not being a parasitic guided resonance. The two PhCs form a cavity to which the incident light couples. The cavity line-width is large with a cavity finesse (Eq. 2.27) of about 8, hence we form a 'bad cavity'. The second dip at 1618 nm is captured in the simulations when taking into the account the Gaussian beam that is incident on the device. This dip is attributed to a parasitic guided resonance in the top PhC as discussed in Sec. 4.1.1.

BIC in PhC-PhC microcavity

The frequency dependent reflectance of PhC gives rise to some interesting phenomena when two PhCs form an optical cavity as in our case. The interference between the guided resonances of the PhC and the cavity resonance give rise to modification in the optical response of the system via cavity linewidth modulation. In Fig. 4.11(a), we see the simulated transmission spectrum of unpatterned slabs while varying the distance between them. We can observe that the Fabry-Pérot cavity resonances denoted by dashed lines are formed when the length fulfills the resonance condition $\nu = c/2q$. The cavity eigenmodes seen as blue crosses (circles) signifying their even (odd) symmetry in the out-of-plane direction. In Fig. 4.11(b), we observe the simulated transmission map of two identical PhCs with PhC parameters $r = 236$ nm and $a = 930$ nm. At the first glance, the transmission spectrum is different due to the patterning. We see that close to the designed resonance of the PhC denoted by the green dashed line the cavity linewdith narrows.

A closer look at the transmission map around the region where the linewidth narrows is shown in Fig. 4.12(a). It shows that for a certain gap the linewidth becomes zero. This is also seen in the quality factor of the cavity eigenmodes as it reaches infinity at this gap see in Fig. 4.12(b). This cavity mode can also be called a 'bound state in a continuum' (BIC). Engineering a BIC in a system with two PhCs would essentially uncouple the optical loss rates from the cavity length. This would mean a system whose optomechanical coupling g_0 is greater than the optical loss rate κ can be realized with only two patterned PhC slabs without the need of an external optical cavity. Such a system with

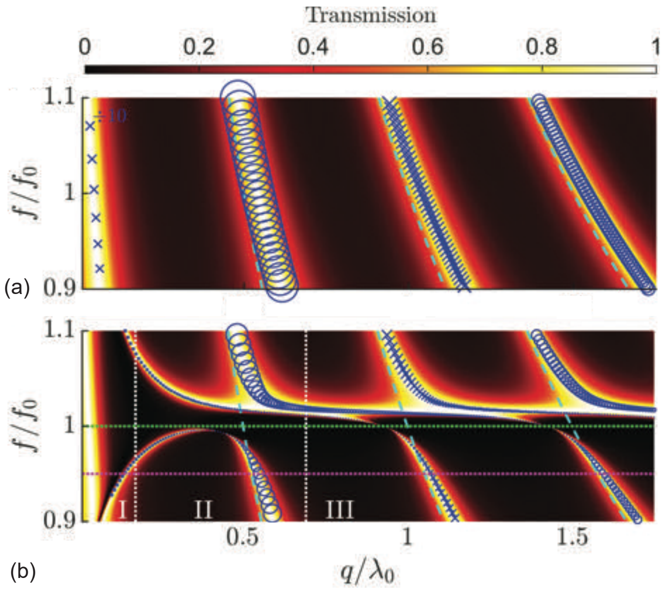

Figure 4.11: (a) Transmission map for two unpatterned slabs of thickness $h = 100\,\text{nm}$ with a effective refractive index calculated by r and a of (b) [71]. (b) Transmission map of two PhC slabs for varying frequency and separation between the two PhCs at $\lambda_0 = c/f_0 = 1550\,\text{nm}$. The PhC parameters are $r = 236\,\text{nm}$ and $a = 930\,\text{nm}$ for a GaAs device layers thickness of $h = 100\,\text{nm}$. The cavity eigenmodes are overlaid in blue as crosses (circles) signifying their even (odd) symmetry in the out-of-plane direction. The horizontal green line signifies the resonance of the PhC. The cyan lines signify the Fabry-Pérot resonances. The vertical lines signify the three regions of interactions : near field [$q \lesssim \lambda_0/(2n_{eff}) \approx 270\,\text{nm}$], intermediate field [$\lambda_0/(2n_{eff}) \lesssim q \lesssim \lambda_0/(2n_{eff})$], and far field ($q \gtrsim \lambda_0/(2n_{eff}) \approx 1000nm$). n_{eff} is the effective refractive given by $n_{eff} = (1-\eta)n + \eta$ where $\eta = \pi a^2/r^2$ and n is the refractive index. Images taken from Ref. [71].

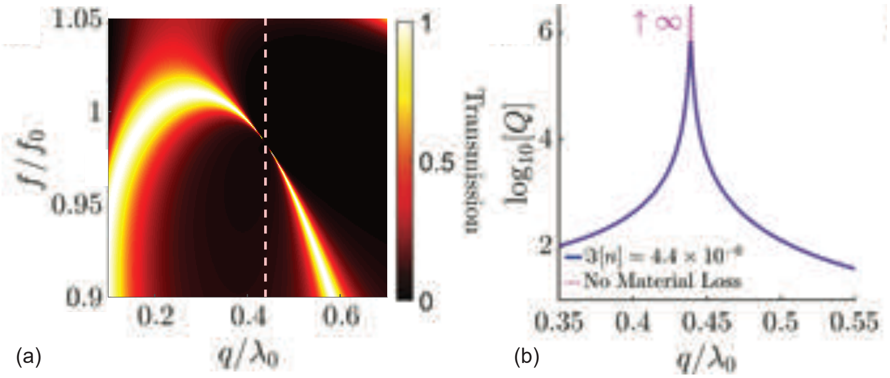

Figure 4.12: (a) A detailed look at the transmission map of two PhC for varying frequency and separation between the two PhCs at $\lambda_0 = c/f_0 = 1550\,\mathrm{nm}$. The PhC parameters are $r = 418\,\mathrm{nm}$ and $a = 1081\,\mathrm{nm}$ for a GaAs device layer thickness of $h = 100\,\mathrm{nm}$. The vertical line signifies the gap at which the linewidth becomes zero. (b) The quality factor of the cavity around the BIC seen in (a). The red dashed line takes no absorption into account. The blue line takes into account absorption of GaAs at $\lambda = 1550\,\mathrm{nm}$. Images taken from Ref. [71].

the PhCs having a mechanical frequency of $\Omega_m/2\pi = 150\,\mathrm{kHz}$ and a realistic mechanical quality factor of $Q = 10^8$ in a suitable material system (such as SiN, crystalline Si, InGaP) can reach single-photon quantum cooperativity greater than unity [71]. However, in reality, a BIC cannot be realized as the system will always be limited by material losses. Another aspect that needs to be taken into account is that it would be impossible to couple light into a BIC. Therefore, 'quasi'-BICs need to be engineered to take advantage of BICs in an optomechanical system. Quasi-BICs are high-Q leaky modes that can couple to the environment and hence can be accessed [96], [97]. The experimental realization of a BIC in the III-V material system discussed in this thesis would require the removal of the substrate and is left for future work.

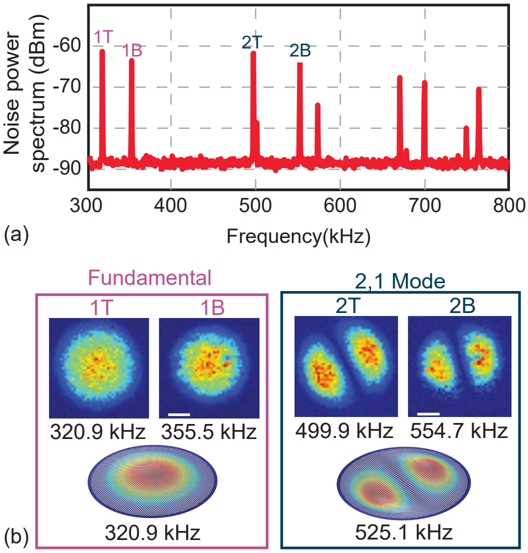

Figure 4.13: a) Noise power spectrum of the double layer device with T and B representing the top and bottom membrane respectively. (b) Measured mode tomography along the simulated mode profile of the fundamental and first higher order mode of the top and bottom membrane [65], [66].

Mechanical properties of a resonator array

In Fig. 4.13(a), we see the NPS of Device B. The mechanical modes of both the top and bottom mechanical resonator are present in the spectrum. This is identified by performing mode tomography on each of the modes. We see that we obtain identical mode shapes for two modes meaning the two resonators in the array are fully released. Since, we etch both the devices in the same step we would expect the resonators to be identical. This would mean the eigenfrequencies of the two resonators would be the same. In our devices, we observe that the frequencies for the same modes of the two resonators differ as seen in Fig. 4.13(b). This can be a result of the minor deviations in the radii of the PhC between the two devices during the dry-etch and release during fabrication. Another factor that can explain the difference in frequencies is the tensile stress in the layers. Ideally, the device layers should have no tensile stress as the sacrificial AlGaAs layer thickness of 730 nm should not allow AlGaAs to relax. But as we discussed in Sec. 4.1.1 and Ref. [21], the modeling of the critical thickness has huge uncertainty based on the model that is chosen [21]. Hence there can be a difference in the tensile stress of the two GaAs layers. A difference in the tensile stress of 2.5 MPa can result in an eigenfrequency difference of approximately 30 kHz according to FEM simulations. The mechanical Q-factor of the two membranes was measured to be $\leqslant 5 \cdot 10^4$. This value is lower than the quality factor observed in Device A. This is expected as the membrane has a significantly larger connection to the support compared to the free-free geometry but, does not show buckling. This would mean the energy loss via clamping losses would be higher in membranes leading to a reduced Q [73].

Optomechanics in the PhC-PhC system

In Device B, we have two suspended PhCs that form an optical microcavity. In other words, we have two mechanical resonators and an optical cavity that interacts with them. This should result in observable optomechanical effects such as mechanical frequency shift via the optical spring effect.

In Fig. 4.14(a), we see the NPS of the device for varying wavelength of

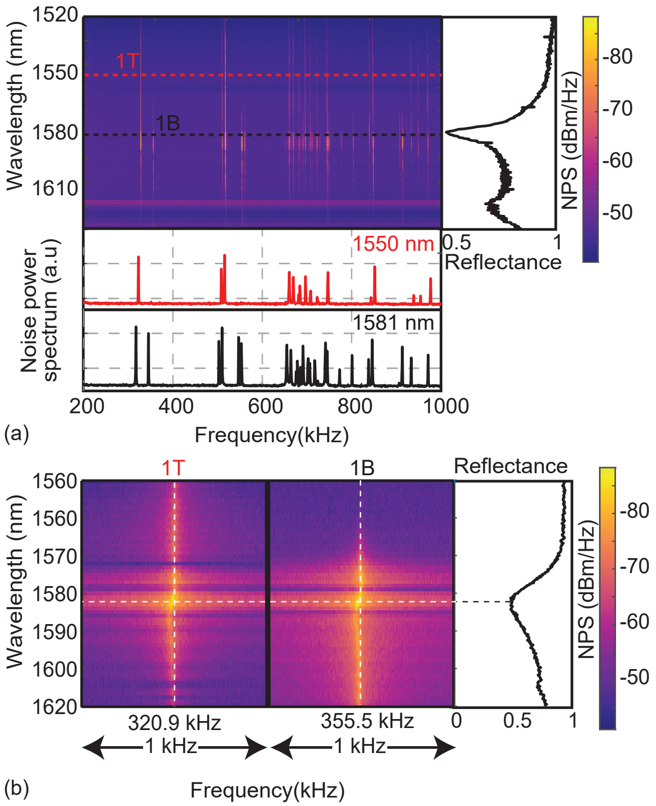

Figure 4.14: Noise power spectrum of a Device B measured at varying wavelength (top left). The red (black) horizontal dotted lines show the noise power spectrum measured at 1550 nm (1581nm), see bottom of panel. The reflectance spectrum of the device is shown in the top right panel. (b) A closer look the NPS of the fundamental mode of the top and bottom membrane seen in (a). The span is 1 kHz with the central frequency as mentioned. The reflectance of the device is shown in the right panel.

the incident light. For wavelengths between 1520 nm and 1560 nm we observe some mechanical peaks. But, as the wavelength is increased we see additional peaks appear in the NPS. Looking at the reflectance of the device shown in the right inset of Fig. 4.14(a), we can observe that between 1520 nm and 1560 nm the reflectance of the device is high. This would result in the light being reflected off the top membrane. As a result, we only see the mechanical modes of the top membrane between 1520 nm and 1560 nm. As the wavelength is increased further, light couples into the microcavity formed between the two PhCs. This results in the light interacting with the bottom membrane also. Therefore, the mechanical modes of the bottom membrane are seen in the NPS. This is another method - an alternative to mode tomography, to identify the individual modes of the top and bottom membranes.

In Fig. 4.14(b), we take a closer look at the fundamental mode of the top and bottom membrane. We can observe that when the wavelength is detuned with respect to the microcavity resonance, the mechanical frequencies of the top and bottom membrane show some deviation. Additionally, the amplitude of the mechanical mode also changes. The system has two PhC mirrors whose individual reflectance is highly frequency-dependent. The minor deviations between the radii of the two PhCs cannot be dependably measured leading to deviations in the modeled optical properties. Additionally, the PhC mirrors have a sub-µm gap between them, which also opens the possibility of evanescent coupling between the two guided PhC resonances. This coupling would modify the cavity mode and consequently the optomechanical interaction. This makes it more complicated to model the optomechanical effects observed in the system.

In Device B we show that monolithic resonator arrays can be fabricated in III-V materials. The resonators in the array are mechanically uncoupled from each other and can be independently addressed. A microcavity is formed between the PhCs, which is a stand-alone cavity optomechanical system. On the one hand, the interference that takes place between the guided resonances of the PhCs and the microcavity offers the possibility to tune the cavity linewidth via BICs. On the other hand, this makes the system difficult to model to understand the optomechanical effects. Hence, we move to a simpler device geometry, where a microcavity is formed by a frequency dependent reflector - PhC and a frequency independent reflector - DBR in Device C.

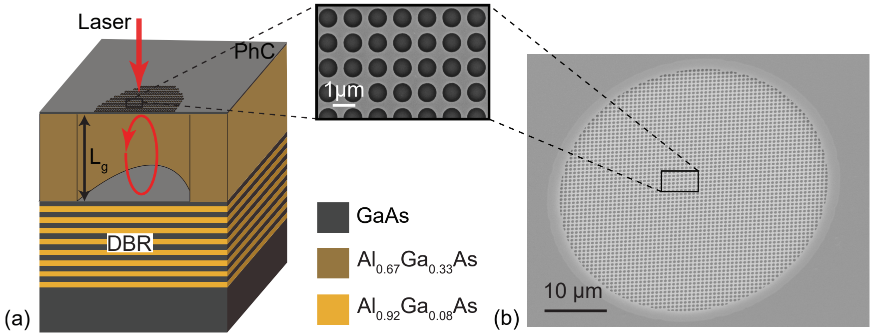

Figure 4.15: (a) Schematic of Device C showing the microcavity formed between the PhC and the DBR. (b) SEM image of a single-layer PhC suspended on top of a DBR. A closer view of the PhC is also shown.

4.1.3 Single-layer GaAs and DBR system

In the previous section, we showed that monolithic mechanical resonators can be realized in the III-V material system. However, an integrated optomechanical system would also need at least one of the mirrors to be part of the monolithic structure. Hence, we use a AlGaAs heterostructure as seen in Fig. 4.15(a) that consisted of a distributed Bragg reflector (DBR) upon which the sacrificial AlGaAs layer and a GaAs device layer were grown. The DBR comprised of 30 pairs of alternating layers of 105.9 nm-thick $Al_{0.92}Ga_{0.08}As$ and 130 nm-thick GaAs. The DBR was followed by a 750 nm-thick $Al_{0.67}Ga_{0.33}As$ sacrificial layer and a 100 nm-thick GaAs device layer. The devices were fabricated with the process described in Sec. 3.2.1, similar to Device A and B.

As in Device B, a fully clamped membrane with a patterned PhC was the preferred geometry used to realize the mechanical element. The openings that were present to efficiently flush the etch-by products out in Device B were omitted in this design. This was initially done to avoid over-etching into the DBR during the dry-etch step. The etch rate is directly proportional to the area that is exposed to the plasma. If the AlGaAs in the DBR is exposed during the wet-etch step, the high Al-content AlGaAs in the DBR would be etched in an uncontrollable manner. This would damage the DBR and may also lead to device failure. We observed that there were no issues in fabricating the devices. A clean release without any etch remnants even without the openings was achieved. A SEM of a single-layer PhC on a DBR is seen in Fig. 4.15(b).

Microcavity engineering

In Device B, we observed that a microcavity is formed between the two PhC membranes. In Device C, we fabricate a PhC with varying radii to investigate its effect on the behavior of the microcavity and the reflectance in general. To this end, we fabricated devices with PhC radii varying from $r = 420\,\mathrm{nm}$ to $r = 350\,\mathrm{nm}$ with the lattice constant $a = 1081\,\mathrm{nm}$ on the same chip. In Fig. 4.16 we see the reflectance of one such microcavity formed between a PhC with $r = 367\,\mathrm{nm}$ and $a = 1081\,\mathrm{nm}$. We observe three distinct features in the spectrum. First, the reflectance minimum at 1508 nm. The dip is asymmetric which points to it being a Fano resonance. The Fano lineshape is a feature of the frequency-dependent reflectance of the PhC [59], [67]–[70]. We look at the electric field in the device at this wavelength to see that the field is distributed between the PhC and the DBR and is highly concentrated close to the PhC. Hence, the dip at 1508 nm is attributed to be the microcavity resonance. Second, we observe a dip at 1573 nm. This is a parasitic guided resonance similar to the one observed in Device A and Device B discussed in Sec. 4.1.1 and Sec. 4.1.2, respectively. The light that is incident at the PhC oblique angles due to the finite waist of the Gaussian beam couples into the parasitic guided resonance leading to the drop in reflectance [21], [64]. Finally, we look at the local minima at 1560 nm and 1600 nm. These are the first two transmission minima of the DBR. This was verified by stripping the top layers and measuring the reflectance of only the DBR seen in Fig. 4.16 (orange dots). The difference in amplitude is due to the presence of the PhC that increases the overall reflectance in the region where the DBR minima occur.

We see that the simulated spectrum is in good agreement with the measured reflectance for the aforementioned features. However, we do see some discrepancies. The deviation in the dip depth of the microcavity resonance and of the DBR minima between experiment and simulation is not captured. These differences can be attributed to the assumptions made during the simulations and certain simplifications made during the modeling of the device. First,

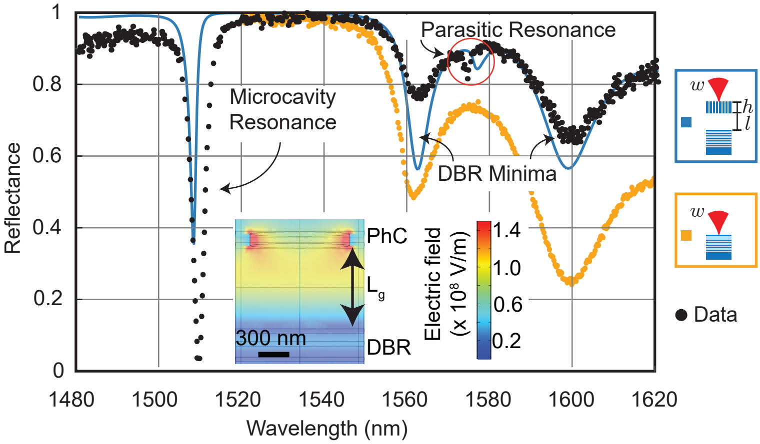

Figure 4.16: Reflectance spectra of a PhC-DBR microcavity with a PhC lattice constant of 1081 nm and PhC radius of $r_{PhC} = 367$ nm. The black dots show the measured reflectance and the blue solid line shows the simulated spectrum. The three main features observed in the reflectance spectrum - the microcavity resonance, the parasitic resonance and the DBR minima are marked. The reflectance of only the DBR after stripping the top layers is shown in orange. The inset shows the FEM simulation of the electric field distribution in the microcavity mode.

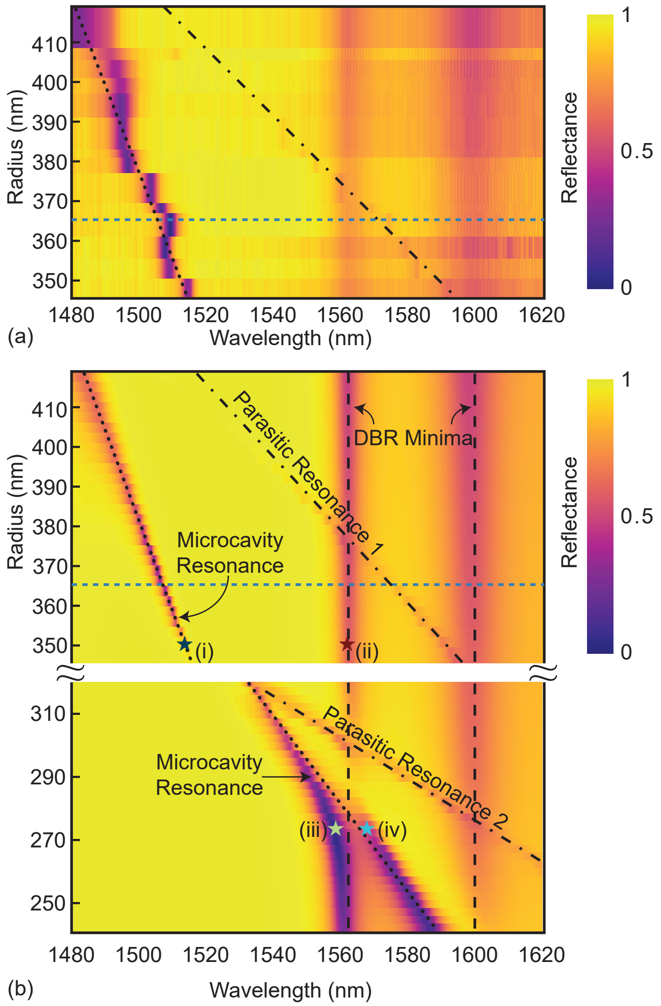

Figure 4.17: (a) Measured reflectance map of the PhC-DBR microcavity for varying PhC radii. (b) Simulation of reflectance map of a PhC-DBR microcavity with parameters as in (a) and increasing radii. The black dashed, dotted and dotted-dashed lines represent the DBR minima, microcavity resonance and parasitic PhC guided resonances, respectively. The horizontal dashed line signifies the reflectance spectrum of the device showcased in Fig. 4.16.

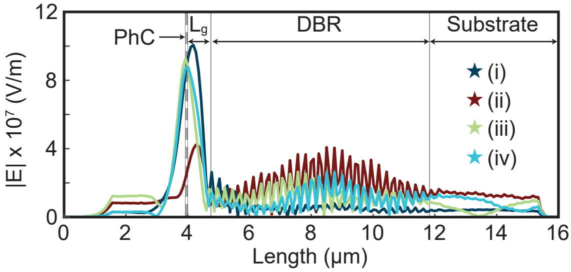

Figure 4.18: The electric field distribution, $|E|$, in the microcavity and DBR at the points marked in Fig. 4.17(b).

the RCWA simulation assumes an infinite in-plane PhC whereas in reality we have a finite-size PhC structure. Second, the simulation cannot account for fabrication imperfections that lead to a variation of the PhC radii over the patterned area. Finally, any deviation from the ideal vertical hole profile leads to an increase in the loss of the PhC guided resonance due to coupling between TE and TM modes inside the PhC slab [105], [118], resulting in a change of the PhC reflectance. The three reasons listed above will all change the reflectance of the PhC and therefore affect the reflectivity mismatch between the PhC and DBR resulting in a change in the dip depth of the microcavity resonance.

As shown in Fig. 4.16(a), the majority of the electric field is concentrated in the PhC. Hence, any variation in the PhC should result in a change in the microcavity behavior. In Fig. 4.17(a), we look at the reflectance map of the microcavity for 14 different PhC radii varying from $r = 350\,\text{nm}$ to $r = 420\,\text{nm}$. A precise control on the microcavity resonance can be obtained by tuning the PhC radius. The simulated reflectance is in good agreement with the measured reflectance for varying radii as seen in Fig. 4.17(b). We see that as the radius is reduced below $r = 340\,\text{nm}$, which is outside the radii window of fabricated devices, the simulation shows another parasitic guided resonance. By reducing the radii further, we observe an avoided crossing between the first DBR minimum and the microcavity resonance. The avoided crossing occurs due to the coupling between the microcavity mode and the transmission mode of the DBR which leads to the formation of new eigenmodes. We investigate these by simulating the electric field distribution of these new modes in

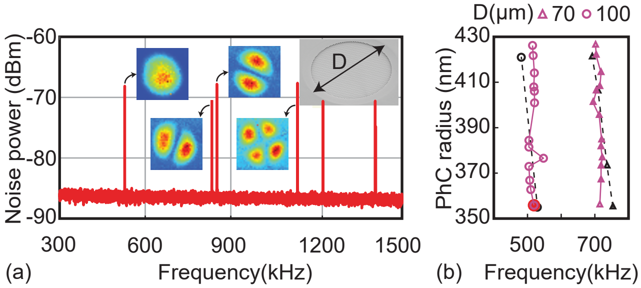

Figure 4.19: (a) NPS of a PhC membrane (SEM image in top right inset) of diameter 100 µm. The insets show the mode shape of the first four modes recorded via mode tomography. (b) Measured mechanical frequencies of the fundamental mode of suspended PhC membranes with varying PhC radii. The triangle (circle) represents the PhC mirror with a diameter of 70 µm (100 µm). The red filled circle marks the device whose NPS is shown in (a). The black triangles (circles) show the frequencies of the fundamental mode of similar devices simulated in FEM. Lines are a guide to the eye.

Fig. 4.18. We see that for the microcavity mode and the DBR mode (marked (i) and (ii) in Fig. 4.17(b) respectively), the field is mainly concentrated in the microcavity region and DBR, respectively. At the avoided crossing (marked (iii) and (iv) in Fig. 4.17(b)), we observe that the microcavity and DBR modes couple and the energy is distributed between the two modes.

Mechanical properties of the PhC membrane

In Fig. 4.19(a), we see the NPS of a suspended PhC membrane with a diameter of 100 µm. We can identify the different mechanical modes of the PhC membrane by performing mode tomography. The mode shapes are seen as insets close to the corresponding mechanical peak in Fig. 4.19(a). As just discussed, we see a discernible effect of the variation of the PhC radii on the optical response of the PhC-DBR microcavity. Now, we investigate the response that the PhC radii variation has on the mechanical response. In Fig. 4.19(b), we plot the fundamental frequency of the PhC membranes of diameter 70 µm and 100 µm with varying PhC radii. We see that the PhC radii change has mini-

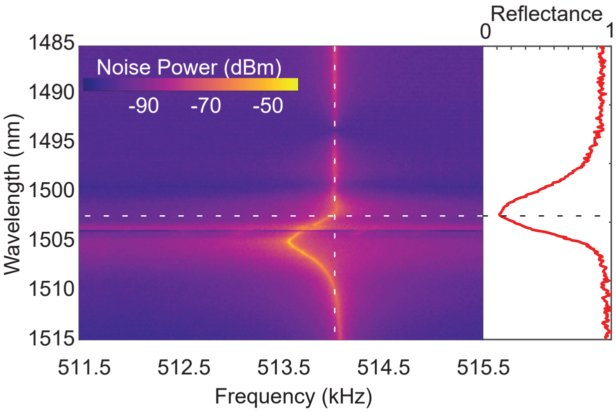

Figure 4.20: Optical spring effect in PhC-DBR optomechanical cavity. The NPS of the fundamental mode of the suspended PhC membrane exhibits a frequency shift for laser detunings close to the microcavity resonance. The optical reflectance of the microcavity is seen in the right panel. The horizontal and vertical lines signify the the optical cavity resonance and the unperturbed mechanical frequency, respectively.

mal impact on the mechanical frequency of the membrane. This response of the mechanical frequency to PhC radii change is expected. The mechanical frequency is directly proportional to the ratio of the stiffness and mass of the PhC membrane. Both entities increase with a decrease in PhC radius, and therefore the ratio does not change much. This leads to only a slight change in mechanical frequency as reflected in the measurement. This hypothesis is confirmed by performing FEM simulations of the PhC membranes (dashed line in Fig. 4.19(b)), whose results show good agreement with the measured mechanical frequencies when assuming an initial tensile stress of 45 MPa in the GaAs device layer. We observe a mechanical quality factor of $\leqslant 3 \cdot 10^4$, which is similar to Device B, and thus, expected.

Integrated cavity optomechanics

In order to observe the optomechanical effects in the PhC-DBR microcavity system, we measure the mechanical response of the resonator while the inci-

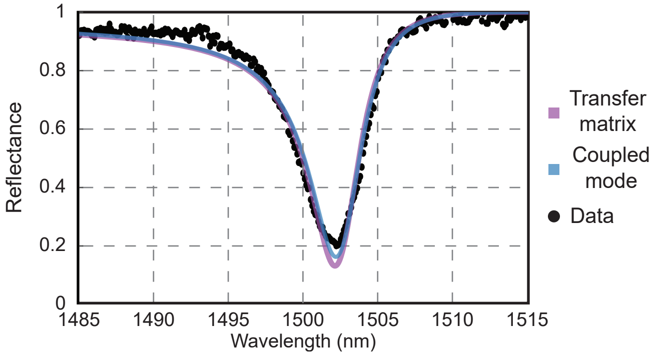

Figure 4.21: Reflectance of the PhC-DBR micrcavity. The measured reflectance of the microcavity is fitted with the reflectance obtained from the transfer matrix method (purple) and the couple-mode thoery (blue).

dent laser beam is detuned with respect to the cavity. In Fig. 4.20, we see the NPS of the fundamental mode of the PhC patterned mechanical resonator. The mechanical frequency shift is asymmetric with respect to the microcavity resonance. We observe that the amplitude of the mechanics reduces around 1495 nm which would point towards a process that leads cooling of the mechanical resonator. Red-detuning of the laser beam (i.e. $\lambda > 1503\,\text{nm}$) leads to the reduction of the frequency of the mechanical resonator. Additionally, an increase of the area under the NPS of the mechanical mode is observed when the cavity is red-detuned. Interestingly, the maximum frequency shift is not observed at the cavity resonance. A slight frequency increase is observed when the laser beam is blue-detuned ($\lambda < 1503\,\text{nm}$).

We model the measured optomechanical response of the PhC-DBR system to optomechanics in frequency-dependent reflectors discussed in Sec. 2.5.1. The modeling requires the 'quantum optics' parameters used in the Langevin equations seen in Eq. 2.62. The measured reflectance spectrum is used to determine these parameters. However, some of these parameters cannot be experimentally determined, therefore we use the transfer matrix method as a bridge between the measured response and the coupled-mode theory presented in Sec. 2.5.2 [69]. In Fig. 4.21, we see the measured optical response of the microcavity and the optical response modeled using the transfer matrix method (purple) and coupled-mode theory (blue). First, we fit the measured optical response to the reflectance from the transfer matrix model with polarizability of the two mirrors (ζ_{PhC} and ζ_{m} in Fig. 2.13) and the phase acquired during propagation as free parameters. Second, we fit the transfer matrix response to the reflectance from coupled-mode theory seen in Eq. 2.68. Here, we use ω_a and κ_1 as fit parameters. The method of parameter estimation is described in detail in Sec. 6.1 [69].

In Fig. 4.22(a), we observe the power-dependent frequency shift in the PhC-DBR optomechanical system. The amplitude of the frequency shift increases with increasing power. A minor change in the frequency response when the laser is blue-detuned is observed. There is no observable non-linear effects in the frequency shift at higher incident power. In Fig. 4.22(b), we compare the measured mechanical frequency shift to the frequency shift obtained by the different models discussed in this thesis i.e., canonical optomechanics, photothermal optomechanics and optomechanics with frequency-dependent reflectors.

The symmetric frequency shift expected from a canonical optomechanical system (Sec. 2.41) is not observed in the measurement. For instance, the positive frequency shift when the laser beam is blue-detuned is not observed. The negative shift in the red-detuned wavelengths is almost two orders lesser than the measured shift. The frequency shift expected from the photothermal optomechanics would have the maximum shift at cavity resonance as the photon number is maximum. Similar to the canonical optomechanics, the amplitude of the frequency shift from photothermal effects is two order smaller than the measured shift. The possibility of photothermal optomechanics being prevelant in this system is minimal as the operating wavlength ($\lambda = 0.8$ eV) lies in the bandgap of GaAs (1.4 eV). Using the model for optomechanics with a frequency dependent reflector (Sec. 2.5.1), we obtain a frequency shift that follows the trend of the measured data in two ways. One, the red-detuned incident beam leads to a negative frequency shift and the maximum of the frequency shift is red-detuned with respect to the microcavity resonance.

The models discussed in this thesis do not fully capture the measured mechanical frequency shift in the PhC-DBR system. This would point to additional physics that come into play in this system that are currently not taken into account in the modeling of the system. We can speculate on a few of

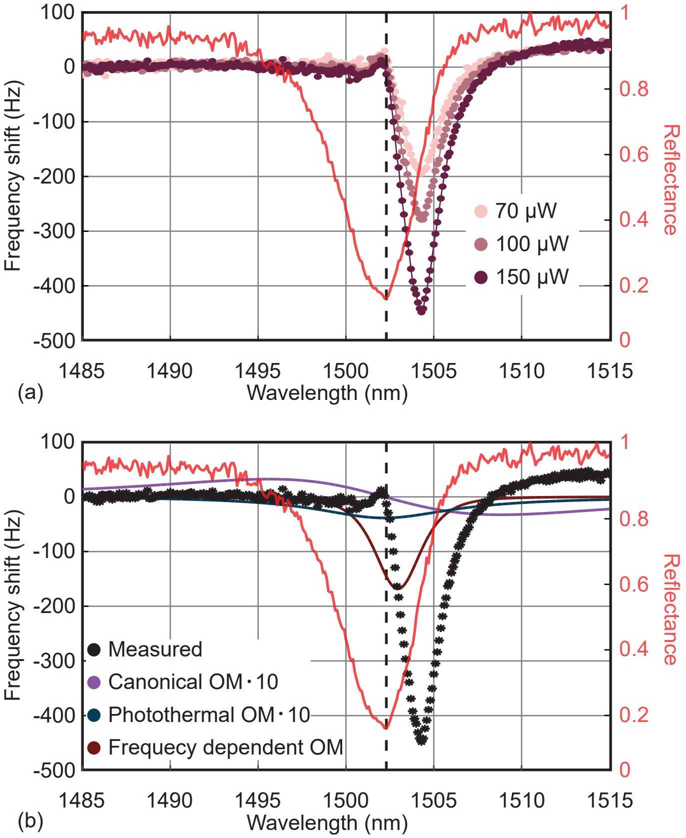

Figure 4.22: (a) Mechanical resonance frequency shift observed while detuning the incident laser with respect to the microcavity resonance for different optical powers. The solid lines are a guide to the eye. The reflectance spectrum of the corresponding microcavity is also shown. (b) Comparison of the measured frequency shift with the frequency shift expected from canonical optomechanics (purple), photothermal optomechanics (blue) and frequency-dependent reflector optomechanics (brown). The reflectance spectrum of the corresponding microcavity is also shown.

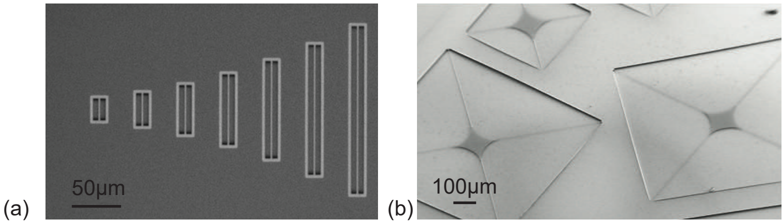

Figure 4.23: InGaP mechanical resonators. (a) SEM image of InGaP string resonators of varying length. (b) SEM image of trampoline resonators with varying tether length and orientation.

the effects that are probable in this system. The sub-µm gap between the PhC and DBR can lead to evanescent coupling between the guided resonance and the field that penetrates the DBR. The highly frequency-dependent PhC could also lead to additional dissipative optomechanical effects as observed and discussed in Refs. [67], [70], [89]. Further investigation and modeling would be needed to completely understand the optomechanically induced frequency shift measured in the PhC-DBR optomechanical microcavity.

4.2 InGaP-based optomechanical systems

In the GaAs-based devices discussed in Sec. 4.1, the maximum mechanical quality factor achieved was $3 \cdot 10^5$ in Device A. This Q-factor is low compared to SiN- [8], [9], [16], [17], [119]–[122], Si- [14] and SiC-[11], [123] based devices which have mechanical quality factors ranging from 10^6 to 10^{10}. The low Q-factor in our devices is due to the low tensile stress in GaAs. However, the SiN-, Si- and SiC-based devices do not have the advantages of III-V materials when it comes to realizing monolithic integrated cavity optomechanical devices. Hence, we choose to alter the material in our optomechanical devices from GaAs to InGaP - a member of the III-V material family that can be grown on AlGaAs-based heterostructures with tensile stress of up to 1 GPa.

We fabricate one-dimensional string resonators to determine the material properties of InGaP. The material properties of the resonators determine its mechanical properties such as eigenmodes and quality factors. The mechanical properties of string resonators are analytically modeled [73]. Hence, they can be used for the purpose of determining the material properties. Following the string resonators, we fabricate two-dimensional trampoline resonators. The trampoline geometry is a simple geometry that utilizes strain engineering that is conducive to out-of-plane coupling to light. The thin, long tethers of the trampoline isolate the central pad from the environment. This is possible because the stress concentrates in the tethers after the release leading to dissipation dilution [8], [10], [11], [14]–[16]. The central pad can be patterned with a PhC to engineer the reflectivity of the resonator. The string and trampoline resonators are fabricated using the process described in Sec. 3.2.2. In Fig. 4.23 we show released InGaP-based string and trampoline resonators.

4.2.1 InGaP string resonators

Micromechanical resonators fabricated in InGaP on AlGaAs heterostructures have been demonstrated recently in membrane-type [30] and string-type geometries [31], [32]. Membrane-type micromechanical resonators have showcased quality factors of up to 10^6 at room temperature [30]. Further, it was experimentally confirmed that stress is anisotropic in InGaP [31], which opens up novel pathways for utilizing strain engineering in crystalline nano- and micromechanical resonators. The mechanical properties such as Young's modulus E, intrinsic strain ϵ, intrinsic quality factor Q_{int} of InGaP are important parameters that determine the quality of the mechanical resonators that can be fabricated in the material system. Hence, we use one-dimensional string resonators to evaluate the aforementioned material properties of InGaP. We fabricate string resonators of varying lengths oriented along different crystal directions and use Eq. 2.2 to fit the measured mechanical frequencies by using releases stress σ as the fit parameter.

In Fig. 4.24(a), we look at the fundamental mode of the different strings with lengths varying from 20 µm to 155 µm. We use Eq. 2.2 to fit the measured frequencies and estimate the stress to be $\sigma(0°) = (467.7 \pm 7.1)\,\text{MPa}$, $\sigma(45°) = (313.3 \pm 5.4)\,\text{MPa}$ and $\sigma(90°) = (374.9 \pm 16.4)\,\text{MPa}$ along three crystal directions.

Based on crystal symmetry, we would expect the stress along perpendicular

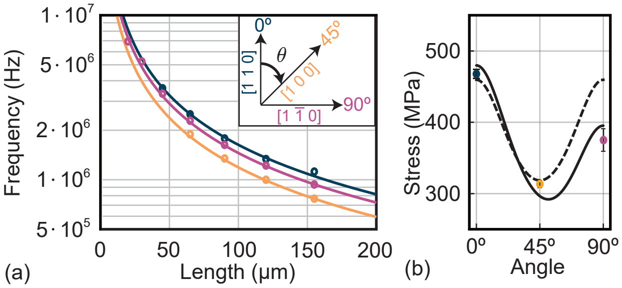

Figure 4.24: Tensile stress of InGaP string resonators. (a) Eigenfrequencies of the fundamental mode of 73 nm-thick InGaP string resonators of different lengths for a width of 200 nm along the three crystal directions [1 1 0] (0°), [1 0 0] (45°), and $[1\,\bar{1}\,0]$ (90°). The lines are a fit to the expected frequencies according to Eq. 2.2. (b) The extracted tensile stress along different crystal directions is shown as points. The dashed line shows the tensile stress $\sigma(x,\theta)$ predicted from in-plane strain $\epsilon(x)$ and Young's modulus $E(x,\theta)$, see Eq. 2.20. The solid line shows the tensile stress that takes into account an additional angle-dependent contribution to Young's modulus. Image taken from [33].

directions to be the same as seen by the dashed line. However, we observe that the stress along 0° and 90° is not the same. This behavior has also been observed in other InGaP works [31]. The deviation can be modeled assuming an additional modulation of the Young's modulus that follows a $\cos(2\theta)$ function. The deviation, i.e., $\Delta\,E(x,\theta)$ is given by

$$\begin{aligned}\Delta\,E(x,\theta) &= \sigma(\theta)/\epsilon(x) - E(x,\theta)\\ &= \alpha + \beta\cos(2\theta).\end{aligned} \tag{4.1}$$

The resulting Young's modulus will be $E(x,\theta) + \Delta\,E(x,\theta)$ [31], [33] with the values of $\alpha = -5.9\,\mathrm{GPa}$ and $\beta = 11.3\,\mathrm{GPa}$. We see that by taking into account the modified Young's modulus we get a good agreement with the estimated relaxed stress via measurements. The reason for this deviation may be a defect density arising from dislocations being greater along one crystal direction [31].

The initial stress in the device layer is redistributed in the fabricated device after release. The geometry of the mechanical resonator determines the stress concentration in certain regions. As a rule of thumb, the smaller the region, the higher the stress concentration. Also, sharp corners in the geometry are regions of high stress concentration. If the stress in a region exceeds the yield stress - the stress at which the material fractures, then the device will break. Therefore, when designing micro-mechanical resonators in high stress materials, it is critical to keep in mind that the yield stress should not be exceeded in any region.

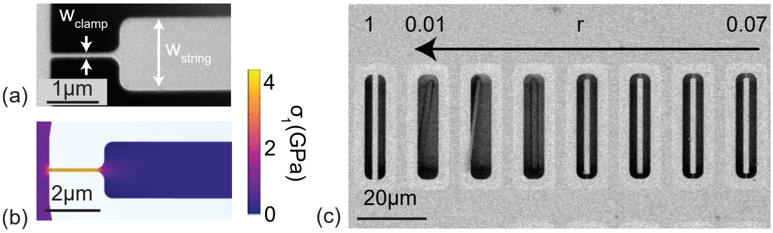

Figure 4.25: Yield strength of InGaP.(a) SEM image of the tapered clamp region of a string resonator. (b) FEM simulation of the first principal stress, σ_1, of the tapered region (c) SEM image of tapered string resonators oriented along 0°. Resonators of $r < 0.06$ (dashed line) fracture. Image taken from [33].

To estimate the yield strength of InGaP, we utilize tapered string resonators. The approach is adopted from Ref. [12] albeit for SiN. In Fig. 4.25(a), we see the SEM image of one such tapered string resonators. The width of the string resonator w_{string} is kept constant whereas the width of the clamping region w_{clamp} is reduced. As discussed above, as the region of the released resonator gets smaller, the stress in that region increases. While reducing the width of the clamping region, we observe that after a certain w_{clamp} the strings fracture at the tapering region seen in Fig. 4.25(c). Since InGaP is anisotropic, the yield stress is also anisotropic. Therefore, we fabricate the tapered string resonators along three crystal directions and find the w_{clamp} after which the strings fracture. On the same device, we fabricate a string resonator with no tapering whose stress is calculated using Eq. 2.2. Then, the yield stress can be calculated analytically, which gives [10], [33]

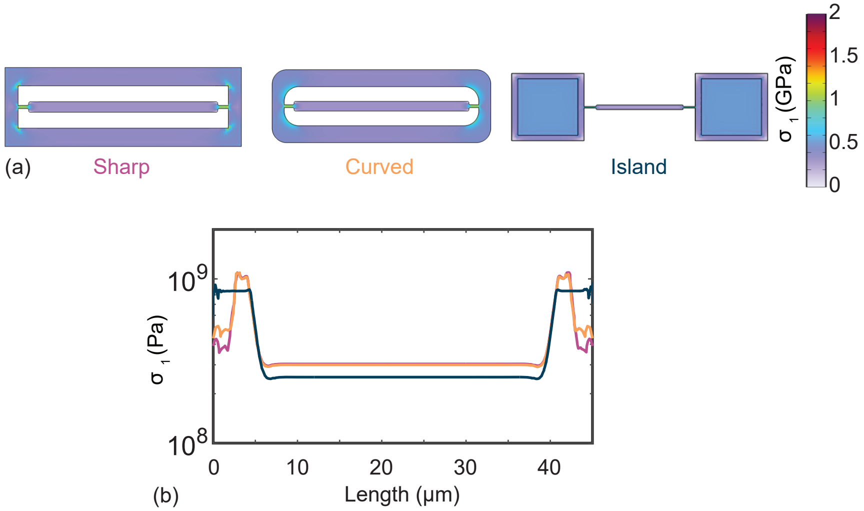

Figure 4.26: (a) FEM simulations of the first principle stress in the released tapered string resonators with three different supports. (b) The first principle stress along the string for different supports seen in (a)

$$\sigma_{\text{yield}} = \sigma_{r=1}/r_{\text{yield}}, \tag{4.2}$$

where $r = w_{\text{clamp}}/w_{\text{string}}$ considering the w_{clamp} of the first tapered resonator that breaks. This method resulted in the yield stress values of (5.5 ± 0.8) GPa, (3.3 ± 0.5) GPa, and (3.7 ± 0.5) GPa along 0°, 45°, and 90°, respectively [33]. Alternatively, FEM simulations to obtain the stress distribution of the first device which fractures can also be performed. The stress that is concentrated in the tapering region is seen in Fig. 4.25(b). We find that for the InGaP sample used in this thesis, the yield stress values from FEM were $\sigma_{\text{yield}}(0°, 90°) \approx 4.14$ GPa, $\sigma_{\text{yield}}(45°) \approx 3.2$ GPa.

There is a difference between the σ_{yield} obtained via the FEM simulation and the analytical modeling. The analytical model does not take into account the geometry surrounding the tapered string resonator. FEM simulations of resonators with the same tapered string but connected in different ways show a difference in the released stress as seen in Fig. 4.26. For the three different supports shown in Fig. 4.26, the first principal stress in the middle of the

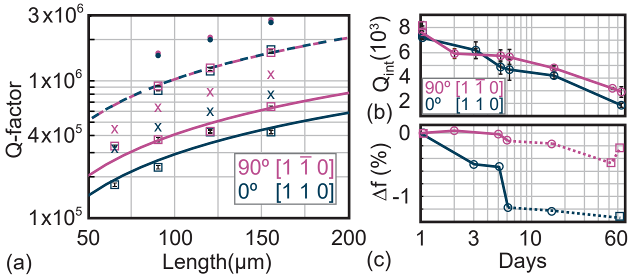

Figure 4.27: Determination of Q_{int} from InGaP string resonators. (a) Measured Q factors (squares) for the fundamental mode of string resonators with varying length oriented along 0° and 90°. The dashed (solid) lines are fits to extract Q_{int} at day 1 (day 60). The dots (crosses) show $Q_{\text{D}}^{\text{FEM}}$ obtained from FEM, when using Q_{int} from day 1 (day 60) as input. (b) We observe that Q_{int} degrades over time, shown for two samples (squares and circles). The solid (dotted) line indicates when the sample was stored in vacuum (ambient condition). (c) The relative change of the resonance frequency of the string resonators, i.e., $\Delta f = (f_{\text{day x}} - f_{\text{day 1}})/f_{\text{day 1}}$, is shown over the same time period. Taken from [33].

device is 305 MPa (Sharp), 300 MPa (Curved) and 250 MPa (Island). This can be a reason for the discrepancy in the yield strength obtained by FEM and the measurement-based analytical model.

Since we fabricated string resonators of varying length to estimate the tensile stress in the device (Fig. 4.24), the same devices can be used to estimate Q_{int}. We measure the Q-factor of the modes of the mechanical resonator with varying length. The measured Q is fitted to Eq. 2.21 and Eq. 2.23 with Q_{int} being the free-parameter. As the other material properties of InGaP we have encountered so far, Q_{int} is also anisotropic. We obtain a Q_{int} of 7550 ± 140 and 8150 ± 320 along 0° and 90°, respectively seen in Fig. 4.27(a). The Q_{int} calculated for InGaP is comparable to Q_{int} for other materials such as SiN [10], [80], Si [14] and SiC [11].

The dilution factor D^{FEM} can be calculated using FEM simulations [10], [100]. The bending and elastic energies of a particular mechanical mode can be calculated in COMSOL [100]. The dissipation dilution limited mechanical quality factor $Q_D^{\mathrm{FEM}} = D^{\mathrm{FEM}} \cdot Q_{\mathrm{int}}$ is shown in Fig. 4.27. The calculated $Q_{\mathrm{D}}^{\mathrm{FEM}}$ is slightly larger than the measured Q factor, which is also observed in other works [11], [13], [15].

Interestingly, we observed that the measured mechanical quality factor was deteriorating with time as shown in Fig. 4.27(b)[33]. One of the reasons for the Q-factor reduction can be time-dependent stress relaxation. The stress relaxation would reduce D and the corresponding Q_D. This stress relaxation should also be observed as a change in the mechanical frequency according to Eq. 2.2. But, the mechanical frequency did not show any significant change during the same duration, as seen in Fig. 4.27(c). Therefore, we can rule out any major stress relaxation that occurs in the InGaP layer. So, the reason for the Q-factor reduction can be speculated to be some change to the surface morphology such as moisture-induced degradation [124] or a growth related process [125] which increases surface losses. Further investigation needs to be carried out to establish the reason behind this time-dependent reduction of the quality factor. AFM measurements at regular intervals of released devices stored in vacuum and ambient environment can shed light upon any surface degradation that may occur. Similarly, XRD measurements can provide information about any material changes such as crystal defects that occur after the release and increase over time.

Using string resonators, we determined the relevant material properties of InGaP. Knowing these properties is crucial to design two-dimensional mechanical resonators, i.e., trampoline resonators to effectively couple to out-of-plane light. A tensile stress of $\approx 500\,\mathrm{MPa}$ can be found in InGaP device layers. This is significantly higher than the stress observed in GaAs-based devices and similar to SiN- and Si-based devices. However, a realistic method to overcome the undesired time-dependent degradation of the Q_{int} of InGaP must be found. This would enable the realization of high-Q mechanical resonators in tensile-strained InGaP that make use of methods such as strain engineering [10], [12], [14], phononic shield [16] and hierarchical support[15].

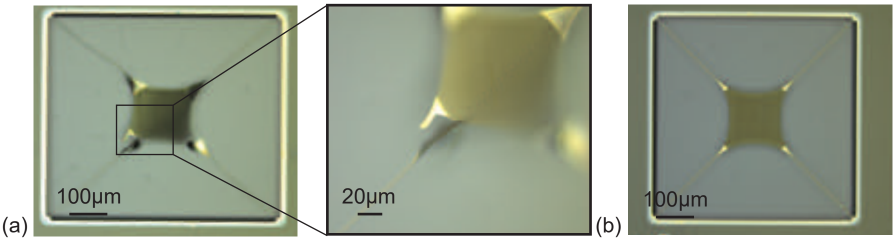

Figure 4.28: Optical microscope images of trampolines. (a) A trampoline design with PhC not going to the edge of the trampoline leading to a fracture of the device. A closer look at the fracture region is shown. (b) A trampoline design where the PhC pattern is written close to the edge and the trampoline survives and is released cleanly.

4.2.2 InGaP trampoline resonators

The simplest trampoline geometry consists of a square-shaped central pad held by four tethers connecting each of its corners to the support, see Fig. 4.28(b). The stress in the material is mainly concentrated in the tethers after release. This would stiffen the tethers thereby increasing the mechanical frequency while dissipation is not affected. Advanced architectures such as membranes or trampolines with phononic shielding [16], hierarchical structures[15], topology optimization [17] can also be implemented in InGaP. In principle, being a crystalline material, InGaP should be less affected by mechanical dissipation compared to amorphous SiN due to well-defined crystal structure and long-range order. Therefore, the strain engineering techniques can be used in InGaP and ideally would result in similar or higher mechanical quality factors compared to SiN-based micromechanical devices.

Photonic crystals in InGaP

We use PhCs to engineer the reflectance of InGaP similar to GaAs devices. The central pad of the trampoline is patterned with a PhC. The region between the photonic crystal holes is very narrow. Similar to tapered string resonators there is the possibility that the stress concentration in this narrow region is high after release, then the device might break. This is especially true of the PhCs close to the edge of the trampoline where the stress is high due to the tether. Additionally, as the sacrificial layer below is removed during wet etch, the stress in the device layer continuously redistributes itself. In the unpatterned region between the PhC holes and the tethers, there can be stress concentration in the region still attached to the GaAs layer below. This leads to the device breaking as seen in Fig. 4.28(a). It was realized that having PhC holes close to the tethers (Fig. 4.28(b)) helps prevent the devices from fracturing. Alternatively, adiabatically reducing the PhC radii at the edges of the pad increases the chances of the trampoline not getting fractured during release as shown in Ref. [126].

Fig. 4.29 shows the reflectance spectrum of an InGaP PhC on top of a GaAs substrate. The gap between the PhC and the substrate was 14.8 µm determined by a profilometer. The gap is large because the wet-etch process used to release the devices etches anisotropically and the etch-along [0 0 1] is about 3 µm min^{-1}. The wet etch is performed for 5 min to fully release the device. Since there is no etch stop layer, the etching continues until the sample is removed from the solution. We observe a dip around 1550 nm. We interpret it as being a Fabry-Pérot resonance that occurs due to the cavity formed between the substrate and the PhC trampoline. The linewidth is very broad due to the cavity formed between the PhC trampoline and the low-reflectance substrate. We observe that we get high-reflectance at 1520 nm. The reflectance map to obtain the PhC parameters for InGaP (similar to Fig. 4.2) was calculated with the value of refractive index estimated from interpolation between GaP and InP [127], [128]. Future works would involve optimizing the PhC parameters with using more accurate values of the refractive index in the wavelength region of interest [33]. One can also add an etch stop layer to gain control over the cavity length. The future implementations of the device would ideally include a DBR below the InGaP layer similar to Device C to showcase an integrated cavity optomechanical device in InGaP.

High-Q InGaP trampoline resonators

In Sec. 4.2.1, we found that the stress is different along different crystal directions. To utilize this anisotropy, we fabricate trampoline resonators with varying tether lengths and orientation along different crystal directions. We

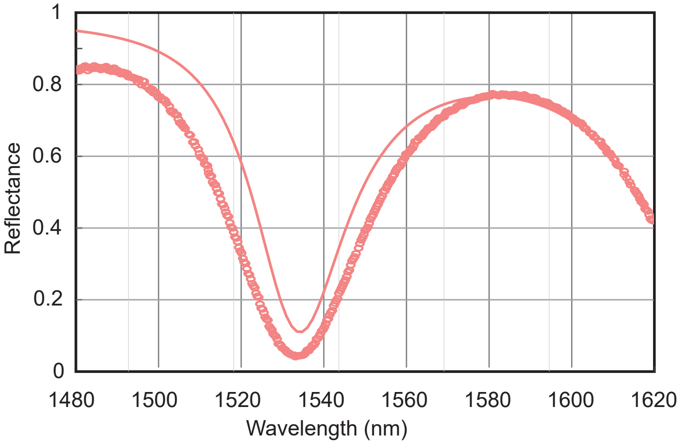

Figure 4.29: Reflectance spectrum of an InGaP mechanical resonator whose central pad is patterned with a PhC. The PhC parameters are $r = 605\,\mathrm{nm}$, $a = 1309\,\mathrm{nm}$. The thickness of the InGaP layer is 73 nm and the vacuum gap between the PhC and the GaAs substrate is about 14.8 µm. The incident light has a Gaussian beam waist of 7.5 µm. The solid line shows the simulated spectrum. Image taken from [33].

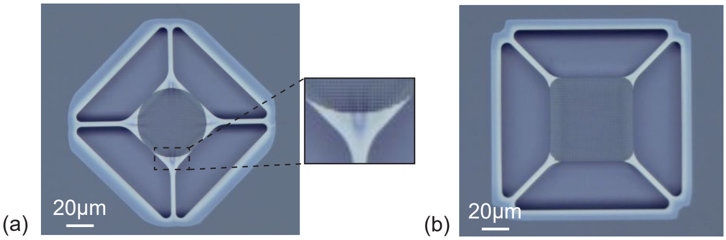

Figure 4.30: (a) Optical image of trampoline whose tethers are oriented along 0° and 90° showing buckling in the region (b) Optical image of trampoline whose tethers are oriented along 45° and 135°

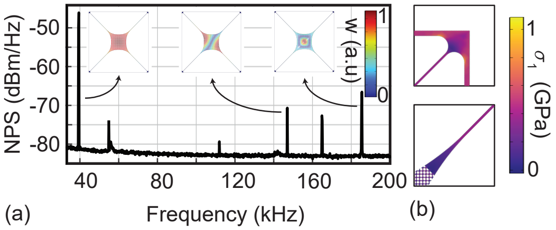

Figure 4.31: NPS of an InGaP trampoline resonator. The length of the tether is 750 µm and its width is 1 µm and are oriented along 45° and 135°. The central pad is $100 \times 100\,\mu\text{m}^2$ and patterned with a PhC. The insets show FEM simulated mode shapes of the mechanical modes of the trampoline. (b) FEM simulations showing the first principal stress in the released device at the tether connection to the pad and the support. Image taken from [33].

fabricate trampolines with tether length 200, 500 and 750 µm with the tethers oriented along 0° and 90° or 45° and 135° (see Sec. 6.3). The tensile stress being higher along the tether directions is preferred as it would increase dissipation dilution. However, due to the difference in the stress along 0° and 90° in InGaP (Fig. 4.24), we see local buckling/deformation in the central pad where it is connected to the tether as seen in Fig. 4.30(a). This would lead to additional mechanical dissipation for devices whose tethers were oriented along 0° and 90°.

In Fig. 4.31, we look at the NPS of a trampoline resonator whose tethers are oriented along 45° and 135°. The tether length is 750 µm and width is 1 µm. We simulate the eigenfrequencies of the trampoline geometry in FEM and identify the different modes. We identify the fundamental mode of trampoline resonator to be at 38.5 kHz. The FEM simulation of the first principal stress in the device is shown in Fig. 4.31(b). We observe that the stress to be concentrated in the tethers and the central pad is relaxed. The stress concentration in the tethers is an indication of dissipation dilution in these devices.

Fig. 4.32(a) shows the highest mechanical Q factor of $1.8 \cdot 10^7$ that was measured for the fundamental mode at 38.5 kHz of the InGaP trampoline with 750 µm tether length along 45° and 135° (device shown in Fig. 4.31(a)). The

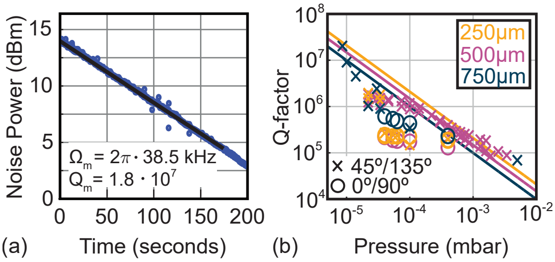

Figure 4.32: Ringdown measurement of the fundamental mode of trampoline whose NPS is shown in Fig. 4.31. We obtain a Q of $1.8 \cdot 10^7$ from a fit (solid line) to the decay. (d) The Q vs. pressure dependence for the fundamental mode of trampolines of different lengths with tethers oriented along different crystal directions. The solid lines show the quality factor limited by gas damping for trampolines of tether length 250 µm, 500 µm, and 750 µm. Image taken from [33].

Q-factor was measured at room temperature and a pressure of $8 \cdot 10^{-6}$mbar which was the lowest attainable pressure with the measurement setup available.

The time-dependent mechanical quality factor degradation seen in string resonators is also observed in trampoline resonators. Yet, to determine the limiting mechanical damping mechanism in the trampoline, we consider different damping mechanisms that come into play. First, we look at gas damping. We measure pressure dependent Q-factor of the various trampolines seen in Fig. 4.32(b). We observe a linear increase in the measured Q when the pressure decreases. This follows the expected behavior from a system limited by gas damping. Second, we look at clamping loss with the aid of PML in FEM simulations [11]. We obtain a value of $\approx Q_{\text{clamp}} > 10^8$ and hence, we can conclude that devices are not currently limited by clamping losses [33], [79].

In InGaP-based trampoline resonators, we have shown that we are able to engineer the optical properties of the resonator using PhC and efficiently couple to out-of-plane light [33]. The addition of an integrated DBR in the heterostructure would provide the opportunity for microcavity engineering similar to GaAs-based PhC-DBR microcavities as discussed in Sec. 4.1.3. The trampoline exhibits mechanical quality factors of $> 10^7$ and are currently the highest reported in the InGaP material system [33]. We show that the Q-factor is currently limited by the measurement setup and can be improved by measuring at lower pressures. This can be further improved by techniques of strain engineering [8], [14], phononic shielding [16] and hierarchical structures [15]. The current $Q \cdot f$ product of the trampoline is $7 \cdot 10^{11}$. The enhancement of the $Q \cdot f$ product by one order of magnitude would place the InGaP trampoline devices in the regime of quantum optomechanics at room temperature [8]. The mitigation of the time-dependent quality factor degradation would make InGaP an excellent material to realize monolithic integrated cavity optomechanical devices.

CHAPTER 5

Conclusions and outlook

The main objective of this thesis was to showcase the platform of integrated free-space cavity optomechanical devices in III-V heterostructures. The III-V material system allows bottom-up growth and top-down fabrication. This feature lends itself to make this material system a promising avenue to realize integrated multi-element optomechanical systems.

We have successfully demonstrated fabrication of high-reflectance GaAs-based mechanical resonators patterned with a photonic crystal. The micromechanical resonators show a mechanical quality factor of 10^5 at room temperature [21], which is on-par with other GaAs mechanical resonators [18]–[20], [22]–[29]. We have showcased the ability to perform reflectance engineering whereby the out-of-plane reflectance is enhanced using photonic crystals.

We argue that GaAs-based micromechanical resonators can be the building blocks of monolithic multi-element integrated cavity optomechanical systems.

To this end, we have realized a GaAs-based mechanical resonator array consisting of two resonators separated by a sub-µm gap between them. We have characterized the mechanical properties of both fully released mechanical resonators with photonic crystals. We have discussed the optical microcavity that is formed between the two suspended photonic crystal resonators. Since the system is a stand-alone cavity optomechanical device, we have observed an optical spring effect originating from the optomechanical interaction. These effects are not prominent as the optical cavity has a low finesse. The microcavity formed by two patterned structures like photonic crystals can form an optical bound state in a continuum. Bound states in a continuum are high-quality optical cavities with no optical losses. Such a system would allow to decouple the otherwise coupled optical loss and coupling strength in an optomechanical system. We have discussed the possibility of realizing such an optical bound state in a continuum using two photonic crystals [71].

Furthermore, we have investigated the properties of a mechanical resonator patterned with photonic crystal suspended over a distributed Bragg reflector mirror to form an integrated optomechanical microcavity. We have demonstrated a precise control over the microcavity position by tuning the photonic crystal radii. We have showcased the presence of highly-frequency dependent photonic crystal in the optomechanical system results in novel optomechanical effects [67], [69], [70]. In particular, we have discussed the mechanical frequency shift due to the optical spring effect which cannot be modeled using canonical optomechanical system dynamics or photothermal optomechanics. However, we have captured the trend of the frequency shift when modeling the system with optomechanics with a frequency dependent reflector. We hypothesize the presence of additional effects such as evanescent coupling, dissipative optomechanics in this system which need further investigation.

The microcavity approach allows us to reach an optomechanical frequency pull factor $G/2\pi$ of about 44 GHz/nm comparable to values realized in integrated systems [49], [51], [129]–[133] and fiber-based microcavities [42], [134], [135] (see Sec. 6.2) placing our microcavity in the ultrastrong coupling regime [42], [136] with a ratio of single photon coupling strength to mechanical frequency of about 0.3. Unfortunately, the large optical loss in the system masks any notable effects such a mechanical squeezing that may be observable in this regime [44].

The GaAs-based mechanical resonators discussed in this thesis show a maximum quality factor of 10^5. The mechanical quality factor has to be increased drastically for these devices to be used in quantum optomechanics experiments. We bridge the gap in quality factor by identifying another material system compatible with the AlGaAs heterostructure, namely InGaP.

InGaP can be grown with tensile stress up to 1 GPa on AlGaAs heterostructures. This allows the implementation of stress engineering to realize high-Q mechanical resonators. We have experimentally determined the material properties of InGaP relevant to mechanical resonators namely the tensile stress, the yield stress and intrinsic Q of InGaP using string resonators. We have observed an undesirable time-dependent degradation of the intrinsic Q of InGaP. Further investigations are needed to determine the cause behind this degradation.

We have demonstrated trampoline-shaped micromechanical resonators with photonic crystals in InGaP. We obtain a Q-factor of $\geq 10^7$, the highest reported to date in InGaP-based micromechanical resonators [33]. We have ascertained that the devices are currently limited by the minimum pressure, i.e, $8 \cdot 10^{-6}$mbar achievable in the vacuum setup. Hence, the Q-factor is expected to increase further at lower pressure.

Once the crucial factor of time-dependent Q degradation has been overcome, future work can be undertaken to improvethe Q-factor further. This can be achieved by using strain engineering [8], [15], [120], phononic shielding [16] and other techniques [17] already used in SiN-based resonators to obtain ultra-high Q mechanical resonators. Following this, the multi-element mechanical resonator systems comprising of suspended photonic crystals and distributed Bragg reflectors would need to be realized in InGaP heterostructures. This would showcase the potential of this material system in enhancing the coupling strength via multi-element optomechanics [54], [113]. The realization of an integrated free-space cavity optomechanical device would also require assembling the device chip with a chip-based micromirror to form the external optical cavity as was demonstrated in Ref. [47].

A robust method to find the parameters for a bound state in a continuum or photonic crystal parameters leading to linewidth reduction in III-V materials would need to be developed. Additionally, a fabrication process to reliably remove the substrate without damaging the device layers would be critical to realize these systems. This would enable to decouple the coupling strength from the optical loss rate in the two photonic crystal optomechanical microcavity. This would allow us to realize a system where g_0 is greater than the optical loss rate κ without the need of an external optical cavity. Additionally, linewidth reduction would put the system in the quantum cooperativity regime, i.e. $g_0 > \sqrt{\kappa \Gamma_m}$, or more optimistically, in the single-photon strong coupling regime. In these regimes, the interaction between the light field and mechanics is non-linear and one could observe quantum effects such as photon blockade [37] which allows for non-destructive single photon detection or the direct generation of non-classical states on mechanical resonators [38].

The field of optomechanics has seen considerable progress in the past decade. The advancements made in fabrication of ultrahigh Q mechanical resonators and the ongoing rise of quantum technology show that there is notable interest in the field of optomechanics. The current boundaries of cavity optomechanics can be pushed further, hopefully leading to significant discoveries in studying the quantum behavior of mechanical resonators.

CHAPTER 6

Appendix

6.1 Parameter estimation for the PhC-DBR microcavity

The estimation of the parameters in the quantum optics model of the cavity optomechanical system in Sec. 2.5.1 is performed by matching the measured reflectance of the microcavity to the transfer matrix model (TMM) (Sec. 2.4.2). Following this, the reflectance from the transfer matrix model is used to fit to the reflectance given by the coupled-mode (COM) model Sec. 2.5.2. The estimation is performed in the following steps :

Stage 1: Parameters of individual elements

Photonic crystal

- The actual radius r_{PhC} and lattice constant a_{PhC} of the PhC are measured using SEM.
- The reflectance of the PhC-DBR system is measured.
- Using the measured r_{PhC} and a_{PhC}, we perform a RCWA simulation of the PhC with a Gaussian beam incident on it while sweeping the thickness of the PhC d_{PhC}.
- The d_{PhC} at which the parasitic guided resonance matches the measurement is considered the actual d_{PhC}.
- The RCWA simulation of the PhC in vacuum is performed with the estimated r_{PhC}, a_{PhC} and d_{PhC}.
- The simulated reflectance is fitted to the Eq. 2.58 to estimate ω_d, γ_d and ϕ_{PhC} and the polarizaibility of the PhC, ζ_{PhC}.

DBR

- The thickness of the alternative layers of GaAs and AlGaAs is measured in a TEM/SEM.
- The reflectance of the PhC-DBR system is measured
- The TMM of DBR is done to estimate the reflectance of the system using the refractive index from literature.
- The reflectance from TMM is fitted to the measured thickness to obtain a better estimate of the thickness of the GaAs and AlGaAs layers.
- The updated values of the thickness are used in a updated TMM model.
- The polarizability of the DBR, ζ_{DBR} is estimated choosing a wavelength

in the reflectance band of the DBR and is assumed to constant in the wavelength region of interest.

Cavity length

- The reflectance of the PhC-DBR system is measured.
- The RCWA simulation of the PhC-DBR system is performed with PhC and DBR parameters estimated above while varying the vacuum gap between the PhC and DBR.
- The cavity length L_g at which the measured microcavity resonance wavelength matches the simulated resonance is taken as the cavity length.

Stage 2: Comparison of measured microcavity reflectance and TMM

The polarizabilities of the PhC and DBR, ζ_{PhC} and ζ_{DBR}, respectively along with L_g from stage 1 are the input to the transmission of the PhC-DBR system seen in Eq. 2.61. This data is fitted to the measured reflectance of the microcavity with $\phi_{\text{PhC}}, \phi_{\text{DBR}}$ and the phase accumulated during propagation, Φ_{acc} being the free parameters as seen in 4.21.

Stage 3: Comparison of TMM and COM

The parameters used in the transmission using COM (Eq. 2.68) are $\kappa 1$,$\kappa 2$, ω_a, ω_d, $gamma_d$ and λ. We estimate them as follows :

- ω_d and γ_d are the same one calculated in Stage 1.
- $\kappa_2 = \frac{FSR}{2\zeta_{\text{DBR}}}$ which is the standard loss rate for a Fabry-Pérot cavity for a highly reflective frequency-independent mirror [69]
- The frequency for which transmission is zero in the TMM model ($\zeta_{\text{PhC}} = \infty$) is $\omega = \omega_d - \gamma_d/2\zeta_0$. Assuming the same for the COM model, i.e. $t(\omega) = 0$, we obtain $\lambda = 2\sqrt{\gamma_d \kappa_1}/\zeta_0$.

- We assume $\omega_a = a{\cdot}\omega_d$ and $\kappa_1 = b{\cdot}\gamma_d$ and the transmission obtained from the TMM is fitted with Eq. 2.68, with a and b being the free parameters.

The estimated values for the microcavity seen in 4.21 is shown in Tab. 6.1.

Parameters	Initial value	Stage 1	Stage 2	Stage 3
r_{PhC}	$351 \pm 1.9\,\mathrm{nm}$	$351\,\mathrm{nm}$		
a_{PhC}	$1081 \pm 2.3\,\mathrm{nm}$	$1081\,\mathrm{nm}$		
d_{PhC}	$95 \pm 6,6\,\mathrm{nm}$	$74\,\mathrm{nm}$		
L_g	$745 \pm 4.5\,\mathrm{nm}$	$750\,\mathrm{nm}$		
d_{GaAs}	$102.4 \pm 1.9\,\mathrm{nm}$	$105.9\,\mathrm{nm}$		
d_{AlGaAs}	$137.6 \pm 2.5\,\mathrm{nm}$	$130\,\mathrm{nm}$		
λ_d		$1473.052\,\mathrm{nm}$		
$\omega_d/2\pi$		203.5		
$\gamma/2\pi$ (THz)		3.442		
ϕ_{PhC}		2.36 rad	2.12 rad	
ϕ_{DBR}		45.5 rad	45.31 rad	
Φ_{acc}			-0.2 rad	
$\kappa_2/2\pi$ (THz)				0.95
$\kappa_1/2\pi$ (THz)				21.1
$\omega_a/2\pi$ (THz)				247.1

Table 6.1: Parameter estimation for the PhC-DBR system using the Transfer matrix and coupled-mode models.

6.2 Comparison of optomechanical microcavities

Tab. 6.2 shows the comparison between the integrated free-space microcavity discussed in Sec. 4.1.3 and other integrated and fiber-based free-space optomechanical microcavities in literature. The integrated free-space microcavity exhibits a better frequency pull factor compared to the fiber-based free space systems and, is comparable to integrated systems such as optomechanical crystals and whispering gallery mode resonators.

Work	$\frac{g_0}{2\pi}$	Frequency pull factor
Integrated optomechanical microcavities		
Burek et al [49]	136 kHz	$2\pi \cdot 43.87$ GHz/nm
Schneider et al [131]	400 kHz	$2\pi \cdot 218$ GHz/nm
Guo et al [132]	237 kHz	$2\pi \cdot 21.6$ GHz/nm
Ghorbel et al [133]	380 kHz	$2\pi \cdot 240$ GHz/nm
Balram et al [129]	1.1 MHz	$2\pi \cdot 338$ GHz/nm
Mitchell et al [130]	30 kHz	$2\pi \cdot 50$ GHz/nm
Ding et al [51]	30 kHz	$2\pi \cdot 41$ GHz/nm to $2\pi \cdot 132$ GHz/nm
Free-space optomechanical microcavities		
Rohse et al [134]	69.7 kHz	$2\pi \cdot 16.4$ GHz/nm
Rochau et al [135]	5.8 kHz	$2\pi \cdot 1$ GHz/nm
Fogliano et al [42]	1.2 MHz	$2\pi \cdot 0.3$ GHz/nm to $2\pi \cdot 3$ GHz/nm
This work (Paper D)	130 kHz	$2\pi \cdot 43.7$ GHz/nm

Table 6.2: Comparison of the single-photon optomechanical coupling rate g_0 and the frequency pull factor $G = d\omega_{\mathrm{cav}}/dx$ for the integrated, fiber-based and free-space integrated optomechanical microcavities.

6.3 Mechanical frequencies of InGaP trampolines

Tab. 6.3 shows measured fundamental mode eigenfrequencies for trampolines with various tether lengths. We find that trampolines with shorter tether lengths exhibit higher resonance frequencies. We observe that trampolines whose tethers are oriented along 0°/90° have larger frequencies than the ones oriented along 45°/135° as the stress along 0° and 90° is higher than 45° and 135° (see Fig. 4.23). We obtain a good agreement to the eigenfrequencies calculated with FEM.

Tether		Frequency (kHz)	
Length (µm)	Orientation	Measured	Simulated
250	0°/90°	90.9	106.9
	45°/135°	80	90.5
500	0°/90°	54.2	62.3
	45°/135°	43.7	52.4
750	0°/90°	40.1	47.8
	45°/135°	38.5	40.1

Table 6.3: Measured and FEM-simulated eigenfrequencies of the fundamental mode of trampolines with varied tether length and orientation.

CHAPTER 7

Summary of included papers

This chapter provides a summary of the included papers.

7.1 Paper A

Sushanth Kini Manjeshwar, Karim Elkhouly, Jamie M. Fitzgerald, Martin Ekman, Yanchao Zhang, Fan Zhang, Shu Min Wang, Philippe Tassin, and Witlef Wieczorek
Suspended photonic crystal membranes in AlGaAs heterostructures for integrated multi-element optomechanics
Appl. Phys. Lett.,
vol. 116, no. 26, pp. 264001, June. 2020
©DOI: 10.1063/5.0012667 .

We show the viability of III-V semiconductors namely AlGaAs heterostructures as a possible platform for integrated multi-element optomechanical system. We fabricate suspended photonic crystal (PhC) slabs and perform their optical and mechanical characterization. We measure the eigenfrequencies of the suspended PhC slabs using homodyne interferometry. The mechanical Q-factor was measured to be up to 3×10^5 The tensile stress present in the material was calculated by performing finite element (FEM) simulations of the mechanical eigenfrequencies for varying tensile stress and matching them to the measured values. We measure the optical reflectance of the suspended PhC slabs and show high reflectance at the desired wavelength. We perform rigorous coupled wave approximation (RCWA) simulations using the S4 software package to completely understand the measured optical reflectance. This work shows that single-layer and sub-μm-spaced double-layer mechanical resonators can be directly fabricated in a monolithic manner and these resonators have good mechanical and optical properties. Such a platform opens a route for realizing integrated multi-element cavity optomechanical devices and optomechanical microcavities on chip.

7.2 Paper B

Jamie M. Fitzgerald, **Sushanth Kini Manjeshwar**, Witlef Wieczorek, Philippe Tassin
Cavity Optomechanics with Photonic Bound States in the Continuum
Phys. Rev. Research,
vol. 3, no. 1, pp. 013131, Feb. 2021.
©DOI: 10.1103/PhysRevResearch.3.013131 .

We discuss a system comprising of two patterned structures with internal modes for example, two PhC slabs where when the parameters namely PhC radius r, lattice constant a and distance between slabs q meet certain conditions, the cavity linewidth becomes zero which points to an existence of a photonic bound state in a continuum (BIC). We show that for a realistic system at the BIC, the losses will be only given by material absorption. We show that for reasonable parameters achievable with our system, we can reach quantum cooperativity greater than unity. Quantum cooperativity is defined as the regime where single-photon coupling rate exceeds the geometric mean of the cavity and mechanical decay rates. This regime is sufficient to implement certain quantum protocols such as photon anti-bunching, quantum transduction, etc. This system could also possibly reach the elusive single photon strong-coupling regime without the need of an external cavity.

7.3 Paper C

Sushanth Kini Manjeshwar, Anastasiia Ciers, Fia Hellman, Jürgen Bläsing, André Strittmater, Witlef Wieczorek
Micromechanical high-Q trampoline resonators from strained crystalline InGaP for integrated free-space optomechanics
Published in ArXiv,
Nov. 2022.
©DOI: 10.48550/arXiv.2211.12469 .

We show a high quality factor mechanical resonator in high-stress InGaP using strain engineering. InGaP can be grown with high stress comparable to widely used high stress SiN. InGaP being crystalline in nature analogous to GaAs could provide better mechanical and optical properties compared to amorphous SiN. We use string resonators to experimentally evaluate the material properties, such as Young's modulus, yield stress and tensile stress of InGaP relevant to mechanical resonators. We realize trampoline-shaped mechanical resonators patterned with photonic crystals. The photonic crystals enable reflectance engineering to increase the out-of-plane reflectance of the resonator. We show a mechanical quality factor above 10^7, the highest reported to date in an InGaP-based micromechanical resonator.

7.4 Paper D

Sushanth Kini Manjeshwar†, Anastasiia Ciers†, Juliette Monsel†, Cindy Peralle, Shu Min Wang, Philippe Tassin, Witlef Wieczorek
Cavity optomechanics with a chip-based microcavity using a suspended

frequency-dependent photonic crystal mirror
Manuscript in preparation (2023)
† Contributed equally .

We show a monolithic sub-μm length optomechanical microcavity formed by a single PhC slab and a distributed Bragg reflector (DBR). We perform optical characterization wherein we demonstrate a precise control over the microcavity resonance wavelength by variation of the photonic crystal hole radius, notably keeping the distance between PhC slab and DBR mirror constant. We perform mechanical characterization of the suspended PhC slab similar to the works stated above. We use the transfer matrix method to successfully capture the reflectance profile of the system and subsequently extract the parameters for the quantum optics description of the optical microcavity. Finally, we show that the presence of a frequency dependent reflector leads to interesting optomechanical effects different to the canonical optomechanical system with a frequency independent mirror

7.5 Paper E

Sushanth Kini Manjeshwar, Anastasiia Glushkova, Jamie M. Fitzgerald, Shu Min Wang, Philippe Tassin, Witlef Wieczorek
Double layer photonic crystal membranes in AlGaAs heterostructures for integrated cavity optomechanics
Proceedings of CLEO 2021,
Jun. 2021.
©DOI: 10.1364/CLEO_QELS.2021.FTh2P.5 .

We build on the results shown in Paper A wherein we showcase a monolithic system of two PhC slabs separated by sub-μm gap followed by the substrate at distance of 750 nm. The fabrication is carried out to maintain uniformity between the two PhC slabs. We characterize the optical reflectance of the system where we observe a microcavity formed between the two suspended PhC slabs. We measure the mechanical eigenfrequencies of both the PhC slabs individually. As in Paper A, COMSOL and S4 simulations are performed to support the measured mechanical and optical properties.

7.6 Paper F

Anastasiia Glushkova, **Sushanth Kini Manjeshwar**, Jamie M. Fitzgerald, Shu Min Wang, Philippe Tassin, Witlef Wieczorek
Integrated free-space optomechanics with AlGaAs heterostructures
Proceedings of CLEO Europe 2021,
Jun. 2021.
©DOI: 10.1109/CLEO/Europe-EQEC52157.2021.9542149 .

This work presents the same results as seen in Paper E and presented by Anastasiia Ciers at CLEO Europe 2021.

7.7 Paper G

Jamie M. Fitzgerald, **Sushanth Kini Manjeshwar**, Witlef Wieczorek, Philippe Tassin
Nanophotonic Structures for Cavity Optomechanics
Jun. 2021.
©DOI: 10.1109/CLEO/Europe-EQEC52157.2021.9542576 .

This work presented at a conference was a precursor to Paper B.

References

[1] C. Liu, *Foundation of MEMS: International Edition*. Pearson Education Limited, 2014, ISBN: 9781292013985.

[2] A. D. O'Connell, M. Hofheinz, M. Ansmann, *et al.*, "Quantum ground state and single-phonon control of a mechanical resonator," en, *Nature*, vol. 464, no. 7289, pp. 697–703, Apr. 2010, ISSN: 1476-4687. DOI: `10.1038/nature08967`.

[3] M. Aspelmeyer, T. J. Kippenberg, and F. Marquardt, "Cavity optomechanics," *Reviews of Modern Physics*, vol. 86, no. 4, pp. 1391–1452, 2014. DOI: `10.1103/RevModPhys.86.1391`.

[4] J. Chan, T. P. M. Alegre, A. H. Safavi-Naeini, *et al.*, "Laser cooling of a nanomechanical oscillator into its quantum ground state," en, *Nature*, vol. 478, no. 7367, pp. 89–92, Oct. 2011, ISSN: 1476-4687. DOI: `10.1038/nature10461`.

[5] J. D. Teufel, T. Donner, D. Li, *et al.*, "Sideband cooling of micromechanical motion to the quantum ground state," en, *Nature*, vol. 475, no. 7356, pp. 359–363, Jul. 2011, ISSN: 1476-4687. DOI: `10.1038/nature10261`.

[6] B. Abbott, R. Abbott, R. Adhikari, *et al.*, "Observation of a kilogram-scale oscillator near its quantum ground state," *New Journal of Physics*,

vol. 11, no. 7, p. 073 032, Jul. 2009. DOI: 10.1088/1367-2630/11/7/073032.

[7] X. Liu, J. F. Vignola, H. J. Simpson, B. R. Lemon, B. H. Houston, and D. M. Photiadis, “A loss mechanism study of a very high q silicon micromechanical oscillator,” *Journal of Applied Physics*, vol. 97, no. 2, p. 023 524, 2005. DOI: 10.1063/1.1819980.

[8] R. A. Norte, J. P. Moura, and S. Gröblacher, “Mechanical resonators for quantum optomechanics experiments at room temperature,” *Phys. Rev. Lett.*, vol. 116, p. 147 202, 14 Apr. 2016. DOI: 10.1103/PhysRevLett.116.147202.

[9] A. H. Ghadimi, S. A. Fedorov, N. J. Engelsen, *et al.*, “Elastic strain engineering for ultralow mechanical dissipation,” *Science*, vol. 360, no. 6390, pp. 764–768, 2018. DOI: 10.1126/science.aar6939.

[10] S. A. Fedorov, N. J. Engelsen, A. H. Ghadimi, *et al.*, “Generalized dissipation dilution in strained mechanical resonators,” *Phys. Rev. B*, vol. 99, p. 054 107, 5 Feb. 2019. DOI: 10.1103/PhysRevB.99.054107.

[11] E. Romero, V. M. Valenzuela, A. R. Kermany, L. Sementilli, F. Iacopi, and W. P. Bowen, “Engineering the dissipation of crystalline micromechanical resonators,” *Phys. Rev. Appl.*, vol. 13, no. 4, p. 044 007, 2020. DOI: 10.1103/PhysRevApplied.13.044007.

[12] M. J. Bereyhi, A. Beccari, S. A. Fedorov, *et al.*, “Clamp-Tapering Increases the Quality Factor of Stressed Nanobeams,” *Nano Letters*, vol. 19, no. 4, pp. 2329–2333, 2019. DOI: 10.1021/acs.nanolett.8b04942.

[13] M. J. Bereyhi, A. Arabmoheghi, A. Beccari, *et al.*, “Perimeter modes of nanomechanical resonators exhibit quality factors exceeding 10^9 at room temperature,” *Phys. Rev. X*, vol. 12, p. 021 036, 2 May 2022. DOI: 10.1103/PhysRevX.12.021036.

[14] A. Beccari, D. A. Visani, S. A. Fedorov, *et al.*, “Strained crystalline nanomechanical resonators with quality factors above 10 billion,” *Nature Physics*, vol. 18, no. 4, pp. 436–441, 2022. DOI: 10.1038/s41567-021-01498-4.

[15] M. J. Bereyhi, A. Beccari, R. Groth, *et al.*, "Hierarchical tensile structures with ultralow mechanical dissipation," *Nature Communications*, vol. 13, no. 1, pp. 1–9, 2022. DOI: `10.1038/s41467-022-30586-z`.

[16] Y. Tsaturyan, A. Barg, E. S. Polzik, and A. Schliesser, "Ultracoherent nanomechanical resonators via soft clamping and dissipation dilution," *Nature nanotechnology*, vol. 12, no. 8, pp. 776–783, 2017. DOI: `10.1038/nnano.2017.101`.

[17] D. Høj, F. Wang, W. Gao, U. B. Hoff, O. Sigmund, and U. L. Andersen, "Ultra-coherent nanomechanical resonators based on inverse design," *Nature Communications*, vol. 12, no. 1, p. 5766, 2021. DOI: `10.1038/s41467-021-26102-4`.

[18] H. Yamaguchi, K. Kato, Y. Nakai, K. Onomitsu, S. Warisawa, and S. Ishihara, "Improved resonance characteristics of GaAs beam resonators by epitaxially induced strain," *Appl. Phys. Lett.*, vol. 92, no. 25, p. 251 913, 2008. DOI: `10.1063/1.2952957`.

[19] M. Hamoumi, P. E. Allain, W. Hease, *et al.*, "Microscopic Nanomechanical Dissipation in Gallium Arsenide Resonators," *Phys. Rev. Lett.*, vol. 120, no. 22, p. 223 601, 2018. DOI: `10.1103/PhysRevLett.120.223601`.

[20] M. Cotrufo, L. Midolo, Z. Zobenica, M. Petruzzella, F. W. M. van Otten, and A. Fiore, "Nanomechanical control of optical field and quality factor in photonic crystal structures," *Phys. Rev. B*, vol. 97, no. 11, p. 115 304, 2018. DOI: `10.1103/PhysRevB.97.115304`.

[21] S. Kini Manjeshwar, K. Elkhouly, J. M. Fitzgerald, *et al.*, "Suspended photonic crystal membranes in algaas heterostructures for integrated multi-element optomechanics," *Appl. Phys. Lett.*, vol. 116, no. 26, p. 264 001, 2020. DOI: `10.1063/5.0012667`.

[22] T. Watanabe, K. Onomitsu, and H. Yamaguchi, "Feedback Cooling of a Strained GaAs Micromechanical Beam Resonator," *Appl. Phys. Express*, vol. 3, no. 6, p. 065 201, 2010. DOI: `10.1143/APEX.3.065201`.

[23] L. Ding, C. Baker, P. Senellart, *et al.*, "High Frequency GaAs Nano-Optomechanical Disk Resonator," *Physical Review Letters*, vol. 105, no. 26, p. 263 903, 2010. DOI: `10.1103/PhysRevLett.105.263903`.

[24] G. D. Cole, I. Wilson-Rae, M. R. Vanner, *et al.*, “Megahertz monocrystalline optomechanical resonators with minimal dissipation,” *Proc. IEEE MEMS*, pp. 847–850, 2010. DOI: `10.1109/MEMSYS.2010.5442339`.

[25] G. D. Cole, I. Wilson-Rae, K. Werbach, M. R. Vanner, and M. Aspelmeyer, “Phonon-tunnelling dissipation in mechanical resonators,” *Nature Communications*, vol. 2, p. 231, 2011. DOI: `10.1038/ncomms1212`.

[26] H. Okamoto, D. Ito, K. Onomitsu, *et al.*, “Vibration Amplification, Damping, and Self-Oscillations in Micromechanical Resonators Induced by Optomechanical Coupling through Carrier Excitation,” *Phys. Rev. Lett.*, vol. 106, no. 3, p. 036 801, 2011. DOI: `10.1103/PhysRevLett.106.036801`.

[27] J. Liu, K. Usami, A. Naesby, *et al.*, “High-Q optomechanical GaAs nanomembranes,” *Appl. Phys. Lett.*, vol. 99, no. 24, pp. 1–4, 2011. DOI: `10.1063/1.3668092`.

[28] K. Usami, A. Naesby, T. Bagci, *et al.*, “Optical cavity cooling of mechanical modes of a semiconductor nanomembrane,” *Nature Physics*, vol. 8, no. 2, pp. 168–172, 2012. DOI: `10.1038/nphys2196`.

[29] H. Yamaguchi, “GaAs-based micro/nanomechanical resonators,” *Semicond. Sci. Technol.*, vol. 32, no. 10, p. 103 003, 2017. DOI: `10.1088/1361-6641/aa857a`.

[30] G. D. Cole, P.-L. Yu, C. Gärtner, *et al.*, “Tensile-strained $\mathrm{In}_x\mathrm{Ga}_{1-x}\mathrm{P}$ membranes for cavity optomechanics,” *Appl. Phys. Lett.*, vol. 104, no. 20, p. 201 908, 2014. DOI: `10.1063/1.4879755`.

[31] M. Bückle, V. C. Hauber, G. D. Cole, *et al.*, “Stress control of tensile-strained $\mathrm{In}_x\mathrm{Ga}_{1-x}\mathrm{P}$ nanomechanical string resonators,” *Appl. Phys. Lett.*, vol. 113, no. 20, p. 201 903, 2018. DOI: `10.1063/1.5054076`.

[32] M. Bückle, Y. S. Klaß, F. B. Nägele, R. Braive, and E. M. Weig, “Universal length dependence of tensile stress in nanomechanical string resonators,” *Phys. Rev. Applied*, vol. 15, p. 034 063, 3 Mar. 2021. DOI: `10.1103/PhysRevApplied.15.034063`.

[33] S. K. Manjeshwar, A. Ciers, F. Hellman, J. Bläsing, A. Strittmater, and W. Wieczorek, “Micromechanical high-q trampoline resonators from strained crystalline ingap for integrated free-space optomechanics,” 2022. DOI: `10.48550/ARXIV.2211.12469`.

[34] T. Faust, J. Rieger, M. J. Seitner, J. P. Kotthaus, and E. M. Weig, "Signatures of two-level defects in the temperature-dependent damping of nanomechanical silicon nitride resonators," *Phys. Rev. B*, vol. 89, p. 100 102, 10 Mar. 2014. DOI: `10.1103/PhysRevB.89.100102`.

[35] S. Gröblacher, J. B. Hertzberg, M. R. Vanner, *et al.*, "Demonstration of an ultracold micro-optomechanical oscillator in a cryogenic cavity," en, *Nature Physics*, vol. 5, no. 7, pp. 485–488, Jul. 2009, ISSN: 1745-2481. DOI: `10.1038/nphys1301`.

[36] A. Nunnenkamp, K. Børkje, and S. M. Girvin, "Single-Photon Optomechanics," *Phys. Rev. Lett.*, vol. 107, no. 6, p. 063 602, 2011. DOI: `10.1103/PhysRevLett.107.063602`.

[37] P. Rabl, "Photon blockade effect in optomechanical systems," *Phys. Rev. Lett.*, vol. 107, no. 6, pp. 1–5, 2011. DOI: `10.1103/PhysRevLett.107.063601`.

[38] W. Marshall, C. Simon, R. Penrose, and D. Bouwmeester, "Towards quantum superpositions of a mirror," *Phys. Rev. Lett.*, vol. 91, p. 130 401, 13 Sep. 2003. DOI: `10.1103/PhysRevLett.91.130401`.

[39] K. W. Murch, K. L. Moore, S. Gupta, and D. M. Stamper-Kurn, "Observation of quantum-measurement backaction with an ultracold atomic gas," en, *Nature Physics*, vol. 4, no. 7, pp. 561–564, Jul. 2008, ISSN: 1745-2481. DOI: `10.1038/nphys965`.

[40] F. Brennecke, S. Ritter, T. Donner, and T. Esslinger, "Cavity Optomechanics with a Bose-Einstein Condensate," en, *Science*, vol. 322, no. 5899, pp. 235–238, Oct. 2008, ISSN: 0036-8075, 1095-9203. DOI: `10.1126/science.1163218`.

[41] L. Ding, C. Baker, P. Senellart, *et al.*, "Wavelength-sized gaas optomechanical resonators with gigahertz frequency," *Appl. Phys. Lett.*, vol. 98, no. 11, p. 113 108, 2011. DOI: `10.1063/1.3563711`.

[42] F. Fogliano, B. Besga, A. Reigue, *et al.*, "Mapping the cavity optomechanical interaction with subwavelength-sized ultrasensitive nanomechanical force sensors," *Phys. Rev. X*, vol. 11, p. 021 009, 2 Apr. 2021. DOI: `10.1103/PhysRevX.11.021009`.

[43] G. A. Peterson, S. Kotler, F. Lecocq, *et al.*, "Ultrastrong parametric coupling between a superconducting cavity and a mechanical resonator," *Phys. Rev. Lett.*, vol. 123, p. 247 701, 24 Dec. 2019. DOI: `10.1103/PhysRevLett.123.247701`.

[44] K. Kustura, C. Gonzalez-Ballestero, A. d. l. R. Sommer, N. Meyer, R. Quidant, and O. Romero-Isart, "Mechanical squeezing via unstable dynamics in a microcavity," *Phys. Rev. Lett.*, vol. 128, p. 143 601, 14 Apr. 2022. DOI: `10.1103/PhysRevLett.128.143601`.

[45] M. Eichenfield, J. Chan, R. M. Camacho, K. J. Vahala, and O. Painter, "Optomechanical crystals," *Nature*, vol. 462, no. 7269, pp. 78–82, 2009, ISSN: 00280836. DOI: `10.1038/nature08524`.

[46] J. Hofer, A. Schliesser, and T. J. Kippenberg, "Cavity optomechanics with ultrahigh-Q crystalline microresonators," *Phys. Rev. A*, vol. 82, p. 031 804, 3 Sep. 2010. DOI: `10.1103/PhysRevA.82.031804`.

[47] G. Wachter, S. Kuhn, S. Minniberger, *et al.*, "Silicon microcavity arrays with open access and a finesse of half a million," *Light: Science & Applications*, vol. 8, no. 1, p. 37, Apr. 2019, ISSN: 2047-7538. DOI: `10.1038/s41377-019-0145-y`.

[48] H. Pfeifer, L. Ratschbacher, J. Gallego, *et al.*, "Achievements and perspectives of optical fiber Fabry–Perot cavities," *Applied Physics B*, vol. 128, no. 2, p. 29, Jan. 2022, ISSN: 1432-0649. DOI: `10.1007/s00340-022-07752-8`.

[49] M. J. Burek, J. D. Cohen, S. M. Meenehan, *et al.*, "Diamond optomechanical crystals," *Optica*, vol. 3, no. 12, pp. 1404–1411, Dec. 2016. DOI: `10.1364/OPTICA.3.001404`.

[50] X. Jiang, Q. Lin, J. Rosenberg, K. Vahala, and O. Painter, "High-q double-disk microcavities for cavity optomechanics," *Opt. Express*, vol. 17, no. 23, pp. 20 911–20 919, Nov. 2009. DOI: `10.1364/OE.17.020911`.

[51] L. Ding, C. Baker, P. Senellart, *et al.*, "High frequency gaas nano-optomechanical disk resonator," *Phys. Rev. Lett.*, vol. 105, p. 263 903, 26 Dec. 2010. DOI: `10.1103/PhysRevLett.105.263903`.

[52] G. J. Hornig, S. Al-Sumaidae, J. Maldaner, L. Bu, and R. G. DeCorby, "Monolithically integrated membrane-in-the-middle cavity optomechanical systems," *Opt. Express*, vol. 28, no. 19, pp. 28 113–28 125, Sep. 2020. DOI: `10.1364/OE.402031`.

[53] I. Favero, S. Stapfner, D. Hunger, *et al.*, "Fluctuating nanomechanical system in a high finesse optical microcavity," *Opt. Express*, vol. 17, no. 15, pp. 12 813–12 820, Jul. 2009. DOI: `10.1364/OE.17.012813`.

[54] A. Xuereb, C. Genes, and A. Dantan, "Strong Coupling and Long-Range Collective Interactions in Optomechanical Arrays," *Phys. Rev. Lett.*, vol. 109, no. 22, p. 223 601, 2012. DOI: `10.1103/PhysRevLett.109.223601`.

[55] B. Nair, A. Naesby, and A. Dantan, "Optomechanical characterization of silicon nitride membrane arrays," *Optics Letters*, vol. 42, no. 7, p. 1341, 2017. DOI: `10.1364/ol.42.001341`.

[56] P. Piergentili, L. Catalini, M. Bawaj, *et al.*, "Two-membrane cavity optomechanics," *New J. Phys.*, vol. 20, no. 8, p. 083 024, 2018. DOI: `10.1088/1367-2630/aad85f`.

[57] C. Gärtner, J. P. Moura, W. Haaxman, R. A. Norte, and S. Gröblacher, "Integrated Optomechanical Arrays of Two High Reflectivity SiN Membranes," *Nano Letters*, vol. 18, no. 11, pp. 7171–7175, 2018. DOI: `10.1021/acs.nanolett.8b03240`.

[58] X. Wei, J. Sheng, C. Yang, Y. Wu, and H. Wu, "Controllable two-membrane-in-the-middle cavity optomechanical system," *Phys. Rev. A*, vol. 99, no. 2, p. 023 851, 2019. DOI: `10.1103/PhysRevA.99.023851`.

[59] S. Fan and J. D. Joannopoulos, "Analysis of guided resonances in photonic crystal slabs," *Phys. Rev. B*, vol. 65, no. 23, p. 235 112, 2002. DOI: `10.1103/PhysRevB.65.235112`.

[60] S. Fan, W. Suh, and J. D. Joannopoulos, "Temporal coupled-mode theory for the Fano resonance in optical resonators," *J. Opt. Soc. Am. A*, vol. 20, no. 3, p. 569, Mar. 2003, ISSN: 1084-7529, 1520-8532. DOI: `10.1364/JOSAA.20.000569`.

[61] U. Kemiktarak, M. Metcalfe, M. Durand, and J. Lawall, "Mechanically compliant grating reflectors for optomechanics," *Appl. Phys. Lett.*, vol. 100, no. 6, p. 061 124, 2012. DOI: `10.1063/1.3684248`.

[62] U. Kemiktarak, M. Durand, M. Metcalfe, and J. Lawall, "Cavity optomechanics with sub-wavelength grating mirrors," *New Journal of Physics*, vol. 14, no. 12, p. 125 010, Dec. 2012, ISSN: 1367-2630. DOI: 10.1088/1367-2630/14/12/125010.

[63] K. Makles, T. Antoni, A. G. Kuhn, *et al.*, "2D photonic-crystal optomechanical nanoresonator," *Opt. Lett.*, vol. 40, no. 2, pp. 174–177, 2015. DOI: 10.1364/OL.40.000174.

[64] J. P. Moura, R. A. Norte, J. Guo, C. Schäfermeier, and S. Gröblacher, "Centimeter-scale suspended photonic crystal mirrors," *Optics express*, vol. 26, no. 2, pp. 1895–1909, 2018. DOI: 10.1364/OE.26.001895.

[65] S. Kini Manjeshwar, A. Glushkova, J. Fitzgerald, S. M. Wang, P. Tassin, and W. Wieczorek, "Double layer photonic crystal membranes in AlGaAs heterostructures for integrated cavity optomechanics," EN, in *Conference on Lasers and Electro-Optics (2021), paper FTh2P.5*, Optica Publishing Group, May 2021, FTh2P.5. DOI: 10.1364/CLEO_QELS.2021.FTh2P.5.

[66] A. Glushkova, S. Kini Manjeshwar, J. M. Fitzgerald, S. M. Wang, P. Tassin, and W. Wieczorek, "Integrated free-space optomechanics with AlGaAs heterostructures," in *2021 Conference on Lasers and Electro-Optics Europe & European Quantum Electronics Conference (CLEO/Europe-EQEC)*, Jun. 2021, pp. 1–1. DOI: 10.1109/CLEO/Europe-EQEC52157.2021.9542149.

[67] V. Tsvirkun, A. Surrente, F. Raineri, *et al.*, "Integrated III-V Photonic Crystal – Si waveguide platform with tailored optomechanical coupling," en, *Scientific Reports*, vol. 5, no. 1, p. 16 526, Nov. 2015, ISSN: 2045-2322. DOI: 10.1038/srep16526.

[68] A. Naesby and A. Dantan, "Microcavities with suspended subwavelength structured mirrors," *Opt. Express*, vol. 26, no. 23, pp. 29 886–29 894, Nov. 2018. DOI: 10.1364/OE.26.029886.

[69] O. Černotík, A. Dantan, and C. Genes, "Cavity Quantum Electrodynamics with Frequency-Dependent Reflectors," *Phys. Rev. Lett.*, vol. 122, no. 24, p. 243 601, 2019. DOI: 10.1103/PhysRevLett.122.243601.

[70] J. Baraillon, B. Taurel, P. Labeye, and L. Duraffourg, “Linear analytical approach to dispersive, external dissipative, and intrinsic dissipative couplings in optomechanical systems,” *Phys. Rev. A*, vol. 102, p. 033 509, 3 Sep. 2020. DOI: 10.1103/PhysRevA.102.033509.

[71] J. M. Fitzgerald, S. K. Manjeshwar, W. Wieczorek, and P. Tassin, “Cavity optomechanics with photonic bound states in the continuum,” *Phys. Rev. Research*, vol. 3, p. 013 131, 1 Feb. 2021. DOI: 10.1103/PhysRevResearch.3.013131.

[72] J. M. Fitzgerald, S. Kini Manjeshwar, W. Wieczorek, and P. Tassin, “Nanophotonic Structures for Cavity Optomechanics,” in *2021 Conference on Lasers and Electro-Optics Europe & European Quantum Electronics Conference (CLEO/Europe-EQEC)*, Jun. 2021, pp. 1–1. DOI: 10.1109/CLEO/Europe-EQEC52157.2021.9542576.

[73] S. Schmid, L. G. Villanueva, and M. L. Roukes, *Fundamentals of nanomechanical resonators*. Springer, 2016, vol. 49. DOI: 10.1007/978-3-319-28691-4.

[74] S. Gröblacher, “Quantum opto-mechanics with micromirrors: Combining nano-mechanics with quantum optics,” Ph.D. dissertation, University of Vienna, 2010. DOI: 10.1007/978-3-642-34955-3.

[75] M. Yuan, M. A. Cohen, and G. A. Steele, “Silicon nitride membrane resonators at millikelvin temperatures with quality factors exceeding 108,” *Applied Physics Letters*, vol. 107, no. 26, p. 263 501, 2015. DOI: 10.1063/1.4938747.

[76] M. Imboden and P. Mohanty, “Dissipation in nanoelectromechanical systems,” *Physics Reports*, vol. 534, no. 3, pp. 89–146, 2014, ISSN: 03701573. DOI: 10.1016/j.physrep.2013.09.003.

[77] Q. P. Unterreithmeier, T. Faust, and J. P. Kotthaus, “Damping of nanomechanical resonators,” *Phys. Rev. Lett.*, vol. 105, p. 027 205, 2 Jul. 2010. DOI: 10.1103/PhysRevLett.105.027205.

[78] L. Sementilli, E. Romero, and W. P. Bowen, “Nanomechanical dissipation and strain engineering,” *Advanced Functional Materials*, vol. 32, no. 3, p. 2 105 247, 2022. DOI: 10.1002/adfm.202105247.

[79] F. Hellman, "Tensile-strained micromechanical resonators made from crystalline ingap with low mechanical dissipation and high optical reflectivity," M.S. thesis, MC2, Göteborg, Sweden, 2022. DOI: `https://hdl.handle.net/20.500.12380/305576`.

[80] L. G. Villanueva and S. Schmid, "Evidence of surface loss as ubiquitous limiting damping mechanism in sin micro-and nanomechanical resonators," *Physical review letters*, vol. 113, no. 22, p. 227 201, 2014. DOI: `10.1103/PhysRevLett.113.227201`.

[81] H. Kum, D. Lee, W. Kong, *et al.*, "Epitaxial growth and layer-transfer techniques for heterogeneous integration of materials for electronic and photonic devices," en, *Nature Electronics*, vol. 2, no. 10, pp. 439–450, Oct. 2019, ISSN: 2520-1131. DOI: `10.1038/s41928-019-0314-2`.

[82] J. D. Renton, *Applied Elasticity (Second Edition)* (Woodhead Publishing Series in Civil and Structural Engineering), en, J. D. Renton, Ed. Woodhead Publishing, Jan. 2002, ISBN: 9781898563853. DOI: `10.1533/9780857099587`.

[83] M. A. Hopcroft, W. D. Nix, and T. W. Kenny, "What is the young's modulus of silicon?" *J. Microelectromechanical Systems*, vol. 19, pp. 229–238, 2010. DOI: `10.1109/JMEMS.2009.2039697`.

[84] J. Wortman and R. Evans, "Young's modulus, shear modulus, and poisson's ratio in silicon and germanium," *Journal of applied physics*, vol. 36, no. 1, pp. 153–156, 1965. DOI: `10.1063/1.1713863`.

[85] P.-L. Yu, T. P. Purdy, and C. A. Regal, "Control of material damping in high-Q membrane microresonators," *Phys. Rev. Lett.*, vol. 108, p. 083 603, 8 Feb. 2012. DOI: `10.1103/PhysRevLett.108.083603`.

[86] E. Hecht, *Optics*, 5 ed. Boston: Pearson Education, Inc, 2017, ISBN: 9780133977226.

[87] B. E. A. Saleh and M. C. Teich, *Fundamentals of photonics* (Wiley series in pure and applied optics), 2nd ed. Hoboken, N.J: Wiley Interscience, 2007, ISBN: 9780471358329.

[88] F. Elste, S. M. Girvin, and A. A. Clerk, "Quantum noise interference and backaction cooling in cavity nanomechanics," *Phys. Rev. Lett.*, vol. 102, p. 207 209, 20 May 2009. DOI: `10.1103/PhysRevLett.102.207209`.

[89] M. Wu, A. C. Hryciw, C. Healey, *et al.*, "Dissipative and dispersive optomechanics in a nanocavity torque sensor," *Phys. Rev. X*, vol. 4, p. 021 052, 2 Jun. 2014. DOI: `10.1103/PhysRevX.4.021052`.

[90] C. Genes, D. Vitali, P. Tombesi, S. Gigan, and M. Aspelmeyer, "Ground-state cooling of a micromechanical oscillator: Comparing cold damping and cavity-assisted cooling schemes," *Phys. Rev. A*, vol. 77, no. 3, p. 033 804, Mar. 2008. DOI: `10.1103/PhysRevA.77.033804`.

[91] J. Restrepo, J. Gabelli, C. Ciuti, and I. Favero, "Classical and quantum theory of photothermal cavity cooling of a mechanical oscillator," en, *Comptes Rendus Physique*, Nano- and micro-optomechanical systems, vol. 12, no. 9, pp. 860–870, Dec. 2011, ISSN: 1631-0705. DOI: `10.1016/j.crhy.2011.02.005`.

[92] D. Woolf, P.-C. Hui, E. Iwase, *et al.*, "Optomechanical and photothermal interactions in suspended photonic crystal membranes," *Opt. Express*, vol. 21, no. 6, pp. 7258–7275, Mar. 2013. DOI: `10.1364/OE.21.007258`.

[93] I. H. Deutsch, R. J. C. Spreeuw, S. L. Rolston, and W. D. Phillips, "Photonic band gaps in optical lattices," *Phys. Rev. A*, vol. 52, pp. 1394–1410, 2 Aug. 1995. DOI: `10.1103/PhysRevA.52.1394`.

[94] J. Monsel, N. Dashti, S. K. Manjeshwar, *et al.*, "Optomechanical cooling with coherent and squeezed light: The thermodynamic cost of opening the heat valve," *Phys. Rev. A*, vol. 103, p. 063 519, 6 Jun. 2021. DOI: `10.1103/PhysRevA.103.063519`.

[95] C. W. Hsu, B. Zhen, A. D. Stone, J. D. Joannopoulos, and M. Soljačić, "Bound states in the continuum," en, *Nature Reviews Materials*, vol. 1, no. 9, pp. 1–13, Jul. 2016, ISSN: 2058-8437. DOI: `10.1038/natrevmats.2016.48`.

[96] Y. Wu, L. Kang, and D. H. Werner, "Active quasi-bic optical vortex generators for ultrafast switching," *New Journal of Physics*, vol. 24, no. 3, p. 033 002, Mar. 2022. DOI: `10.1088/1367-2630/ac52c0`.

[97] C. B. R. Hurtado, J. Dickmann, F. F. Bruns, T. Siefke, and S. Kroker, "Bound states in the continuum for optomechanical light control with dielectric metasurfaces," *Opt. Express*, vol. 28, no. 14, pp. 20 106–20 116, Jul. 2020. DOI: `10.1364/OE.392782`.

[98] COMSOL AB, Stockholm, Sweden, *Comsol multiphysics*, `www.comsol.com`, version 6.0, 2019.

[99] A. Akbar Darki, R. Vinther Nielsen, J. Vinge Nygaard, and A. Dantan, “Mechanical investigations of free-standing sin membranes patterned with one-dimensional photonic crystal structures,” *Journal of Applied Physics*, vol. 131, no. 19, p. 195 101, 2022. DOI: `10.1063/5.0093016`.

[100] S. Fedorov, “Mechanical resonators with high dissipation dilution in precision and quantum measurements,” Ph.D. dissertation, IEL, Lausanne, 2020, p. 205. DOI: `10.5075/epfl-thesis-10421`.

[101] M. G. Moharam and T. K. Gaylord, “Rigorous coupled-wave analysis of planar-grating diffraction,” *J. Opt. Soc. Am.*, vol. 71, no. 7, pp. 811–818, Jul. 1981. DOI: `10.1364/JOSA.71.000811`.

[102] A. Junker, “Advances in the Performance and Applicability of Modal Electromagnetic Simulations,” Ph.D. dissertation, Natural Sciences and Mathematics, 2018. DOI: `10.11588/HEIDOK.00024770`.

[103] T. Stomeo, M. Grande, G. Raino, *et al.*, “Optical filter based on two coupled PhC GaAs-membranes,” *Opt. Lett.*, vol. 35, no. 3, pp. 411–413, 2010. DOI: `10.1364/OL.35.000411`.

[104] N. Ikeda, Y. Sugimoto, Y. Watanabe, *et al.*, “Precise control of dry etching for nanometer scale air-hole arrays in two-dimensional GaAs/AlGaAs photonic crystal slabs,” *Optics Communications*, vol. 275, no. 1, pp. 257–267, 2007, ISSN: 00304018. DOI: `10.1016/j.optcom.2007.03.036`.

[105] “Modelling and fabrication of GaAs photonic-crystal cavities for cavity quantum electrodynamics,” *Nanotechnology*, vol. 21, no. 6, 2010, ISSN: 09574484. DOI: `10.1088/0957-4484/21/6/065202`.

[106] X. Zhang, Y. Togano, K. Hashimura, M. Morifuji, and M. Kondow, “Dry etching of Al-rich AlGaAs with silicon nitride masks for photonic crystal fabrication,” *Japanese Journal of Applied Physics*, vol. 54, no. 4, 2015, ISSN: 13474065. DOI: `10.7567/JJAP.54.042003`.

[107] X. Zhang, K. Takeuchi, X. Cong, *et al.*, “Dry etching of deep air holes in GaAs/AlGaAs-based epi-wafer having InAs quantum dots for fabrication of photonic crystal laser,” *Jpn. J. Appl. Phys.*, vol. 56, no. 12, p. 126 501, 2017. DOI: `10.7567/JJAP.56.126501`.

[108] M. M. A. J. Voncken, J. J. Schermer, A. T. J. van Niftrik, *et al.*, “Etching alas with hf for epitaxial lift-off applications,” *Journal of The Electrochemical Society*, vol. 151, no. 5, G347, Mar. 2004. DOI: 10.1149/1.1690293.

[109] L. Midolo, T. Pregnolato, G. Kiršanskė, and S. Stobbe, “Soft-mask fabrication of gallium arsenide nanomembranes for integrated quantum photonics,” *Nanotechnology*, vol. 26, no. 48, p. 484 002, 2015. DOI: 10.1088/0957-4484/26/48/484002.

[110] S. Sioncke, D. P. Brunco, M. Meuris, *et al.*, “Etch Rates of Ge, GaAs and InGaAs in Acids, Bases and Peroxide Based Mixtures,” *ECS Transactions*, vol. 16, no. 10, pp. 451–460, Oct. 2008, ISSN: 1938-5862, 1938-6737. DOI: 10.1149/1.2986802.

[111] D. Arslan, A. Dehé, and H. L. Hartnagel, “New concept of lateral gaas field emitter for sensor applications,” *Journal of Vacuum Science & Technology B: Microelectronics and Nanometer Structures Processing, Measurement, and Phenomena*, vol. 17, no. 2, pp. 784–787, 1999. DOI: 10.1116/1.590640.

[112] H.-A. Bachor and T. C. Ralph, *A Guide to Experiments in Quantum Optics*, en, 1st ed. Wiley, Sep. 2019, ISBN: 9783527411931 9783527695805. DOI: 10.1002/9783527695805.

[113] A. Xuereb, C. Genes, and A. Dantan, “Collectively enhanced optomechanical coupling in periodic arrays of scatterers,” *Physical Review A*, vol. 88, no. 5, pp. 1–13, 2013. DOI: 10.1103/PhysRevA.88.053803.

[114] C. H. Bui, J. Zheng, S. W. Hoch, L. Y. T. Lee, J. G. E. Harris, and C. Wei Wong, “High-reflectivity, high-Q micromechanical membranes via guided resonances for enhanced optomechanical coupling,” *Appl. Phys. Lett.*, vol. 100, no. 2, p. 021 110, 2012. DOI: 10.1063/1.3658731.

[115] X. Chen, C. Chardin, K. Makles, *et al.*, “High-finesse Fabry-Perot cavities with bidimensional Si3N4 photonic-crystal slabs,” *Light: Science and Applications*, vol. 6, no. 1, pp. 1–8, 2017. DOI: 10.1038/lsa.2016.190.

[116] V. Liu and S. Fan, “S^4 : A free electromagnetic solver for layered periodic structures,” *Computer Physics Communications*, vol. 183, no. 10, pp. 2233–2244, 2012, ISSN: 0010-4655. DOI: 10.1016/j.cpc.2012.04.026.

[117] J. Sweet, B. C. Richards, J. D. Olitzky, *et al.*, "GaAs photonic crystal slab nanocavities: Growth, fabrication, and quality factor," *Photonics and Nanostructures - Fundamentals and Applications*, vol. 8, no. 1, pp. 1–6, 2010. DOI: 10.1016/j.photonics.2009.10.004.

[118] Y. Tanaka, T. Asano, Y. Akahane, B.-S. Song, and S. Noda, "Theoretical investigation of a two-dimensional photonic crystal slab with truncated cone air holes," *Appl. Phys. Lett.*, vol. 82, no. 11, pp. 1661–1663, 2003. DOI: 10.1063/1.1559947.

[119] S. S. Verbridge, J. M. Parpia, R. B. Reichenbach, L. M. Bellan, and H. G. Craighead, "High quality factor resonance at room temperature with nanostrings under high tensile stress," *Journal of Applied Physics*, vol. 99, no. 12, p. 124 304, 2006. DOI: 10.1063/1.2204829.

[120] C. Reinhardt, T. Müller, A. Bourassa, and J. C. Sankey, "Ultralow-Noise SiN Trampoline Resonators for Sensing and Optomechanics," *Phys. Rev. X*, vol. 6, p. 021 001, 2 Apr. 2016. DOI: 10.1103/PhysRevX.6.021001.

[121] C. Reetz, R. Fischer, G. Assumpção, *et al.*, "Analysis of Membrane Phononic Crystals with Wide Band Gaps and Low-Mass Defects," *Phys. Rev. Applied*, vol. 12, no. 4, p. 044 027, 2019. DOI: 10.1103/PhysRevApplied.12.044027.

[122] D. Shin, A. Cupertino, M. H. de Jong, P. G. Steeneken, M. A. Bessa, and R. A. Norte, "Spiderweb nanomechanical resonators via bayesian optimization: Inspired by nature and guided by machine learning," *Advanced Materials*, vol. 34, no. 3, p. 2 106 248, 2022. DOI: 10.1002/adma.202106248.

[123] A. R. Kermany, G. Brawley, N. Mishra, E. Sheridan, W. P. Bowen, and F. Iacopi, "Microresonators with q-factors over a million from highly stressed epitaxial silicon carbide on silicon," *Appl. Phys. Lett.*, vol. 104, no. 8, p. 081 901, 2014. DOI: 10.1063/1.4866268.

[124] T. S. Kim, H. J. Kim, D.-M. Geum, *et al.*, "Ultra-Lightweight, Flexible InGaP/GaAs Tandem Solar Cells with a Dual-Function Encapsulation Layer," *ACS Appl. Mater. Interfaces*, vol. 13, no. 11, pp. 13 248–13 253, 2021. DOI: 10.1021/acsami.1c00006.

[125] S. Bahl, L. Camnitz, D. Houng, M. Mierzwinski, J. Turner, and G. Lefforge, “Reliability investigation of InGaP/GaAs heterojunction bipolar transistors,” in *Proceedings of International Electron Devices Meeting*, 1995, pp. 815–818. DOI: `10.1109/IEDM.1995.499342`.

[126] M. H. J. de Jong, M. A. ten Wolde, A. Cupertino, S. Gröblacher, P. G. Steeneken, and R. A. Norte, “Mechanical dissipation by substrate–mode coupling in sin resonators,” *Appl. Phys. Lett.*, vol. 121, no. 3, p. 032 201, 2022. DOI: `10.1063/5.0092894`.

[127] S. Adachi, “Refractive indices of iii–v compounds: Key properties of ingaasp relevant to device design,” *Journal of Applied Physics*, vol. 53, no. 8, pp. 5863–5869, 1982. DOI: `10.1063/1.331425`.

[128] A. B. Djurišić, A. D. Rakić, P. C. K. Kwok, E. H. Li, and M. L. Majewski, “Modeling the optical constants of gap, inp, and inas,” *Journal of Applied Physics*, vol. 85, no. 7, pp. 3638–3642, 1999. DOI: `10.1063/1.369727`.

[129] K. C. Balram, M. Davanço, J. Y. Lim, J. D. Song, and K. Srinivasan, “Moving boundary and photoelastic coupling in GaAs optomechanical resonators,” en, *Optica*, vol. 1, no. 6, p. 414, Dec. 2014, ISSN: 2334-2536. DOI: `10.1364/OPTICA.1.000414`.

[130] M. Mitchell, A. C. Hryciw, and P. E. Barclay, “Cavity optomechanics in gallium phosphide microdisks,” *Appl. Phys. Lett.*, vol. 104, no. 14, p. 141 104, Apr. 2014, ISSN: 0003-6951. DOI: `10.1063/1.4870999`.

[131] K. Schneider, Y. Baumgartner, S. Hönl, *et al.*, “Optomechanics with one-dimensional gallium phosphide photonic crystal cavities,” en, *Optica*, vol. 6, no. 5, p. 577, May 2019, ISSN: 2334-2536. DOI: `10.1364/OPTICA.6.000577`.

[132] J. Guo, R. Norte, and S. Gröblacher, “Feedback Cooling of a Room Temperature Mechanical Oscillator close to its Motional Ground State,” *Phys. Rev. Lett.*, vol. 123, no. 22, p. 223 602, Nov. 2019. DOI: `10.1103/PhysRevLett.123.223602`.

[133] I. Ghorbel, F. Swiadek, R. Zhu, *et al.*, “Optomechanical gigahertz oscillator made of a two photon absorption free piezoelectric III/V semiconductor,” *APL Photonics*, vol. 4, no. 11, p. 116 103, Nov. 2019. DOI: `10.1063/1.5121774`.

[134] P. Rohse, J. Butlewski, F. Klein, *et al.*, “A cavity optomechanical locking scheme based on the optical spring effect,” *Review of Scientific Instruments*, vol. 91, no. 10, p. 103 102, Oct. 2020, ISSN: 0034-6748. DOI: `10.1063/5.0010255`.

[135] F. Rochau, I. Sánchez Arribas, A. Brieussel, S. Stapfner, D. Hunger, and E. M. Weig, “Dynamical Backaction in an Ultrahigh-Finesse Fiber-Based Microcavity,” *Phys. Rev. Appl.*, vol. 16, no. 1, p. 014 013, Jul. 2021. DOI: `10.1103/PhysRevApplied.16.014013`.

[136] A. Frisk Kockum, A. Miranowicz, S. De Liberato, S. Savasta, and F. Nori, “Ultrastrong coupling between light and matter,” en, *Nature Reviews Physics*, vol. 1, no. 1, pp. 19–40, Jan. 2019, ISSN: 2522-5820. DOI: `10.1038/s42254-018-0006-2`.